Facile Fabrication of Various Titanium Oxide Particles for the Visible Light Photocatalytic Application

Zhehan YU

Division of Materials Science and Engineering
Graduate School of Engineering
Hokkaido University

September 2022

Table of Contents

Abstract

Nanotechnology is one of the most attracting research objectives in the world. Due to the small size, nanomaterials usually show unique properties, making it useful in many fields of research. Titanium dioxide, TiO_2, which is one kind of metal oxide materials, has become the most widely used material.

In chapter 1, an overview of this dissertation is given. At first, a review of metal oxide nanomaterial is given, which focuses on TiO_2 with its different structure. In addition, other metal oxide materials are mentioned in this chapter. Then, an introduction of photocatalysis is summarized, containing the structure of dyes (Rhodamine B, methylene blue) and the general photodegradation mechanism of dyes.

In chapter 2, two different fabrication methods are reported for the fabrication of TiO_2. Black TiO_2 nanoparticles (b-TiO_2) with superior solar–thermal water evaporation performance are prepared using a one-step solution plasma process (SPP) in ambient conditions. It is found that radicals that are generated during SPP play a critical role in b-TiO_2 formation by comparing several water–alcohol electrolyte environments for the SPP synthesis. Our results show that the radical-induced formation of a black TiO_{2-x} layer on the Ti electrode is necessary for b-TiO_2 formation, which was ignored in previous studies. A two-step mechanism for b-TiO_2 formation in SPP synthesis is proposed: (I) pre-oxidation of a Ti electrode surface; and (II) quenching and aggregation of sputtered molten TiO_x clusters to form b-TiO_2 particles. In addition, EC-SPSC method is also used for the fabrication of TiO_2. Although it is proved that EC-SPSC is able to form TiO_2, the morphology of the product is very unstable, resisting the further research.

In chapter 3, a new kind of TiO_2 is fabricated by a one-step method for the visible light utilization. This new TiO_2 has ellipsoidal shape, so it is called e-TiO_2. e-TiO_2 is single crystal structure, with oxygen vacancies and low-valance Ti components. In the fabrication method, hydrogen peroxide was used for the oxidation of titanium plate, and ammonia fluoride was used for the microparticle morphology controlling and pore introducing. Characterizations and calculations have proved that our as-synthesized TiO_2 microparticles were in anatase phase with meso pores, single crystal structure and Ti (III) component. UV–vis–NIR spectra have also indicated that the bandgap of the e-TiO_2 was 2.4 eV, much lower than typical anatase materials (3.2 eV). Rhodamine B and methylene blue were introduced as dyes for the photodegradation test of the e-TiO_2 compared to commercial P25–TiO_2. Our e-TiO_2 had better adsorption of both dyes

and very high efficiency for the photodegradation of Rhodamine B under visible light illumination, whose kinetic constant is four times as much as P25–TiO_2. Thus, the one-step synthesized e-TiO_2 has high efficiency for visible light dye photodegradation.

In chapter 4, a facile modification method is introduced to increase the visible light activity of TiO_2 samples. Titanium isopropoxide (TTIP) is used as the raw Ti source, then hydrolyzing in acidic and alkaline solutions, respectively, to fabricate different TiO_2 samples as pretreatment TiO_2 together with P25-TiO_2. Only hydrogen peroxide and ammonia fluoride are used for this facile modification method, and three TiO_2 samples are modified for the visible light degradation. The present method could promote the transformation of crystalline TiO_2 from rutile to anatase, increase the specific surface area, and the bandgap of samples shift to lower energy (2.2 – 3.0 eV) after the modification. For the visible light photodegradation tests, all the three modified samples show a higher visible light photodegradation efficiency. The highest kinetic constant of Rhodamine B and methylene blue degradation is 7 and 2 times that of P25, respectively. In addition, TiO_2 fabricated by TTIP in alkaline solution and its as-modified sample show the highest adsorption of methylene blue dye, whose adsorption rate reaches 9 times that of P25. Thus, the present facile modification can effectively improve the photocatalytic ability of TiO_2 under visible light.

In chapter 5, an overall conclusion of this dissertation is summarized.

All in all, this dissertation thesis presents a series of systematic research on the enhancement of TiO_2 metal oxide materials, for the enhancement of visible light utilization. This work shows three different pathways to improve the visible light activity of TiO_2 materials. Fabricating new TiO_2 can directly obtain the desired product. However, the yield of both b-TiO_2 and e-TiO_2 are low, which prevents them from further research. Modification is another way for the visible light activity improvement. At this point, the modification of TiO_2 by H_2O_2 + NH_4F can effectively increase the visible light photodegradation efficiency. This method has higher yield than fabricating new TiO_2. In addition, this method can be combined with other modification methods. Therefore, this pathway will be the focus of future research in this experiment.

CHAPTER 1

General Introduction

1.1 Nanomaterials

Nanotechnology is one of the most promising research fields, which has attracted great attention from the researchers worldwide [1]. Nanomaterial is one important part of nanotechnology, which is defined as 'the material with at least one dimension between 1 and 100 nm' [2]. Since nanomaterials have different properties from macroscopic matters due to the differences of surface effects, small-sized effects, macroscopic quantum tunneling effects and quantum confinement effects, nanomaterials often have unique optical, electronic, thermo, and mechanical performance [3, 4]. Recently, research on nanomaterials has become more popular, and related products also appear, making nanomaterials have very broad research and application prospects. According to the dimensions, nanomaterials can be divided into the following categories, from 0D (three-dimension scales all at the nanoscale) to 2D (one dimension scale at the nanoscale). According to chemical composition, nanomaterials can be divided into nanometals, nanocrystals, nanoceramics, nanoglasses, nanopolymers and nanocomposites. Among these materials, metal oxide nanoparticles are one of the most widely used nanomaterials due to their unique properties [5]. In this chapter, we will focus on metal oxides, with a focus on titanium dioxide, to introduce the metal oxides involved in this experiment. At the same time, we will also introduce the dye degradation, which works as the application of metal oxide.

1.2 Metal Oxides

Metal elements refer to the elements with metallic properties. They are usually located on the left and bottom left of the periodic table, which mean that they have few valence shell electrons, and easy to lose electrons in chemical reactions. This characteristic indicates that the metal element is usually reducible. Table 1.1 summarizes the standard electrode potentials of common metals [6].

Table 1.1. Standard electrode potentials of common metals.

Element	**Half-reaction**			**E^0/V**
	Oxidant	**⇌**	**Reductant**	
Li	$Li^+ + e^-$	⇌	Li	-3.0401

Na	$Na^+ + e^-$	⇌	Na	-2.71
Mg	$Mg^{2+} + 2e^-$	⇌	Mg	-2.372
Al	$Al^{3+} + 3e^-$	⇌	Al	-1.662
Ti	$Ti^{2+} + 2e^-$	⇌	Ti	-1.630
Mn	$Mn^{2+} + 2e^-$	⇌	Mn	-1.185
Fe	$Fe^{2+} + 2e^-$	⇌	Fe	-0.447
Cu	$Cu^{2+} + 2e^-$	⇌	Cu	0.3419
Zn	$Zn^{2+} + 2e^-$	⇌	Zn	-0.7618
Mo	$Mo^{3+} + 3e^-$	⇌	Mo	-0.200
W	$WO_3 + 6H^+ + 6e^-$	⇌	$W + 3H_2O$	-0.090

Generally, as a strong oxidant, oxygen is easy to react with metals and form metal oxides [6]. A metal oxide is a type of chemical compound with one or more oxygen atoms as well as another metal element in its composition. Alkali metal, alkaline earth metal and transition metal (in lower valence) usually form ionic oxides. The high-valence oxides formed by metals usually have covalent bonds. [7] Among these metal oxides, transition metal oxides (TMO) are commonly used because of their catalytic activity and semiconductive properties due to the unique nature of outer d-electrons [8]. Since the overlap between metal d electrons and oxygen orbitals is small, the bandgaps of TMO are typically in the order of 1 or 2 eV. This characteristic indicates that transition metal oxides have good photoactivity.

Table 1.2 Bandgaps of transition metal oxides (TMO).

Nature of TMO	**Bandgap Energy (eV)**	**Reference**
TiO_2 (Anatase)	3.2	[9]
TiO_2 (Rutile)	3.0	[9]
Cr_2O_3	3.0	[10]
MnO_2	1.3	[11]
Fe_2O_3	2.2	[12]
Cu_2O	2.2	[13]
CuO	1.4	[14]

ZnO	3.4	[15]
MoO_3	3.2	[16]
WO_3	2.4 – 2.8	[17]

1.3 Titanium Dioxide

1.3.1 Brief Introduction

Titanium dioxide (TiO_2), also known as titanium (IV) oxide or titania, is one of the most promising materials in both research and industry. Generally, TiO_2 is a kind of white solid. It has the best opacity, best whiteness, and best brightness, which is recognized as the best white pigment in the world today. Therefore, TiO_2 is widely used in coating, plastic, papermaking, printing ink, chemical fiber, rubber, cosmetics, and other industries. TiO_2 has high melting point (1840°C) [18], so it can also be used to produce high temperature resistant materials. In addition, TiO_2 has semiconductor properties, and can be used for the electron components such as electrochromic displays [19].

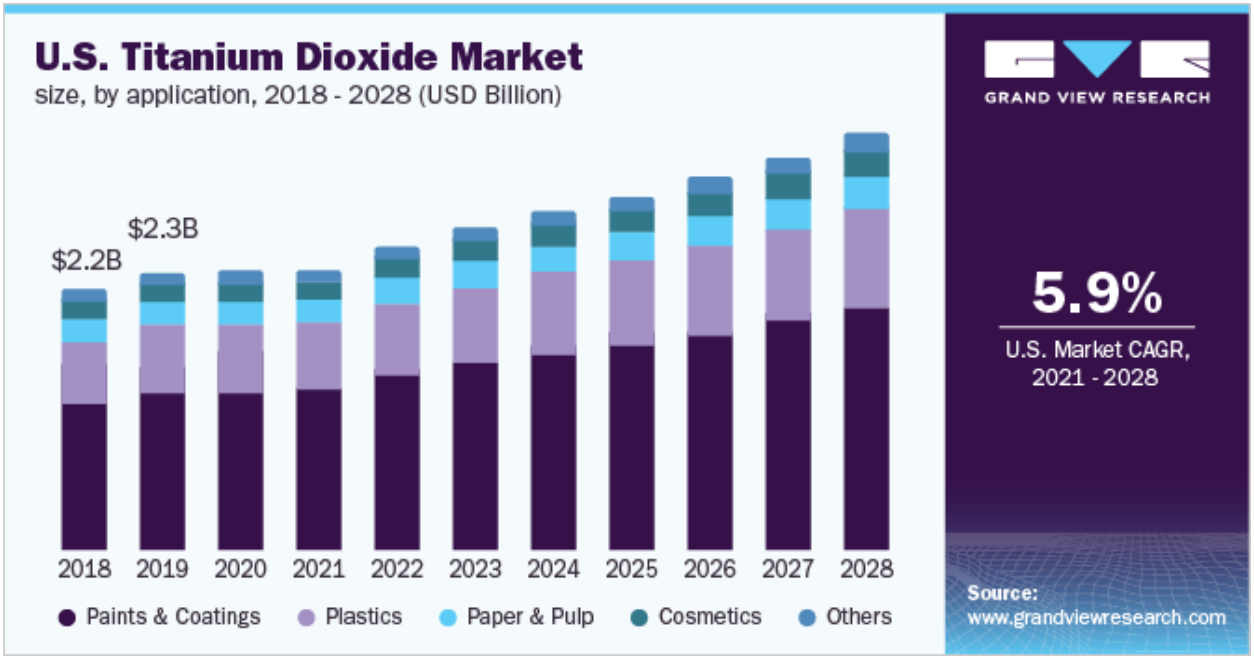

Figure 1.1. U.S. TiO_2 market size by application, from 2018 to 2028 [20].

TiO_2 is also chemically stable. It is non-toxic and insoluble in water and dilute sulfuric acid. In industry, TiO_2 can be produced by gas-phase oxidation method:

$$TiCl_4 + O_2 \xrightarrow{923K\sim1023K} TiO_2 + 2Cl_2 \quad (1.1)$$

Besides, TiO_2 is generally extracted from Ti-bearing minerals by using the following method. At first, ground ilmenite is used with concentrated sulfuric acid (≥ 80%) to react in the continuous air and stirring to obtain soluble sulfate.

$$FeTiO_3 + 2H_2SO_4 \xrightarrow{343K\sim353K} TiOSO_4 + FeSO_4 + 2H_2O \quad (1.2)$$

Then hydrolyzing the Ti liquid:

$$TiOSO_4 + 2H_2O \xrightarrow{Hydrolysis} TiO_2 \cdot H_2O + H_2SO_4 \quad (1.3)$$

In laboratory, TiO_2 can be prepared by the sol-gel method.

$$Ti(OEt)_4 + 2H_2O \rightarrow TiO_2 + 4EtOH \quad (1.4)$$

According to Table 1.2, the bandgap of TiO_2 locates at 3 eV, which is in the range of ultraviolet. As a result, TiO_2 has strong ultraviolet shielding properties because of the high absorption of ultraviolet.

1.3.2 Rutile

Rutile is the most common natural form of TiO_2, which was first described by Abraham Gottlob Werner in 1803. Rutile ore is usually red, while rutile-TiO_2 is white. Rutile is brittle, with a hardness of 6 ~ 6.5, and a density of 4.2 ~ 4.3 g/cm^3. Thermodynamically, rutile is the most stable structure among all TiO_2 materials because of the lower free energy [21].

As crystal, rutile has tetragonal crystal system. The unit cell parameters of rutile are $a = b =$ 4.584 Å, while c = 2.953 Å [22]. According to Figure 1.2, Ti cations have a coordination number of 6, forming an octahedral structure with surrounding oxygen. O anions have a coordination number of 3, forming a flat triangular structure with surrounding Ti. During the reduction process, oxygen vacancies would appear in the structure, and couple to Ti^{3+} centers [23]. Also, hydrogen can enter the structure, existing as a single occupant (H^+) or forming a hydroxyl group with the surrounding oxygen [23].

According to Table 1.2, the bandgap of rutile is 3.0 eV, locating in UV range. This makes rutile so effective at absorbing UV radiation. So rutile can be used as a sunscreen to prevent the skin damage. In addition, rutile can also be used as semiconductor because of the large bandgap [24].

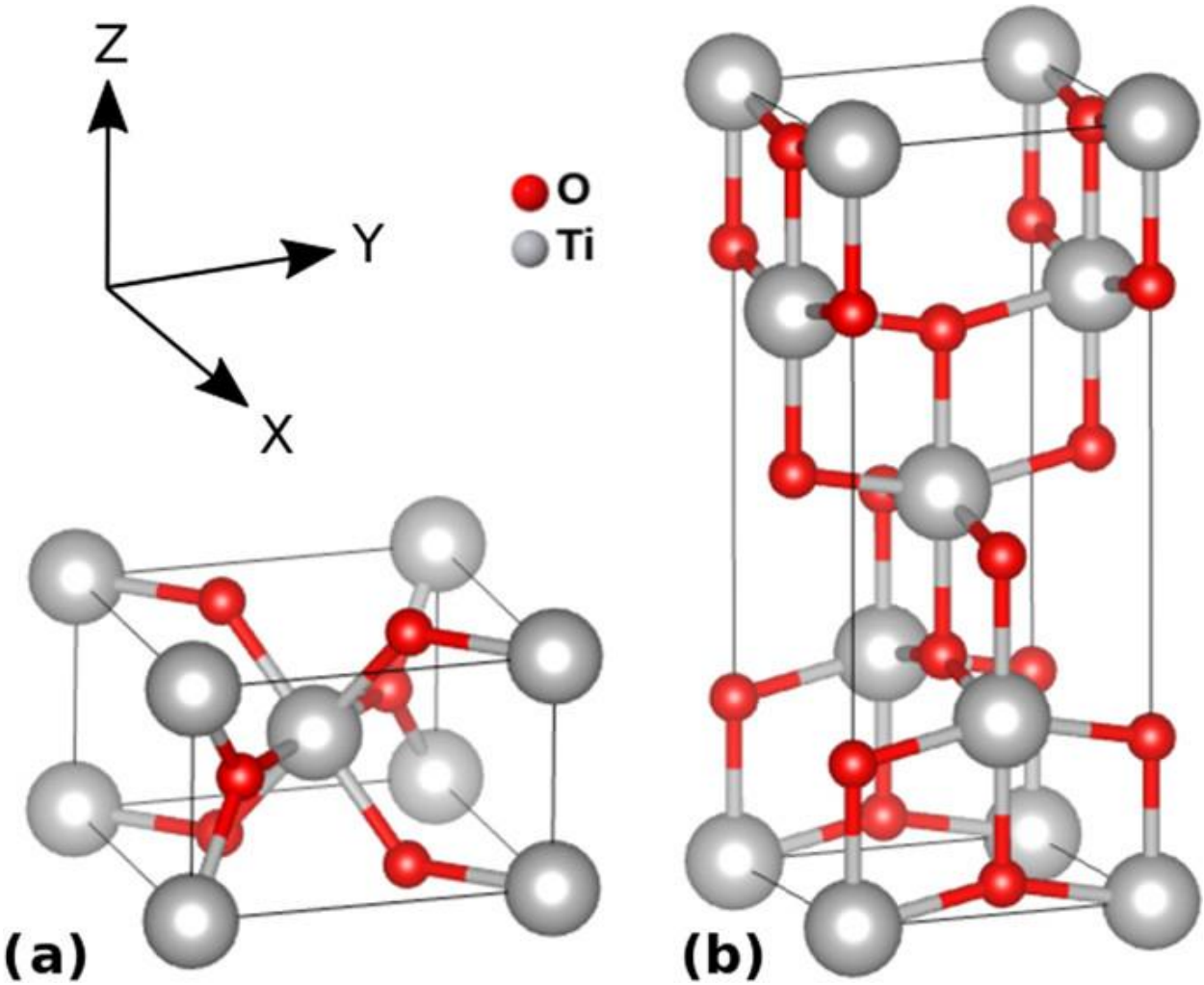

Figure 1.2. Sketch of the conventional cells of (a) rutile and (b) anatase [25].

1.3.2 Anatase

Anatase is another metastable naturally mineral form of TiO_2 in addition to rutile, which is first named by René Just Haüy in 1801. Pure anatase is colorless or white. Generally, compared to rutile, anatase is stable only at low temperature. The hardness of anatase is 5.5 ~ 6.5, and the density is 3.8 ~ 4.0 g/cm^3. Due to its low surface energy, anatase is usually the first phase formed in the TiO_2 fabrication sample. However, at high temperature, anatase would transform to rutile [26].

Figure 1.2 shows the crystal structure of anatase. Anatase also has tetragonal crystal system. The unit cell parameters of rutile are $a = b = 3.7852$ Å, while $c = 9.5139$ Å [27]. According to the figure, O anions are cubic closest packing, while Ti cations are in the octahedral voids. The coordination number of Ti is 6, and O is 3. The [TiO_6] octahedra relate to each other by sharing

two pairs of opposite edges, forming a helical chain, which is parallel to the *c*-axis. The plane (1 0 1) is the most thermodynamically stable surface [28].

Anatase is considered to have higher photoactivity than rutile [29]. Based on Table 1.2, anatase (3.2 eV) has a larger bandgap than rutile (3.0 eV). Although reducing the absorbed light, the valence band of anatase may raise to higher energy levels relating to the redox potentials of adsorbed molecules, which increases the oxidation ability of electrons, and improving its transformation from TiO_2 to adsorbed molecules [30]. In addition, the surface properties [31, 32], and the differences of charge transportation between different polymorphs [33] can also cause the higher photoactivity of anatase.

1.3.3 P25

Evonik Aeroxide P25-TiO_2 (formerly Degussa P25-TiO_2 [34], hereinafter called P25) is the most famous multiphasic TiO_2 nanoparticle material. Appeared in early 1980s, up to now, more than 10,000 papers of P25 have been published. P25 has small size (10 – 40 nm) [35, 36] and low density (around 4 g/ml), which also has a high specific surface area (50 – 60 m^2/g) [37]. The color of P25 is usually white, while a small part of P25 is yellow.

P25 has a binary structure of rutile and anatase, with a ratio of 80:20 (anatase over rutile) [38]. It is generally believed that rutile structure hinders the reaction of light on anatase surface. However, P25 presents a morphology of nanoclusters, containing small rutile crystallites with anatase crystallites. The transfer of excited electrons and holes within the mixed-phase TiO_2 may enhance the charge separation and increase the efficiency of electron-hole pair utilization [39]. As a result, P25 has become the most popular commercial TiO_2 for the research of photocatalysis.

1.4 Other Metal Oxide Materials

1.4.1 Tungsten Trioxide

Tungsten trioxide (WO_3), also known as tungsten (VI) oxide, is a chemical compound containing oxygen and tungsten. At ambient temperature, WO_3 is pale yellow. As the temperature increases, the color changes from light to dark. The color of WO_3 in molten state is green. The density of WO_3 is 7.16 g/cm^3, and the melting point is 1473°C. Therefore, WO_3 can be used as a pigment in ceramics and paints [40]. In addition, WO_3 can also be used to fabricate tungstate for fireproofing fabrics [41], gas sensors [42], and electrochromic windows [43, 44].

WO_3 is stable in air. It is insoluble in water and inorganic acids, except hydrofluoric acid. WO_3 can be prepared by different ways. Scheelite ($CaWO_4$) is a common mineral which can be used for the WO_3 fabrication [40].

$$CaWO_4 + 2HCl \rightarrow CaCl_2 + H_2WO_4 \quad (1.5)$$

$$H_2WO_4 \rightarrow H_2O + WO_3 \quad (1.6)$$

WO_3 is a strong oxidizing agent:

$$WO_3 + 2Fe \rightarrow W + Fe_2O_3 \quad (1.7)$$

$$2WO_3 + Pt \rightarrow 2WO_2 + PtO_2 \quad (1.8)$$

Figure 1.3 shows the crystal structure of WO_3 and H_2WO_4. The crystal structure of WO_3 is related to the temperature. At the temperature above 740°C, WO_3 shows tetragonal structure, while from 330°C to 740°C, WO_3 shows orthorhombic structure. Besides, WO_3 is monoclinic from 17°C to 330°C, and triclinic from -50°C to 17°C. Finally, at the temperature below -50°C, WO_3 is monoclinic again [45].

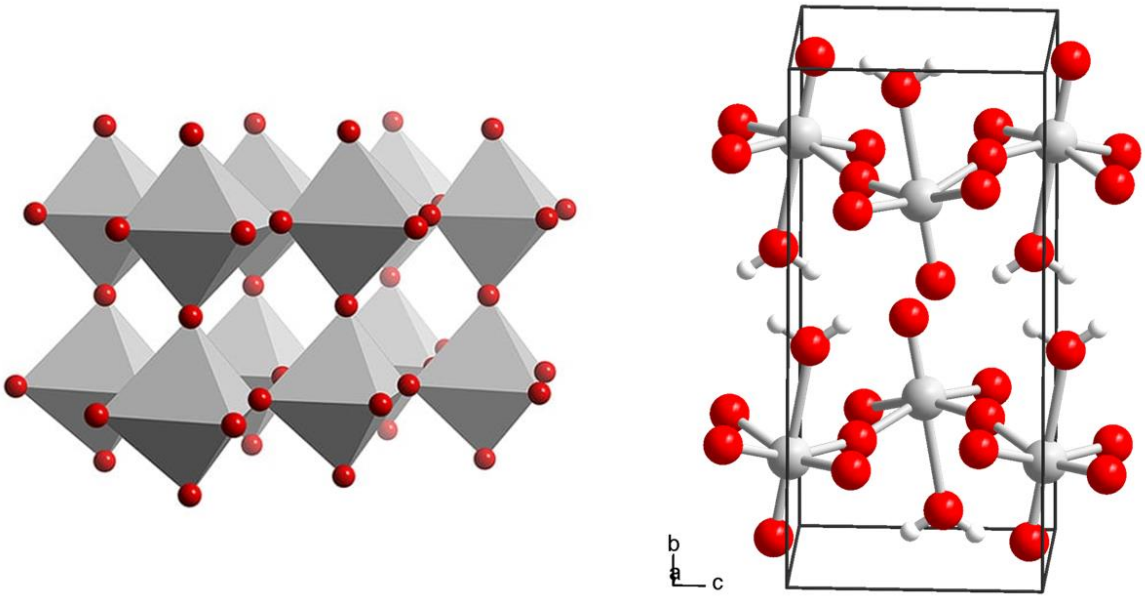

Figure 1.3. Crystal structure of (a) WO_3 and (b) H_2WO_4.

1.4.2 Manganese Dioxide

Manganese dioxide (MnO_2) is a black or brown solid, which is most stable form in all manganese oxides. Generally, MnO_2 is present in the form of pyrolusite. The density of MnO_2 is 5.08 g/cm^3, while the melting point is 535°C [46]. MnO_2 is well-known as an electrode of zinc-

manganese battery [47]. In addition, MnO_2 can be used as catalyst (in the famous decomposition of H_2O_2 to produce O_2 reaction [48]) or oxidant (for the oxidation of allylic alcohols). It is also used as a pigment and as a precursor to other Mn compounds, e.g., $KMnO_4$.

In industry, N_2O_4 is commonly used for the purification of crude MnO_2 feedstocks.

$$MnO_2 + N_2O_4 \overset{400°C}{\underset{H_2O}{\leftrightharpoons}} Mn(NO_3)_2 \tag{1.9}$$

MnO_2 can be used as an oxidant [47].

$$2MnO_2 + 2H_2SO_4 \rightarrow 2MnSO_4 + O_2 + 2H_2O \tag{1.10}$$

MnO_2 can also be used as a reducing agent.

$$2MnO_2 + 4KOH + O_2 \rightarrow 2K_2MnO_4 + 2H_2O \tag{1.11}$$

Figure 1.4 shows the crystal structures of MnO_2. Like other metal oxide materials, MnO_2 crystallizes in a rutile crystal structure, with three-coordinate oxide and octahedral metal centers [47]. This kind of MnO_2 is called β-MnO_2. The α-polymorph of MnO_2, also called as Mn_8O_{16} [49], has 'channels', which is a very open structure and can accommodate other metal atoms.

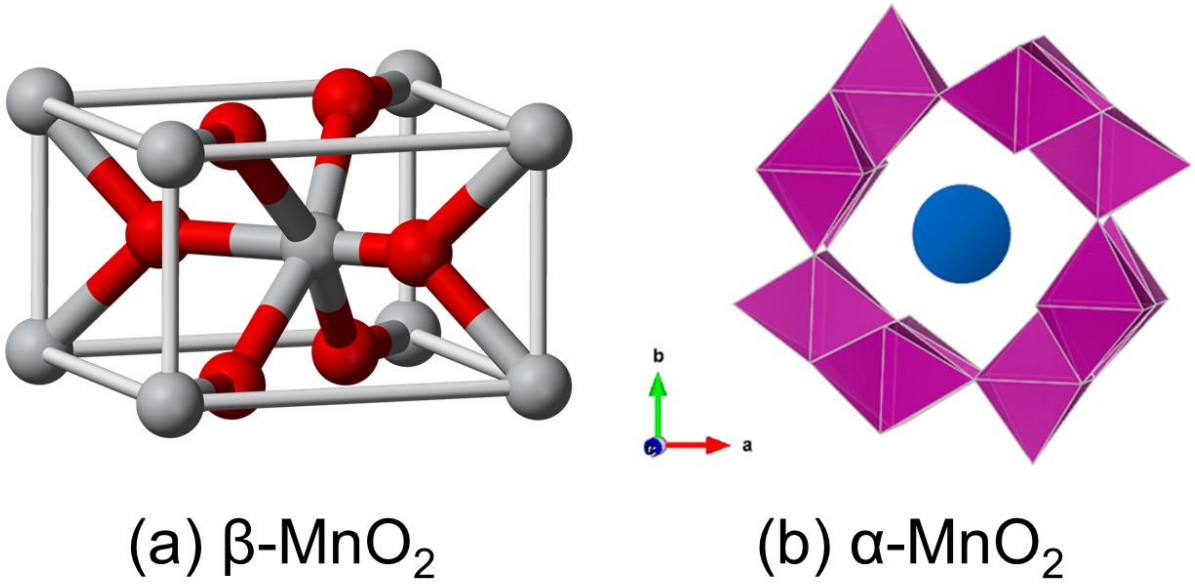

Figure 1.4. The crystal structures of (a) β-MnO_2 and (b) α-MnO_2 [49].

1.5 Common Dyes, Properties, and the Degradation Mechanisms

1.5.1 Dye definition and common dyes

A dye refers to a classic of organic compounds which enables other substances to obtain a bright and firm color by chemically bonding to the substrate. Dating back to the Neolithic period, humans have been using dyes for thousands of years. Natural dyes are usually derived from non-animal sources [50]. The first synthetic dye, Mauveine, was discovered by William Henry Perkin in 1856 [51]. In the 21st century, synthetic materials are widely used. Nowadays, dyes are usually used for the color of textiles, paints, cosmetics, foods, and other industries [52]. In addition, photo-sensitized dyes can be used for the dye-sensitized solar cell [53].

Rhodamine B (RhB, $C_{28}H_{31}ClN_2O_3$), also called Rhodamine 610, is a chemical compound and a synthetic dye. Figure 1.5(a) shows the molecular structure of RhB. The RhB solid is red to violet powder, while its aqueous solution is peach red. RhB is easily soluble in water and ethanol, slightly soluble in acetone, chloroform, hydrochloric acid, and sodium hydroxide solution. As one of the most popular dyes, RhB is widely used in the industry of textile, paper, paint, and so on [54]. In addition, RhB can be used as a biomarker for the wildlife vaccines to identify the vaccinated animals [55]. RhB is toxic. The effective and lethal concentration (EC_{50} and LC_{50}) locate in the range of 14 – 24 mg/L [56]. RhB is also in the IARC monographs of classification lists, recognized as 'Not classifiable as to its carcinogenicity to humans' [57].

Methylene blue (MB, $C_{16}H_{18}ClN_3S$), also known as methylthioninium chloride, is a chemical compound used as a dye and a medication. Figure 1.5(b) shows the molecular structure of MB. MB solid is dark green bronze lustrous crystal or powder, while its solution is blue-green. As a typical cation dye, MB is used in industries such as textile industry for coloring paper, dying cotton, wools, and so on [58]. Moreover, MB is also able to work as a medicine, treating methemoglobinemia. MB is also toxic, whose LC50 is 18 mg/L for fish. MB can do harm to the human body by causing eye burn, increasing heartbeat, vomiting, and diarrhea [59, 60].

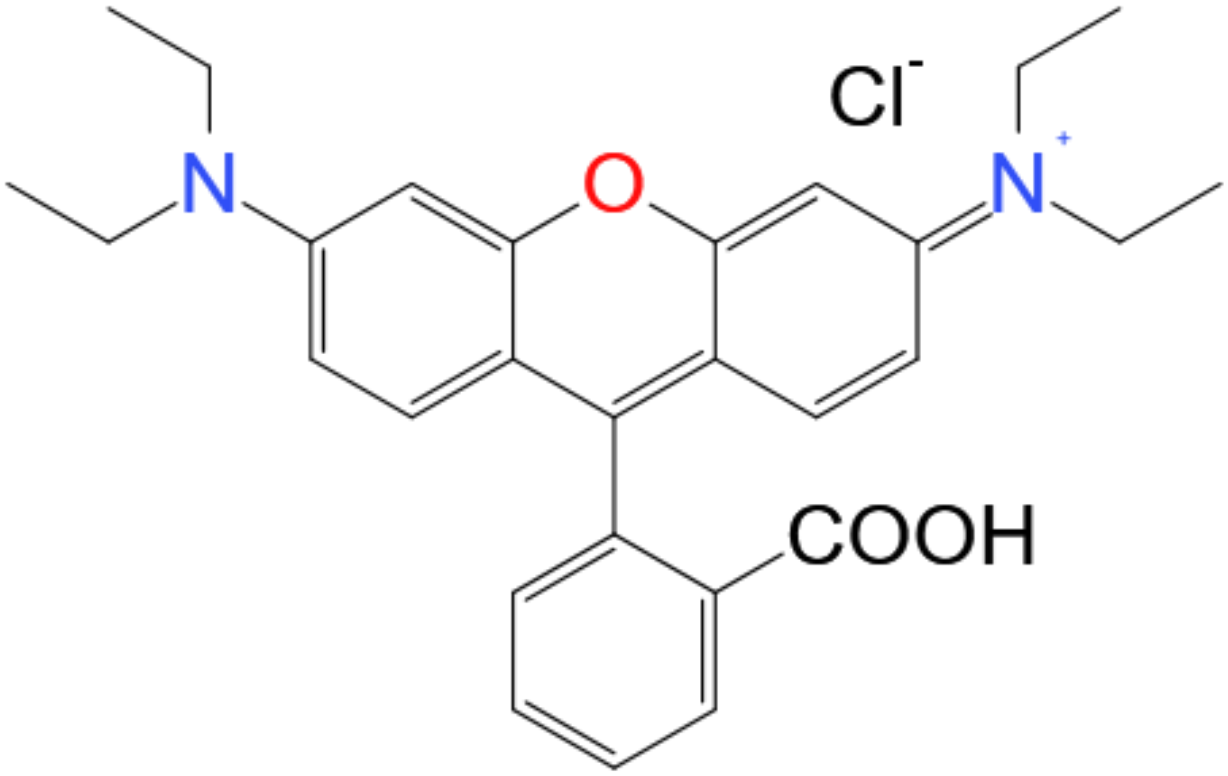

(a) Rhodamine B

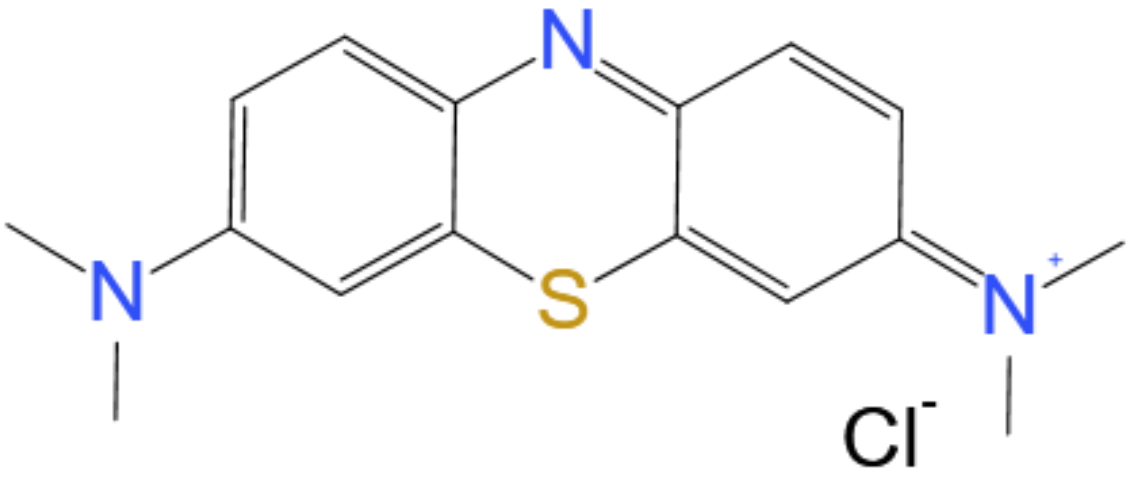

(b) Methylene blue

Figure 1.5. Structural formular of (a) RhB and (b) MB.

Dye pollution is one of the most disturbing industrial water pollution problems. The dyes not only affect the stability of the water biological chain, but also do harm to human health. Figure 1.6 shows the organic water pollutant emissions of east European countries [61]. Millions of tons of organic wastewater are discharged every day, and a large part of it is the pollution caused by dyes. This makes day degradation one of the urgent problems to be solved.

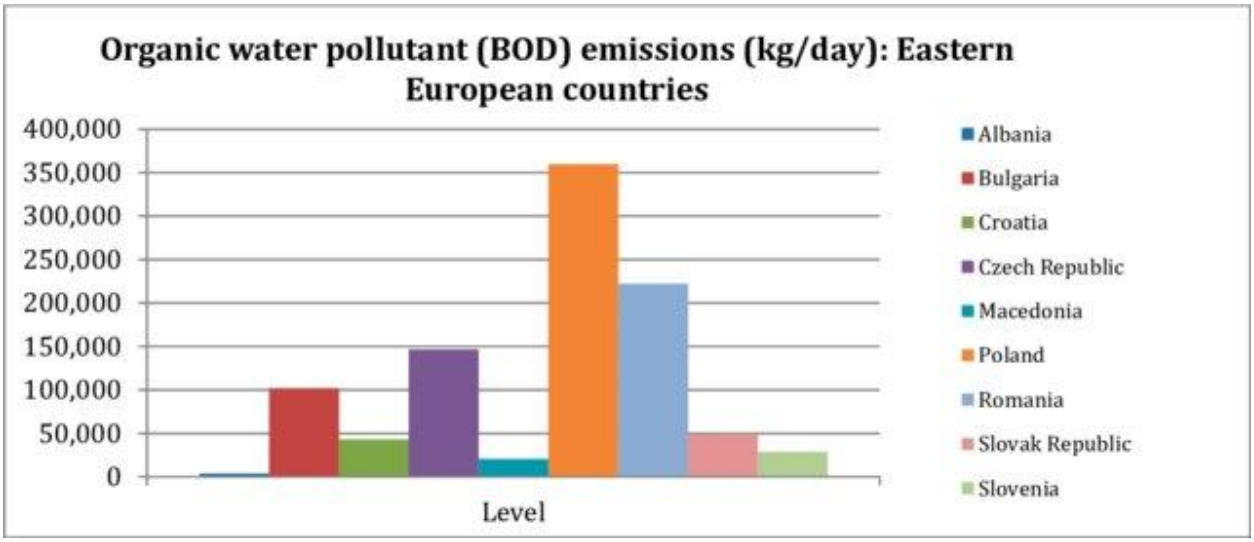

Figure 1.6. The organic water pollutant emissions by eastern European countries [61].

1.5.2 General dye degradation mechanisms

In order to solve the dye issues, several techniques, including biological and physicochemical methods, have been applied for the degradation. However, biological method has certain limitations and cannot treat wastewater containing high concentration of dyes [62], while chemical technology may cause secondary pollution. The advanced oxidation processes are considered as one of the promising methods for dye degradation [63]. After first proposed by Honda and Fujishima in 1972 [64], photocatalytic degradation of dyes have attracted the attention of many researchers. Until now, the research on the degradation of dyes by photocatalysis has become more and more mature. There are three types of mechanisms for the photodegradation of dyes [65-67]:

1. Dye sensitization
2. Indirect dye degradation by oxidation or reduction
3. Direct photolysis of dye

The mechanism of dye sensitization is shown in Figure 1.7(a) [63]. Dyes can absorb the electrons whose energy are equal to or greater than the bandgap of material, which makes the electrons excite from the valence band to the conduction band, forming a pair of electrons and

positive hole. Electrons and positive holes can interact with dye molecules and producing 'exciting dye', the converted to anionic or cationic radicals, followed by decomposition.

Indirect degradation is another pathway, which is shown in Figure 1.7(b) [63]. In this case, the electrons of metal oxide, rather than dyes, are excited to conduction band, forming electron pairs and positive holes. Both electrons and holes can react with water and fabricate hydroxyl radicals. Hydroxyl radicals are strong oxidizing agent, which is very effective for the decomposition of organic pollutants [68, 69].

$$\text{Metal Oxide} + h\nu \rightarrow h^+ + e^- \quad (1.12)$$

$$h^+ + H_2O \rightarrow \cdot OH + H^+ \quad (1.13)$$

$$\text{Dye} + \cdot OH \rightarrow \text{Degradation Product} \quad (1.14)$$

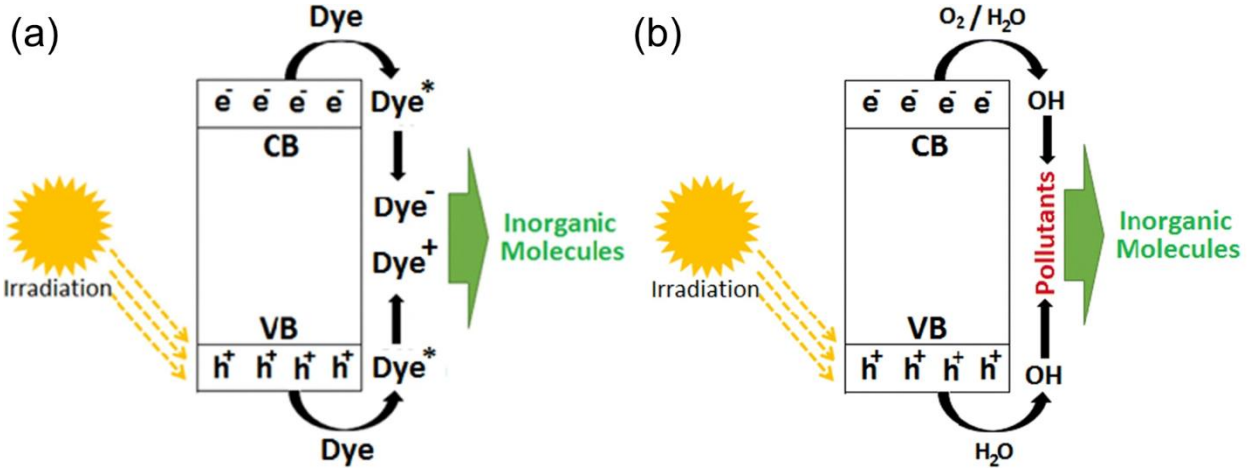

Figure 1.7. Mechanism of photocatalysis of pollutants by (a) direct dye sensitization and (b) indirect photodegradation [63].

1.6 Research Motivations and Objectives

Just as reported in the previous introduction, TiO_2 is one of the most used metal oxides for the photodegradation. Although P25 and other TiO_2 materials have been proved to have high photoactivity under UV because of the bandgap [70]. However, TiO_2 is not so effective when being illuminated by visible light [71]. Therefore, for this dissertation, the fabrication or modification method would be focused on, in order to improve the visible light activity of TiO_2.

In this dissertation, several modification methods have been applied for the enhancement of TiO_2 materials to broaden its absorption wavelength for light, and then improve its visible light utilization. **Chapter 1** gives a brief introduction about TiO_2 and other metal oxide materials,

together with some visible light applications. **Chapter 2** introduces two fabrication methods of TiO_2 – 'submerged photosynthesis of crystallites' and 'solution-plasma synthesis' – and discuss about the property increasement of visible light. **Chapter 3** introduces ellipsoidal TiO_2 (e-TiO_2), which is a new fabricated single crystal with enhanced visible light photodegradation activity. **Chapter 4** introduces a facile modification method, which is first used in e-TiO_2 fabrication, to modify different TiO_2 samples and increase their visible light activity. **Chapter 5** gives the conclusions of this dissertation and some prospects.

References

1. Bayda, S., et al., *The History of Nanoscience and Nanotechnology: From Chemical-Physical Applications to Nanomedicine.* Molecules (Basel, Switzerland), 2019. **25**(1): p. 112.

2. Buzea, C., I.I. Pacheco, and K. Robbie, *Nanomaterials and nanoparticles: Sources and toxicity.* Biointerphases, 2007. **2**(4): p. MR17-MR71.

3. Portela, C.M., et al., *Extreme mechanical resilience of self-assembled nanolabyrinthine materials.* Proceedings of the National Academy of Sciences of the United States of America, 2020. **117**(11): p. 5686-5693.

4. Sadri, R., et al., *A facile, bio-based, novel approach for synthesis of covalently functionalized graphene nanoplatelet nano-coolants toward improved thermo-physical and heat transfer properties.* Journal of Colloid and Interface Science, 2018. **509**: p. 140-152.

5. Chavali, M.S. and M.P. Nikolova, *Metal oxide nanoparticles and their applications in nanotechnology.* SN Applied Sciences, 2019. **1**(6): p. 607.

6. Vanýsek, P., *Electrochemical Series*, in *CRC Handbook of Chemistry and Physics 92nd Edition*, W.M. Haynes, Editor. 2011, CRC Press. p. 5-80-9.

7. Zumdahl, S.S. *Oxide*. Encyclopedia Britannica 1998 May 7th, 2018; Available from: https://www.britannica.com/science/oxide.

8. Rao, C.N.R., *Transition Metal Oxides.* Annual Review of Physical Chemistry, 1989. **40**(1): p. 291-326.

9. Lv, H., et al., *A brief introduction to the fabrication and synthesis of graphene based composites for the realization of electromagnetic absorbing materials.* Journal of Materials Chemistry C, 2017. **5**(3): p. 491-512.

10. Cheng, C.-S., H. Gomi, and H. Sakata, *Electrical and Optical Properties of Cr_2O_3 Films Prepared by Chemical Vapour Deposition.* physica status solidi (a), 1996. **155**(2): p. 417-425.

11. Cockayne, E. and L. Li, *First-principles DFT+U studies of the atomic, electronic, and magnetic structure of α-MnO_2 (cryptomelane).* Chemical Physics Letters, 2012. **544**: p. 53-58.

12. Sulania, I., et al., *Investigations of electrical and optical properties of low energy ion irradiated α-Fe_2O_3 (hematite) thin films.* AIP Conference Proceedings, 2016. **1731**(1): p. 120021.

13. Ravichandran, A.T., et al., *Morphology, Bandgap, and Grain Size Tailoring in Cu_2O Thin Film by SILAR Method.* IEEE Transactions on Nanotechnology, 2015. **14**(1): p. 108-112.

14. Dhineshbabu, N.R., et al., *Study of structural and optical properties of cupric oxide nanoparticles.* Applied Nanoscience, 2016. **6**(6): p. 933-939.

15. Kamarulzaman, N., M.F. Kasim, and R. Rusdi, *Band Gap Narrowing and Widening of ZnO Nanostructures and Doped Materials.* Nanoscale Research Letters, 2015. **10**(1): p. 346.

16. Bandaru, S., et al., *Tweaking the Electronic and Optical Properties of α-MoO_3 by Sulphur and Selenium Doping - a Density Functional Theory Study.* Scientific reports, 2018. **8**(1): p. 10144-10144.

17. Fujii, S., et al., *Selective fabrication of tungsten nano-oxides via submerged photosynthesis with hydrogen peroxide for chromic device application.* Materials Letters, 2021. **302**: p. 130344.

18. Pierre, P.D.S.S., *A Note on the Melting Point of Titanium Dioxide.* Journal of the American Ceramic Society, 1952. **35**(7): p. 188-188.

19. Anitha, V.C., A.N. Banerjee, and S.W. Joo, *Recent developments in TiO_2 as n- and p-type transparent semiconductors: synthesis, modification, properties, and energy-related applications.* Journal of Materials Science, 2015. **50**(23): p. 7495-7536.

20. *Titanium Dioxide Market Size, Share & Trends Analysis Report By Grade (Anatase, Rutile), By Production Process (Sulfate, Chloride), By Application (Paints & Coatings, Plastics), By Region, And Segment Forecasts, 2021 - 2028*. 2021 [cited 2022 05/10]; Available from: https://www.grandviewresearch.com/industry-analysis/titanium-dioxide-industry.

21. Hanaor, D.A.H., et al., *Ab initio study of phase stability in doped TiO_2.* Computational Mechanics, 2012. **50**(2): p. 185-194.

22. Diebold, U., *The surface science of titanium dioxide.* Surface Science Reports, 2003. **48**(5): p. 53-229.

23. Palfey, W.R., G.R. Rossman, and W.A. Goddard, *Structure, Energetics, and Spectra for the Oxygen Vacancy in Rutile: Prominence of the Ti–HO–Ti Bond.* The Journal of Physical Chemistry Letters, 2021. **12**(41): p. 10175-10181.

24. Assadi, M.H.N. and D.A.H. Hanaor, *Theoretical study on copper's energetics and magnetism in TiO_2 polymorphs.* Journal of Applied Physics, 2013. **113**(23): p. 233913.

25. Torres, P. and R. Rurali, *Thermal Conductivity of Rutile and Anatase TiO_2 from First-Principles.* The Journal of Physical Chemistry C, 2019. **123**(51): p. 30851-30855.

26. Hanaor, D.A.H. and C.C. Sorrell, *Review of the anatase to rutile phase transformation.* Journal of Materials Science, 2011. **46**(4): p. 855-874.

27. Wu, S., et al., *Exploring the Phase Transformation Mechanism of Titanium Dioxide by High Temperature in Situ Method.* IOP Conference Series: Materials Science and Engineering, 2019. **493**: p. 012010.

28. Assadi, M.H.N. and D.A.H. Hanaor, *The effects of copper doping on photocatalytic activity at (101) planes of anatase TiO_2: A theoretical study.* Applied Surface Science, 2016. **387**: p. 682-689.

29. Luttrell, T., et al., *Why is anatase a better photocatalyst than rutile? - Model studies on epitaxial TiO_2 films.* Scientific Reports, 2014. **4**(1): p. 4043.

30. Batzill, M., *Fundamental aspects of surface engineering of transition metal oxide photocatalysts.* Energy & Environmental Science, 2011. **4**(9): p. 3275-3286.

31. Wilson, J.N. and H. Idriss, *Effect of surface reconstruction of TiO_2(001) single crystal on the photoreaction of acetic acid.* Journal of Catalysis, 2003. **214**(1): p. 46-52.

32. Wilson, J.N. and H. Idriss, *Structure Sensitivity and Photocatalytic Reactions of Semiconductors. Effect of the Last Layer Atomic Arrangement.* Journal of the American Chemical Society, 2002. **124**(38): p. 11284-11285.

33. Giocondi, J.L., P.A. Salvador, and G.S. Rohrer, *The origin of photochemical anisotropy in $SrTiO_3$.* Topics in Catalysis, 2007. **44**(4): p. 529-533.

34. Jiang, X., et al., *Anatase and rutile in evonik aeroxide P25: Heterojunctioned or individual nanoparticles?* Catalysis Today, 2018. **300**: p. 12-17.

35. Raj, K.J.S. and B. Viswanathan, *Effect of surface area, pore volume and particle size of P25 titania on the phase transformation of anatase to rutile.* Indian journal of chemistry. Sect. A: Inorganic, physical, theoretical & analytical, 2009. **48**: p. 1378-1382.

36. Nica, I.C., et al., *Interaction of New-Developed TiO_2-Based Photocatalytic Nanoparticles with Pathogenic Microorganisms and Human Dermal and Pulmonary Fibroblasts.* International Journal of Molecular Sciences, 2017. **18**(2).

37. Suttiponparnit, K., et al., *Role of Surface Area, Primary Particle Size, and Crystal Phase on Titanium Dioxide Nanoparticle Dispersion Properties.* Nanoscale research letters, 2011. **6**(1): p. 27-27.

38. Ohtani, B., et al., *What is Degussa (Evonik) P25? Crystalline composition analysis, reconstruction from isolated pure particles and photocatalytic activity test.* Journal of Photochemistry and Photobiology A: Chemistry, 2010. **216**(2): p. 179-182.

39. Hurum, D.C., et al., *Explaining the Enhanced Photocatalytic Activity of Degussa P25 Mixed-Phase TiO_2 Using EPR.* The Journal of Physical Chemistry B, 2003. **107**(19): p. 4545-4549.
40. Erik Lassner, W.-D.S., *Tungsten: Properties, Chemistry, Technology of the Element, Alloys, and Chemical Compounds*. 1999, New York: Springer New York. XXI, 422.
41. Williams, M., *The Merck Index: an Encyclopedia of Chemicals, Drugs, and Biologicals. 14th Edition. Merck Inc., Whitehouse Station/Rahway, New Jersey, October 2006. Cloth 0-911910-00X. $125. pp. 2564.* Drug Development Research, 2006. **67**(11): p. 870-870.
42. Williams, D.E., et al., *Modelling the response of a tungsten oxide semiconductor as a gas sensor for the measurement of ozone.* Measurement Science and Technology, 2002. **13**(6): p. 923-931.
43. Lee, W.J., et al., *Effects of surface porosity on tungsten trioxide(WO_3) films' electrochromic performance.* Journal of Electronic Materials, 2000. **29**(2): p. 183-187.
44. Patel, K., et al., *All-solid-thin film electrochromic devices consisting of layers ITO/NiO/ZrO_2/WO_3/ITO.* Journal of Nano- and Electronic Physics, 2013. **5**.
45. Wriedt, H.A., *The O-W (oxygen-tungsten) system.* Bulletin of Alloy Phase Diagrams, 1989. **10**(4): p. 368-384.
46. Haynes, W.M., *CRC Handbook of Chemistry and Physics, 97th Edition.* 2016.
47. Greenwood, N.N., et al., *Chemistry of the Elements*. 1984: Butterworth-Heinemann.
48. Broughton, D.B., R.L. Wentworth, and M.E. Laing, *Mechanism of Decomposition of Hydrogen Peroxide Solutions with Manganese Dioxide. II.* Journal of the American Chemical Society, 1947. **69**(4): p. 744-747.
49. Housel, L.M., et al., *Investigation of α-MnO_2 Tunneled Structures as Model Cation Hosts for Energy Storage.* Accounts of Chemical Research, 2018. **51**(3): p. 575-582.
50. Burgess, R. and P. Green, *Harvesting Color: How to Find Plants and Make Natural Dyes*. 2011: Artisan.
51. Travis, A.S., *Perkin's Mauve: Ancestor of the Organic Chemical Industry.* Technology and Culture, 1990. **31**(1): p. 51-82.
52. Nikfar, S. and M. Jaberidoost, *Dyes and Colorants*, in *Encyclopedia of Toxicology (Third Edition)*, P. Wexler, Editor. 2014, Academic Press: Oxford. p. 252-261.
53. O'Regan, B. and M. Grätzel, *A low-cost, high-efficiency solar cell based on dye-sensitized colloidal TiO_2 films.* Nature, 1991. **353**(6346): p. 737-740.

54. Hao, Z., et al., *Nanosize α-Bi_2O_3 decorated Bi_2MoO_6 via an alkali etching process for enhanced photocatalytic performance.* RSC Advances, 2015. **5**(16): p. 12346-12353.
55. Slate, D., et al., *Oral Rabies Vaccination in North America: Opportunities, Complexities, and Challenges.* PLOS Neglected Tropical Diseases, 2009. **3**(12): p. e549.
56. Skjolding, L.M., et al., *Assessing the aquatic toxicity and environmental safety of tracer compounds Rhodamine B and Rhodamine WT.* Water Research, 2021. **197**: p. 117109.
57. International Agency for Research on Cancer. *Agents classified by the IARC Monographs, Volumes 1–131*. List of Classifications 2022 [cited 2022 05/16]; Available from: https://monographs.iarc.who.int/list-of-classifications/.
58. Mulushewa, Z., W.T. Dinbore, and Y. Ayele, *Removal of methylene blue from textile waste water using kaolin and zeolite-x synthesized from Ethiopian kaolin.* Environmental analysis, health and toxicology, 2021. **36**(1): p. e2021007.
59. Velmurugan, P., V. Kumar, and G. Dhinakaran, *Dye removal from aqueous solution using low cost adsorbent.* Int. J. Environ. Sci., 2011. **1**: p. 1492-1503.
60. Umoren, S., U. Etim, and A.U. Israel, *Adsorption of methylene blue from industrial effluent using poly (vinyl alcohol).* Journal of Materials and Environmental Science, 2013. **4**: p. 75-86.
61. Paraschiv, D., C. Tudor, and R. Petrariu, *The Textile Industry and Sustainable Development: A Holt–Winters Forecasting Investigation for the Eastern European Area.* Sustainability, 2015. **7**(2).
62. Garcia, B.B., et al., *Photocatalytic degradation of swine wastewater on aqueous TiO_2 suspensions: optimization and modeling via Box-Behnken design.* Heliyon, 2020. **6**(1): p. e03293.
63. Saeed, M., et al., *Photocatalysis: an effective tool for photodegradation of dyes—a review.* Environmental Science and Pollution Research, 2022. **29**(1): p. 293-311.
64. Fujishima, A. and K. Honda, *Electrochemical Photolysis of Water at a Semiconductor Electrode.* Nature, 1972. **238**(5358): p. 37-38.
65. Pingmuang, K., et al., *Composite Photocatalysts Containing $BiVO_4$ for Degradation of Cationic Dyes.* Scientific Reports, 2017. **7**(1): p. 8929.
66. Isac, L., et al., *Copper Sulfide Based Heterojunctions as Photocatalysts for Dyes Photodegradation.* Frontiers in Chemistry, 2019. **7**.
67. Pavithra, K.G., et al., *Removal of colorants from wastewater: A review on sources and treatment strategies.* Journal of Industrial and Engineering Chemistry, 2019. **75**: p. 1-19.

68. Ng, K.H., et al., *TiO_2 and ZnO photocatalytic treatment of palm oil mill effluent (POME) and feasibility of renewable energy generation: A short review.* Journal of Cleaner Production, 2019. **233**: p. 209-225.
69. Al-Mamun, M.R., et al., *Photocatalytic activity improvement and application of UV-TiO_2 photocatalysis in textile wastewater treatment: A review.* Journal of Environmental Chemical Engineering, 2019. **7**(5): p. 103248.
70. Zaleska, A., *Doped-TiO_2: A Review.* Recent Patents on Engineering, 2008. **2**(3): p. 157-164.
71. Humayun, M., et al., *Modification strategies of TiO_2 for potential applications in photocatalysis: A critical review.* Green Chemistry Letters and Reviews, 2018. **11**(2): p. 86-102.

Chapter 2

TiO_2 Fabricated by Submerged Photosynthesis of Crystallites and Solution Plasma Synthesis

2.1 General Introduction

Exploration of solar-driven functional materials is currently a hot topic in many fields like solar energy utilization, photocatalysis, synthetic chemistry, optoelectronics, and environmental science. Among various photosensitive materials, titanium dioxide (TiO_2) has been widely used owing to its nontoxicity and low cost. However, pristine white TiO_2 photocatalysts have absorption only in ultraviolet (UV) regime due to their wide bandgap (anatase: ~3.2 eV, rutile: ~3.0 eV), which greatly limits their application under solar irradiation. Doping of foreign atoms is a commonly used method to introduce sub-bands into TiO_2 to enhance light absorption at a broader range of wavelength [1-3]. Without introducing impurities, self-structured modification is becoming a new strategy in tuning optical and electrical properties of TiO_2 [4]. Hydrogenated black TiO_2 with structural disordered surface, reported by Chen et al., exhibits good solar absorption ability [5]. However, the current mainstream fabricating methods for obtaining black TiO_2 are multi-step and require severe experimental conditions, such as high-temperature annealing and oxygen-free atmospheric condition [6].

No need for complicated operations, plasma electrolysis in solution with a metal electrode as the raw material was used in nanomaterial synthesis of metals, semi-metals, and metal oxides, which was also named as solution plasma process (SPP) [7-11]. The nanomaterial formation in these synthetic systems was based on a melting/evaporation-quenching mechanism, in which the concentrated current flow sharply increased the local temperature of current spots on the electrode by Joule heating, thus resulting in the local melting of the metal electrode. The molten electrode fraction was quenched in the liquid phase and transformed into the target nano/micro particles [12, 13]. The SPP method has been applied for the synthesis and activation of TiO_2 nanoparticles. Several groups synthesized defected black TiO_2 particles in a direct current (DC) excited plasma in solution with a titanium cathode [12, 13] or using two symmetric titanium electrodes with a bipolar-pulsed power supply [14-16]. In those studies, black TiO_2 particles were formed from Ti electrodes based on a top-down synthetic strategy. A recent study conducted by Yu et al. showed that the SPP method could be used for the incorporation of hydrogen dopant into pre-synthesized

oxygen-vacancy rich TiO_2 nanoparticles to create shallow-level defects [17]. The resulting colored TiO_2 nanoparticles exhibited much higher photocatalytic ability over CO_2 reduction and acetaldehyde removal under solar irradiation. However, until now, there is still no clear mechanism study on the formation or modification process in black TiO_2 synthesis through the SPP method.

Submerged photosynthesis of crystallites (SPSC) is a new pathway for the fabrication of metal oxide materials. First proposed by Jeem et al. [18], SPSC method is based on the submerged liquid plasma process. After the fabrication of metal oxide 'seeds' by plasma process, UV light is used for the growth of metal oxides in the water. Up to now, SPSC method has been successfully used in the fabrication of ZnO, Fe_2O_3, CuO and other metal oxides [19-22]. Generally, SPSC method can be summed up in the following equations [18]:

$$\text{Semiconductor} + h\nu \rightarrow h^+ + e^- \quad (2.1)$$

$$H_2O + h^+ \rightarrow \cdot OH + H^+ \quad (2.2)$$

$$\cdot OH + e^- \rightarrow OH^- \quad (2.3)$$

These three equations represent the band gap excitation (equation 2.1), water dissociation (equation 2.2), and hydroxyl radical reduction (equation 2.3), respectively. Equation 2.1 – 2.3 reveal the mechanism of water splitting in the presence of light, which can be summarized as:

$$H_2O + h\nu \rightarrow H^+ + OH^- \quad (2.4)$$

After the water splitting, OH^- is able to react with metal ions and form metal oxide.

Herein, we first synthesized black TiO_2 nanoparticles (b-TiO_2) through a facile SPP method using DC-excited plasma in an aqueous KOH electrolyte solution with a titanium plate cathode. After SPP, the black TiO_2 was otherwise collected, and the titanium cathode was added into water for the SPSC method. A voltage was applied on the Ti electrode in order to increase the reaction rate. Both b-TiO_2 fabricated by SPP method and TiO_2 fabricated by SPSC method were collected for the further research.

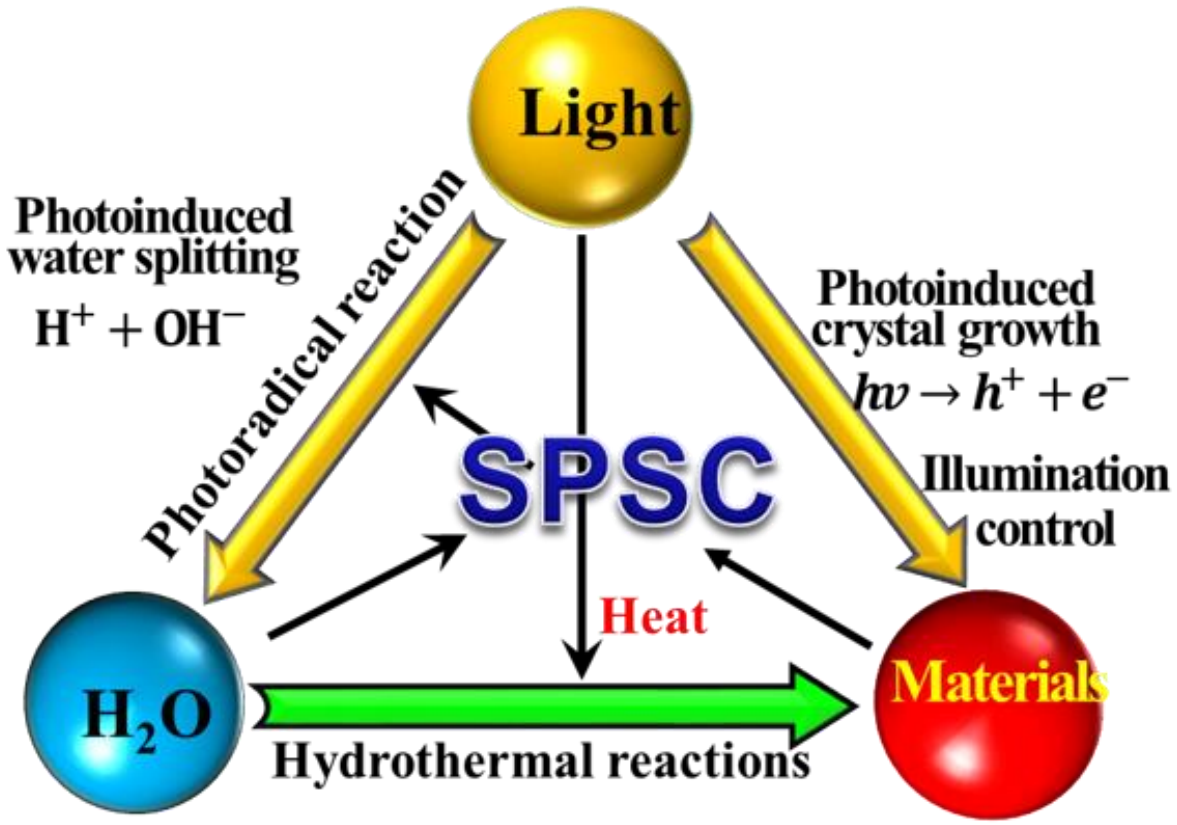

Figure 2.1. Mechanism of SPSC method [18].

2.2 Experimental Section

2.2.1 Solution Plasma of TiO_2

Figure 2.2(a) shows the experimental setup of solution plasma device for TiO_2 fabrication. A Ti plate (30 × 5 × 0.5 mm, 99.5%, NILACO, Japan) and an arc-shape Pt mesh (produced by Pt wire, 0.5 mm diameter, 1000 mm length) were used as cathode and anode, respectively. Then the Ti cathode supported by Cu wire (1 mm diameter, 99.5%, NILACO, Japan) was placed at the center of a glass beaker (300 mL), with the 30-mm cathode-anode distance. 300 mL of 0.1 M KOH aqueous solution (Wako, Japan) was heated to 80°C as the electrolyte. The plasma was generated near the Ti cathode while applying a voltage of 140 V using a regulated DC power generator (Kikusui, PWR1600H, Japan). The obtained TiO_2 particle suspension was centrifuged and purified with deionized water three times and dried in an oven at 50°C for 12 hours. The deionized water was produced by an ultrapure water system (> 18.2 MΩ, RFU424CB, ADVANTEC, Japan). All the chemicals were used as received without purification.

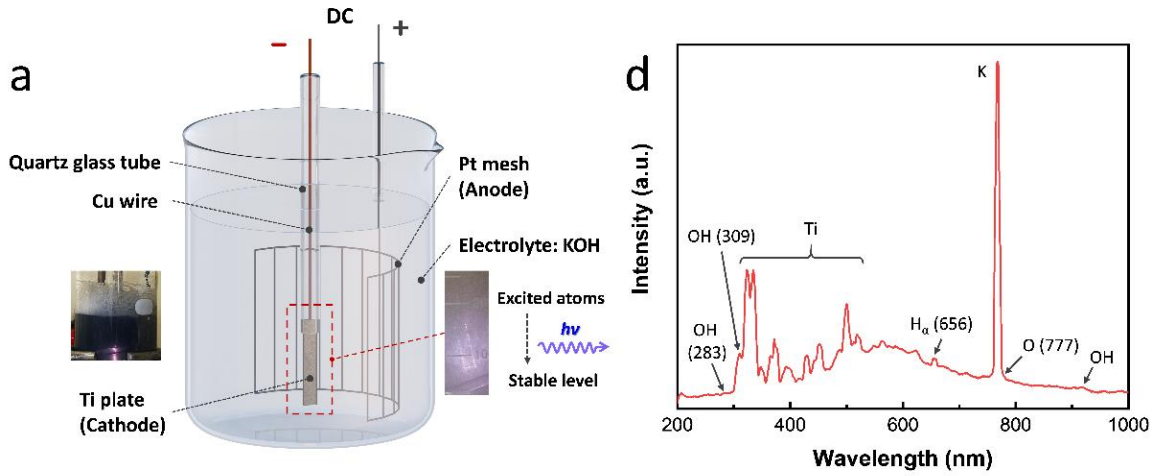

Figure 2.2. (a) Experimental setup for the SPP synthesis of b-TiO_2. The inset images show the b-TiO_2 suspension after SPP synthesis (left) and the plasma emission (right). (b) Optical emission spectrum (OES) of the plasma in the SPP synthesis of b-TiO_2.

2.2.2 Electrochemical SPSC fabrication of TiO_2

After the plasma process, the Ti cathode was cleaned and collected for the electrochemical SPSC fabrication. In a Metrohm Autolab three-electrode system, Ti plate after plasma was used as the working electrode (WE), while a square-shape Pt foil (10 × 10 mm) worked as the counter electrode (CE), and a silver chloride electrode (SCE, Ag/AgCl/Cl^-) was chosen as the reference electrode (RE). 50 mL of the 3.5 wt% sodium chloride aqueous solution (NaCl, Hayashi Pure Chemical Ind. Ltd.) worked as the electrolyte. Two steps are taken for the electrochemical SPSC method. At first, the whole device was put into a dark chamber for 72 hours, with a voltage of 5 V for the dissolving step. Then, a UV light source (300 – 360 nm, HAMAMATSU Lightningcure) was applied on the Ti surface for another 72 hours, together with a voltage of -1 V for the deposition process. After these two steps, the Ti plate was collected and cleaned for the further characterization.

2.2.3 Characterizations

The morphologies of b-TiO_2 and SPSC TiO_2 were examined by using a JEOL JSM-7001F scanning electron microscope (SEM) operated at 15 kV and a JEOL JEM-2000FX transmission electron microscope (TEM) operated at 200 kV. High-resolution transmission electron microscopy (HRTEM) images were taken by using a JEOL JEM-2100F TEM operated at 200 kV. X-ray diffraction (XRD) patterns were collected by using a RIGAKU Miniflex X-ray diffractometer with the Cu Kα radiation, λ = 1.5418 Å, as the source. X-ray fluorescence spectrometry (XRF) was

measured by using a JEOL JSX-3100RII spectrometer. UV-VIS-NIR absorption spectrums were recorded using a JASCO V-770 spectrophotometer. Raman spectrum was measured by using a HORIBA XploRA PLUS Raman microscope. A JEOL JPS-9200 photoelectron spectrometer with monochromatic Al Kα radiation was used for X-ray photoelectron spectroscopy (XPS). The optical emission spectrum (OES) of plasma was obtained by using a USB-2000+ visible-light spectrophotometer (Ocean Optics). The contact angle measurements were done by using a DropMaster contact angle meter (KYOWA).

2.3 Results and Discussion

2.3.1 The characterization of b-TiO_2

The b-TiO_2 fabricated by SPP method in KOH electrolyte exhibits deep dark blue color, which is shown in the inset image of Figure 2.3(c). The X-ray diffraction pattern (XRD) shows a mix-phase structure, in which peaks located at 25° and 56° indicate the existence of anatase, while 36°, 42°, 54°, and 57° represent the rutile. In special, the peak at 29° shows a high intensity, which corresponds to the oxygen-deficient phase (ODP) of TiO_2. Figure 2.3(c) and (d) display the SEM and TEM images of b-TiO_2, showing the spherical morphology and broad size distribution. The lattice spaces of 2.49 Å and 2.28 Å shown in the HRTEM image of b-TiO_2 could be indexed to rutile plane (1 0 1) and rutile plane (2 0 0), while the lattice space 2.01 Å is attributed to the ODP of TiO_2 (Figure 2.3e). The blurred fringe of the particle suggests the amorphous phase on the b-TiO_2 particle surface. Figure 2(b) shows the Raman spectrum of b-TiO_2. Three broad bands centered at 441.5, 509.2, and 620.9 cm^{-1} were attributed to the Raman active modes of B_{1g} (A) with E_g (R), A_{1g} + B_{1g} (A), and A_{1g} (R) with E_g (A), respectively (hereinafter (A) and (R) refer to anatase and rutile phase). The broadening of these bands indicates the existence of the disordered phase of TiO_2. The bands that located at 171. 9 and 269.0 cm^{-1} were attributed to the ODP of TiO_2. Figure 2.4 shows the XPS O 1s spectrum of b-TiO_2. A large proportion of Ti^{3+}-O and Ti-OH species, indicating the existence of a large number of defects.

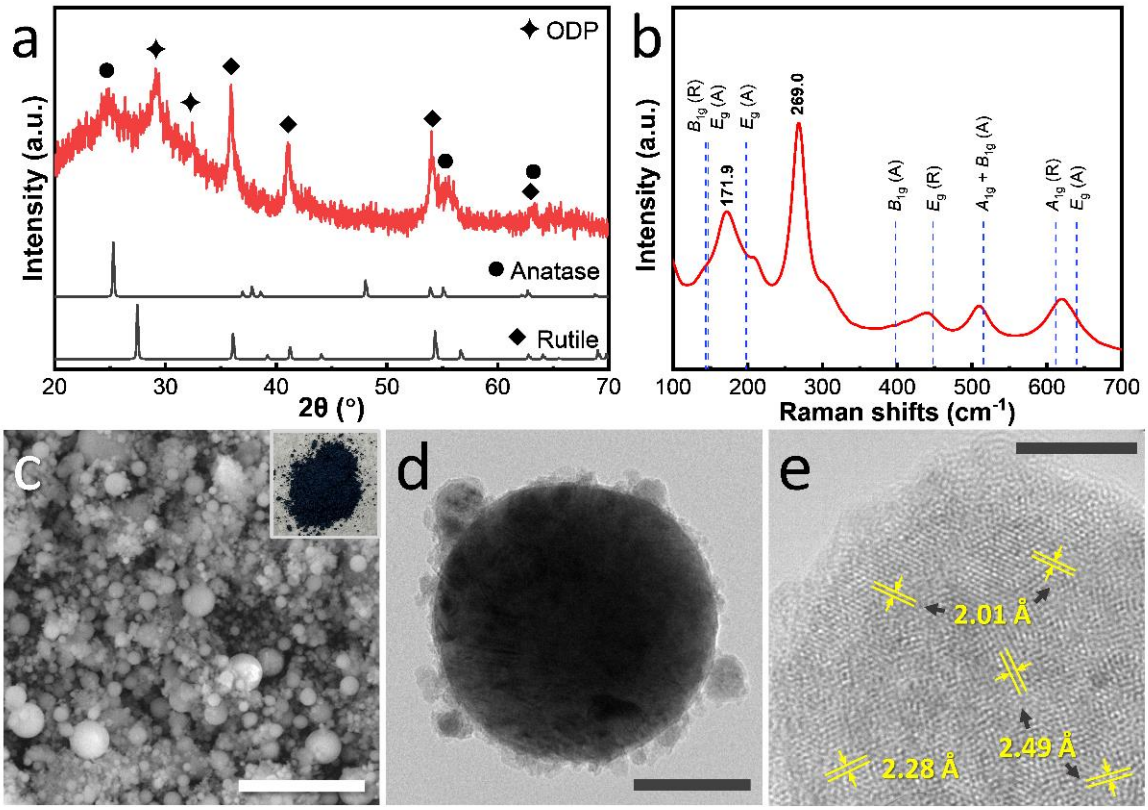

Figure 2.3. The XRD pattern (a), Raman spectrum (b), SEM (c), TEM (d), and HRTEM (e) images of as-prepared SPP synthesized b-TiO_2. The inset image in (b) shows the black-powder like b-TiO_2 sample. Scale bars shown in (c), (d), and (e) are 5 μm, 100 nm, and 5 nm, respectively.

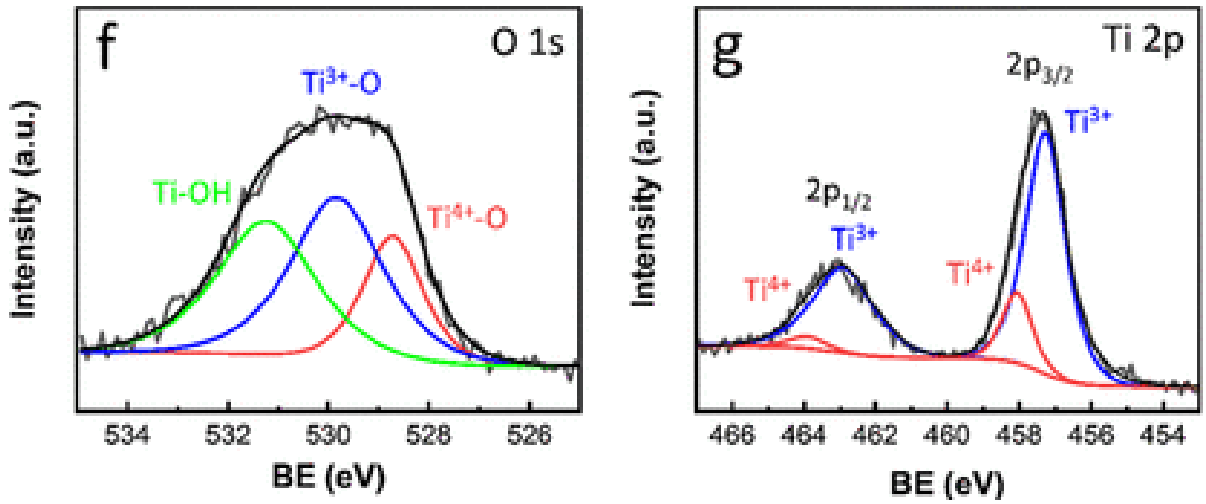

Figure 2.4. The XPS O 1s and Ti 2p spectrum of b-TiO_2.

The as-synthesized b-TiO_2 shows an excellent property for the absorption of solar light. Figure 2.5(a) shows the UV-vis-NIR spectra of b-TiO_2. Compared to commercial P25, b-TiO_2 has a high

light absorption, especially in vis-NIR range. Figure 2.5(b) shows the Tauc's plot transformed from UV-vis-NIR. The SPP synthesized b-TiO_2 gets a smaller bandgap compared to P25 according to the Tauc's plot [23].

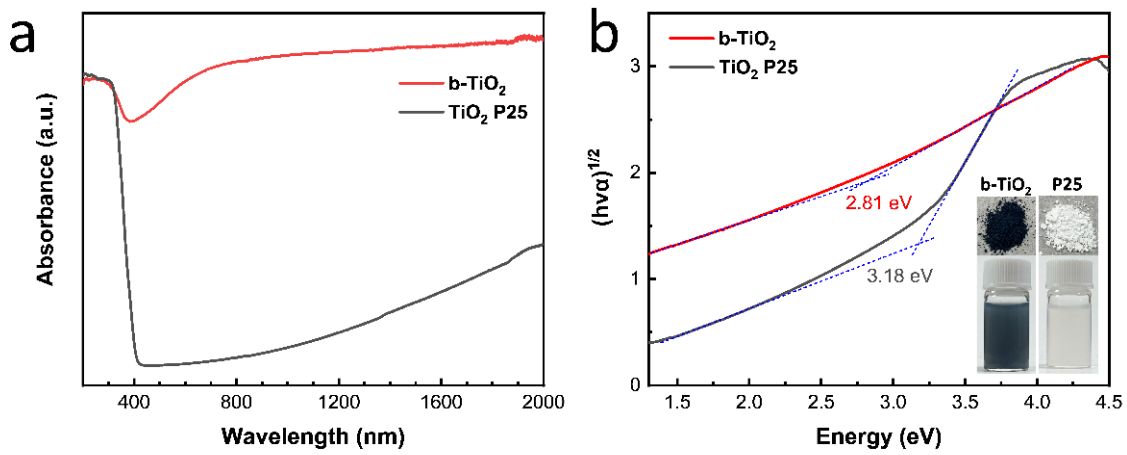

Figure 2.5. (a) A broader absorption of b-TiO_2 in the UV-vis-NIR regime compared with the absorption spectrum of commercially available TiO_2 P25; (b) the Tauc plot if b-TiO_2 and TiO_2 P25 reference.

In our experiment, it is found that radicals play an important role in the fabrication of b-TiO_2, which is generated in the plasma process. It is well known that ·H and ·OH radicals can be formed through multiple processes during the plasma. For example, it has been proved that water can split during the SPP synthesis in aqueous electrolyte as Equation 2.5 [24]:

$$H_2O \rightarrow \cdot H + \cdot OH \tag{2.5}$$

Furthermore, during the electrolysis and evaporation of water happened in SPP method, H_2 gas and water vapor are generated and upwelling around the Ti electrode. Meanwhile, O_2 gas and small water vaper are formed at the anode. The discharge in the liquid can ignite H_2 near the Ti cathode [25], making the thermal decomposition of H_2 in the plasma region and form hydrogen radical ·H, as Equation 2.6 [26].

$$H_2 \rightarrow \cdot H + \cdot H \tag{2.6}$$

To investigate the role of radicals (·H and ·OH) in the fabrication of b-TiO_2 via SPP, short-chain alcohols are introduced to remove the effects of highly reactive radicals. The chosen short-chain alcohols, such as methanol, ethanol, and 1-propanol, have a strong ability for radical scavenging. The following reaction can occur after this addition [27]:

$$ROH + \cdot H \rightarrow \cdot RO + H_2 \quad (2.7)$$

$$ROH + \cdot OH \rightarrow \cdot RO + H_2O \quad (2.8)$$

whereas "R" represents a carbon chain. The presence of alcohol molecules could transform highly reactive ·H and ·OH radicals to stable alcohol radicals (·ROH). As shown in Figure 2.2(b), the OES result of plasma in typical SPP synthesis of b-TiO_2 indicates that the plasma zone is filled with species including ·H, ·OH radicals, and atomic O [13, 28].

Notably, the amount of black precipitate is significantly reduced after the addition of alcohol. Methanol, ethanol, and 1-propanol are used to create different radical environments for the SPP synthesis of b-TiO_2. Figure 2.6 shows the inhibitory effect of alcohol addition on the formation of b-TiO_2. All three alcohols involved in SPP reduced the formation of b-TiO_2 and the mass loss of the Ti cathode. The suppression effect is found to be inversely related to the carbon number in these n-alcohols with a molar ratio of 0.01 (alcohol: water). In addition, as shown in Figure 2.7, while using ethanol as electrolyte, the supernatant of solution would turn yellow, which is different from KOH electrolyte. Figure 2.8 shows the XRF results. No Ti-based species are detected in the supernatant after SPP synthesis of b-TiO_2.

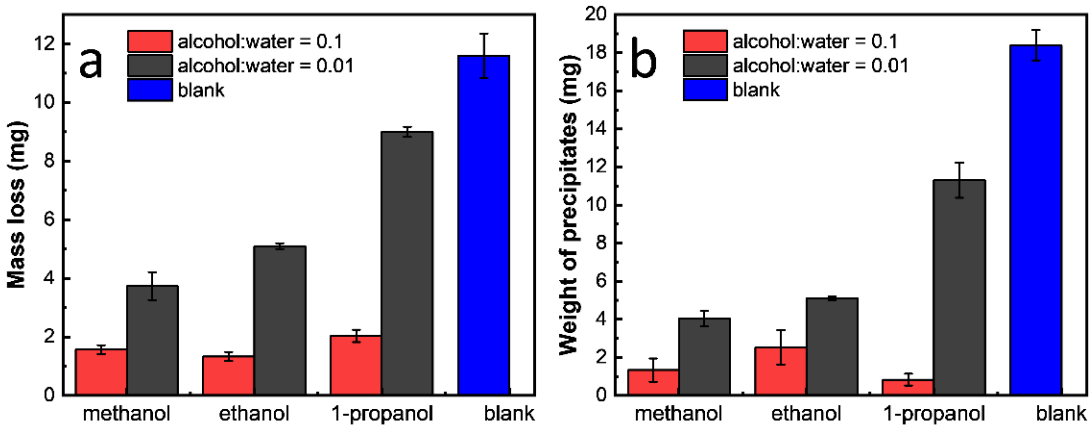

Figure 2.6. Effects of alcohol addition in electrolyte on the production of b-TiO_2 through the SPP method. (a) The mass loss of Ti electrode and (b) the weight of precipitates after centrifugation after SPP for 20 min. The parameter of "0.1" and "0.01" refer to the molar ratio of alcohol and water in the electrolyte. The blank sample was in the condition of using aqueous KOH (0.1 M) as the electrolyte (typical synthesis of b-TiO_2 through the SPP method).

Figure 2.7. Image of dark yellow supernatant of SPP synthesis of b-TiO_2 in water-ethanol electrolyte.

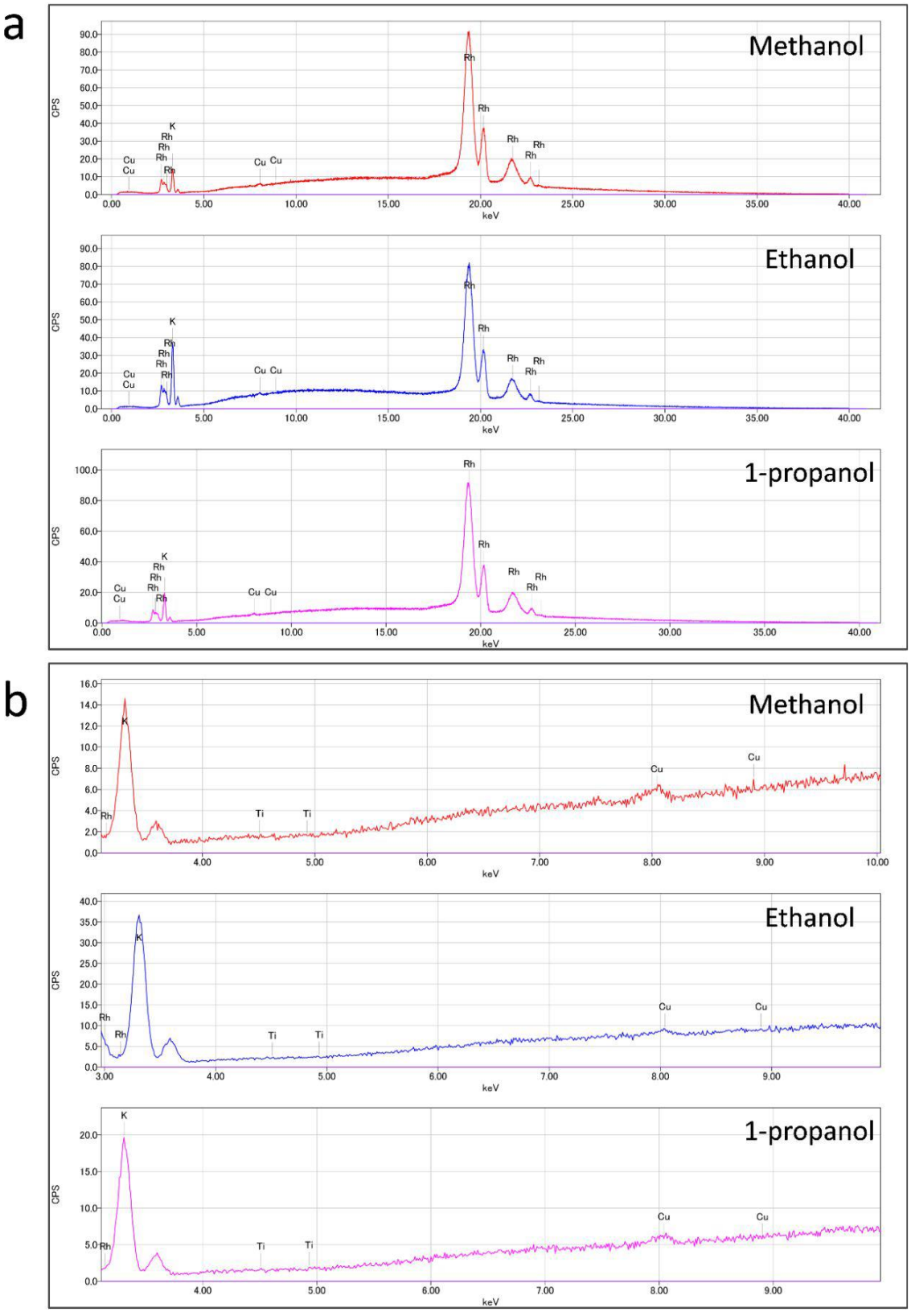

Figure 2.8. XRF element analysis of supernatant of SPP synthesis in alcohol-water mixed solution.

At the same time, the Ti electrode surface after SPP synthesis has obvious characteristics between the electrolyte with and without short chain alcohol (the molar ratio of alcohol to water is 1:10). After a typical SPP synthesis of black TiO_2 particles in KOH aqueous solution without alcohol addition, it is found that the Ti electrode (hereinafter named as 'Ti-Std') is covered by a black layer, which is shown in Figure 2.9(a). It is observed that the introduction of alcohols leads to the formation of dark yellow color on the electrode surface (hereinafter referred to as samples "Ti-Me", "Ti-Et" and "Ti-Pr" with the introduction of methanol, ethanol and 1-propanol in the electrolyte solvent, respectively) (Figure 2.9b-d). According to the optical microscopy and SEM images (Figure 2.10a&b), Ti-Std samples show relatively smooth and dense surfaces with micron sized pores, while Ti-Me, Ti-Et and Ti-Pr samples show cracks and nano sized pores on the coarser surfaces. The corresponding XRD patterns and Raman spectra revealed significant differences in surface conditions after the introduction of alcohol in different electrolyte compositions (Figure 2.10c&d). No obvious peak corresponding to anatase or rutile phase are found in all Ti electrode samples. The diffraction peaks marked by blue arrows are attributed to the presence of ODPs of TiO_2, including Ti_6O_{11}, Ti_8O_{13}, $Ti_{13}O_{22}$, and $Ti_{19}O_{30}$. The high relative peak intensity at 36.2° indicates a large amount of TiO_2 ODPs formed. In the XRD patterns of all Ti electrode samples after SPP synthesis, the two overlapping peak groups are concentrated at 34.9°, 39.9°, 52.4°, 62.7°, 69.7°, 75.7°, 77.0°, 86.2° and 35.1°, 40.2°, 52.9°, 63.0°, 70.6°, 76.2°, 77.4°, 86.9° due to the gap structure of Ti_6O (JCPDS No. 01-072-1907) and metal Ti (JCPDS No. 44-1294) (Fig. 2.10c) [29]. The peaks at 37.3 and 43.5° are related to TiO_2 (JCPDS No. 08-0117), indicating that in our experiment, a cubic TiO_2 phase is formed on the Ti electrode under all SPP conditions [30, 31]. Therefore, no Raman active modes of anatase and rutile were found in all titanium electrode samples (Fig. 2.10c). In the Ti-Std samples, the disorder induced broadband at 146, 179, 214, 351 and 594 cm^{-1} indicate the formation of defect rich TiO_2 characteristics corresponding to the XRD results. The two broad bands centered at 230 and 450 cm^{-1} in the samples Ti-Me, Ti-Et and Ti-Pr are the characteristics of the highly disordered phase of titanium oxide [32, 33]. Compared with Ti-Me, Ti Et and Ti-Pr, XPS O 1s of Ti Std electrode shows a significantly larger proportion of Ti-OH (shown in Figure 2.10e).

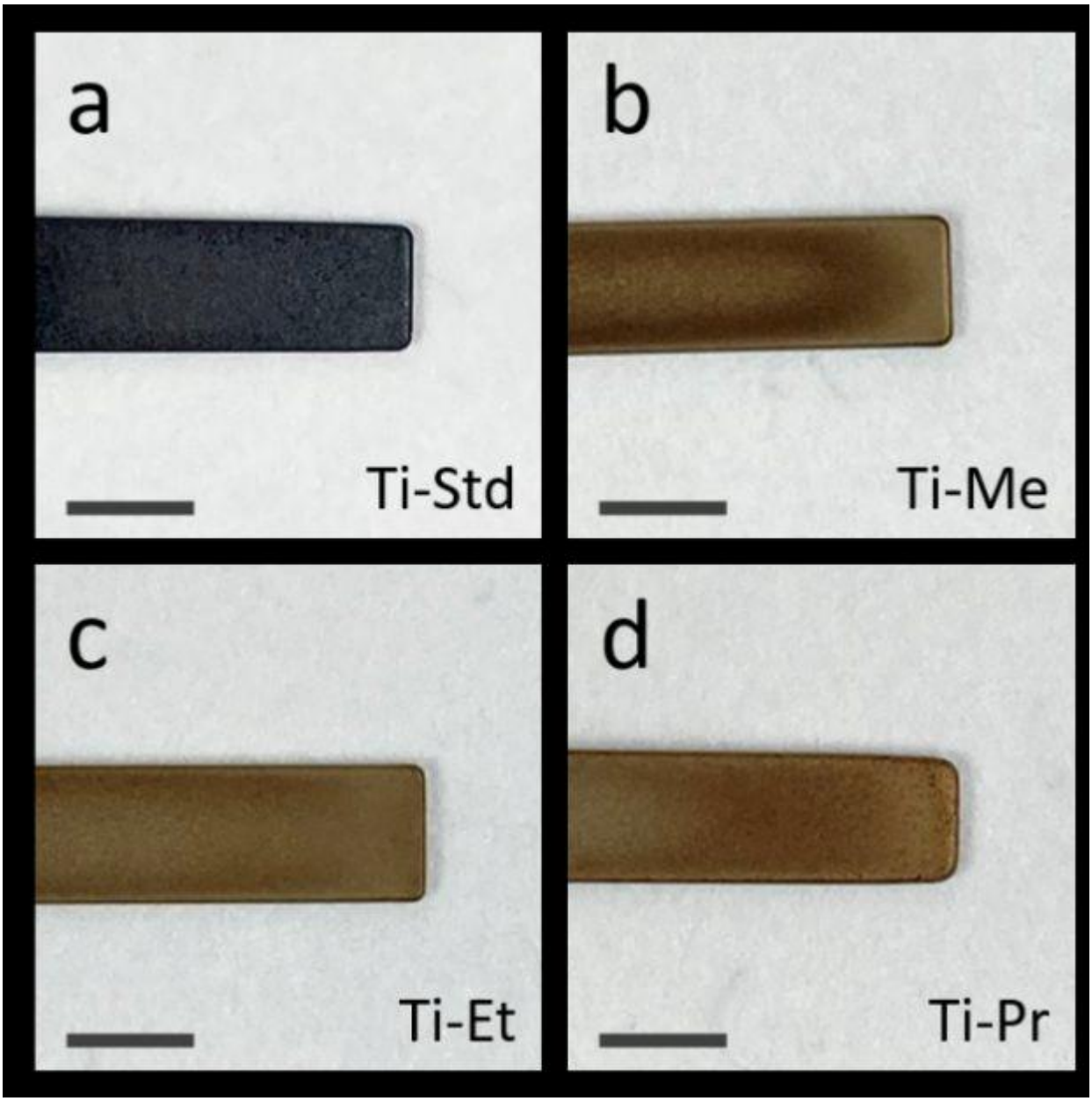

Figure 2.9. Optical images of Ti electrodes after SPP in different electrolytes (scale bar: 5 mm).

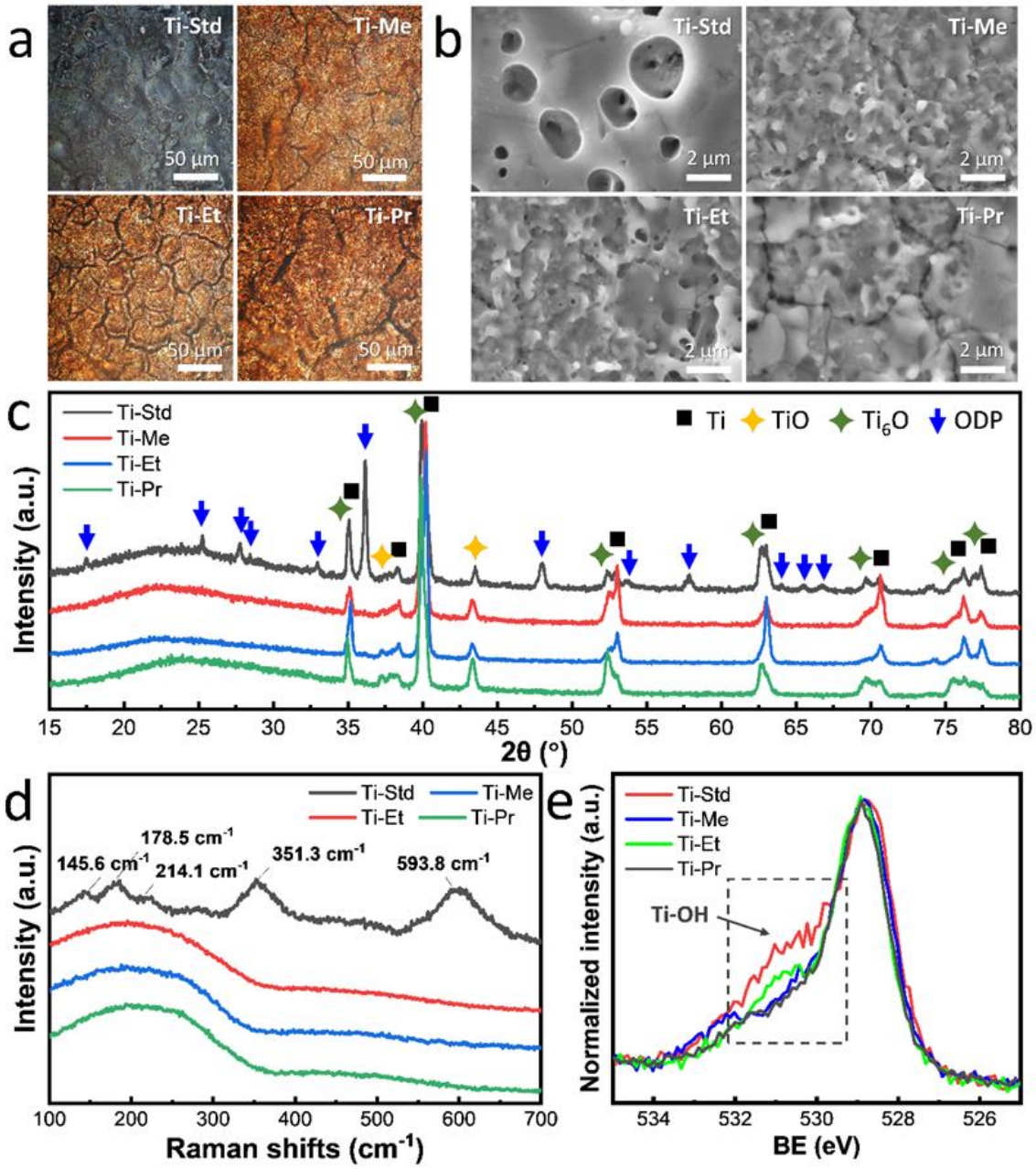

Figure 2.10. Surface characterization of Ti electrode after the SPP synthesis. (a) Optical images, (b) SEM images, (c) XRD patterns, (d) Raman spectrums, and (e) XPS O 1s spectrum of Ti electrodes processed in aqueous electrolyte (Ti-Std), water-methanol electrolyte (Ti-Me), water-ethanol electrolyte (Ti-Et) and water-1-propanol electrolyte (Ti-Pr).

The non-negligible phase differences between b-TiO_2 and black layer on the Ti electrode suggests that the formation of b-TiO_2 particles is not a simple disengagement process of molten species from the black layer. Since the role of ·H and ·OH are not properly emphasized in the

previous research, the mechanism is still ambiguous. One process is proposed by Zhang et al. [13], which uses 'melting-quenching' to clarify the mechanism of the formation of b-TiO_2 by SPP method. Because of the Joule heating by concentrated current flow, the local melting of Ti electrode happens with the rapid rising of plasma temperature, and then sputters molten Ti cluster species, which aggregates to form spherical particles in sequence. In another research, it is hypothesized that in the SPP fabrication of b-TiO_2, before being quenched, the sputtered molten Ti species are oxidized in plasma region and hydrogenated in or near plasma-liquid interface in the electrolyte [14]. According to the previous report, the excitation temperature calculated by the results of H_α and H_β lines in DC-excited discharge with Ti electrode can reach over 8000 K, which is much higher than the melting point of Ti and TiO_2 solid [28, 34]. Based on this temperature, the pre-oxidized surface of TiO_2 layer is melted and sputtered to form molten TiO_2 cluster species, then quenched by the electrolyte in sequence, thus forming the b-TiO_2 containing stable and metastable phases.

In addition, it is found that after being SPP treatment by KOH electrolyte (0.1 M) with an ethanol-water ratio of 1:10, the black surface on the Ti-Std sample can be removed and transformed to dark yellow color. Meanwhile, after centrifugation, black precipitates can be collected. The record of Ti electrode mass loss shows a rapid decrease in weight before the full removal of the black layer on the Ti electrode, while the dark yellow surface appears, the mass decreases much slower, as Figure 2.11 shows. Compared to typical SPP product, the obtained b-TiO_2 precipitates show the same properties. Although alcohols have been used as reducing agents for the noble metal s, like Ag, Au, and Pt [35, 36], the reduction potential of Ti is low, so that alcohols cannot reduce Ti oxides. This finding indicates that the disengagement of TiO_x species occurs as a separated step with a suppressed supply of ·H and ·OH radicals in the presence of alcohols.

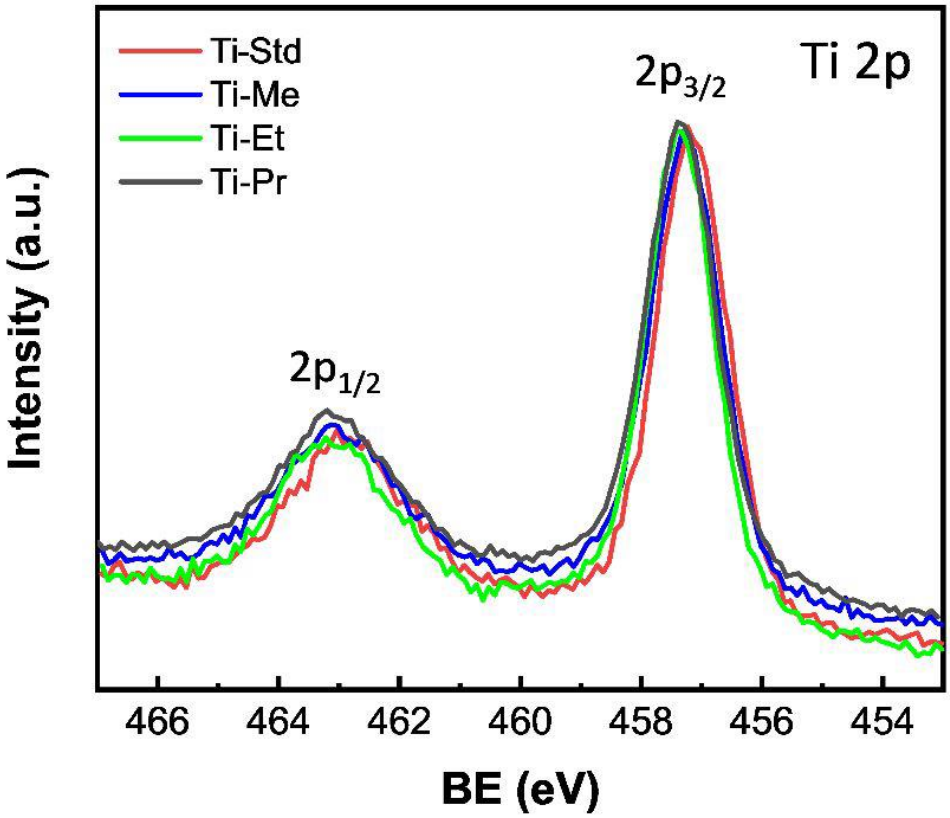

Figure 2.11. XPS Ti 2p spectra of Ti-Std, Ti-Me, Ti-Et, and Ti-Pr.

According to the above discussion, the formation of b-TiO_2 by SPP can be divided to two steps. In step 1, Ti cathode is bombarded by the dominated negative ions, such as O_2^- and OH^-, causing the damage of Ti surface, which exhibits as the increase of surface roughness. Meanwhile, with the effect of strong oxidant ·OH, TiO_2 surface with rich oxygen vacancies is formed on the Ti electrode [25]:

$$Ti \rightarrow TiO_{2-x} \tag{2.9}$$

During the SPP synthesis, hydrogen radical ·H can be produced by water splitting and decomposition of H_2 in plasma. As a strong reduction agent, ·H involves in many reduction reactions. In SPP synthesis, ·H fabricated in the plasma helps the hydrogen doping into the pre-oxidized TiO_{2-x} layer with oxygen vacancies, and forms black TiO_{2-x} layer in the plasma created by DC discharging [17]:

$$TiO_{2-x} + \cdot H \rightarrow H - TiO_{2-x} \tag{2.10}$$

Pre-oxidized TiO_2 is necessary for the formation of b-TiO_2, as reported by Yu et al. [17]. In step 2, the black TiO_{2-x} layer on the electrode melts by Joule heating from DC discharge, and the molten TiO_x are sputtered and quenched by electrolytes with lower temperature. The b-TiO_2 particles are formed by the aggregation of TiO_x clusters.

2.3.2 Basic Characterization of TiO_2 fabricated by EC-SPSC method

Figure 2.12 shows the SEM and XRD characterization of TiO_2 fabricated by EC-SPSC method. After the synthesis method, fine-grained oxides are formed on the surface of the Ti plate. Several cracks appear on the surface. According to the EDS mapping of O in Figure 2.12(b) and (c), the oxygen content of cracks is low, while Ti content is high, suggesting that these parts do not form Ti oxides. As shown in Figure 2.12(d), XRD patterns shows mainly Ti peaks instead of TiO_2 peaks. This result indicates that Ti substrate would affect the characterization results of TiO_2. Compared to the SEM of Ti cathode just after the plasma, EC-SPSC is workable for the fabrication of TiO_2. The elemental ratio of Ti/O is unpredictable, indicating that the repeatability of this method is bad. In addition, the TiO_2 product by EC-SPSC method is not homogeneous. These two problems hinder the further research.

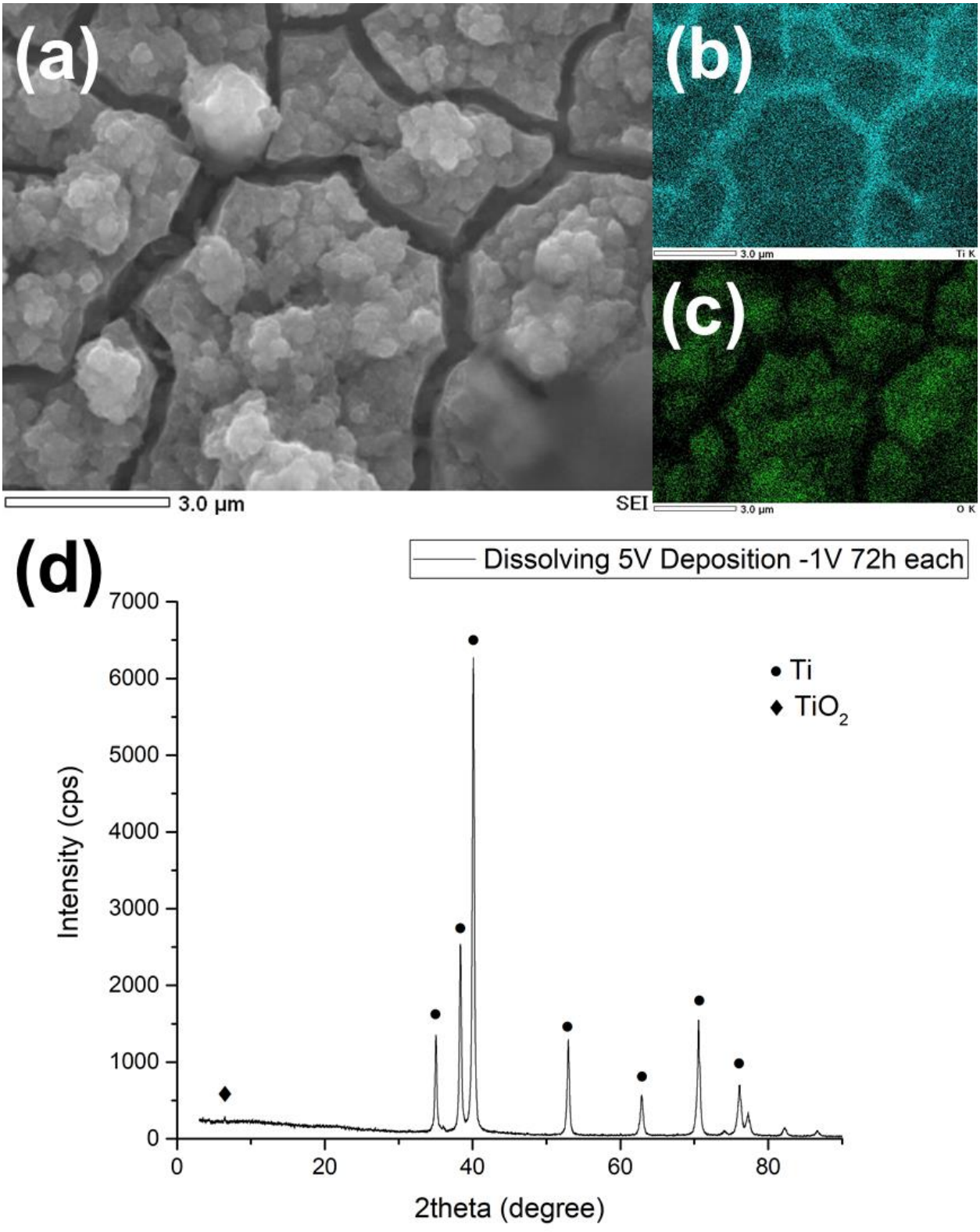

Figure 2.12. Basic characterization of EC-SPSC fabricated TiO_2.

2.4 Conclusion

In this work, we use a one-step SPP method to fabricate b-TiO_2, whose solar absorption property is superior. In addition, EC-SPSC method is used for the attempting of TiO_2 fabrication. A two-step mechanism for the formation of b-TiO_2 is proposed as follows:

(1) The formation of black TiO_{2-x} layer caused by the Ti electrode surface pre-oxidation.

(2) The electrode surface melted by Joule heating in plasma, then sputtered molten TiO_x clusters quenched by electrolyte and aggregated to form b-TiO_2 particles.

In these steps, the pre-oxidized TiO_{2-x} layer is found to be necessary for the b-TiO_2 formation by SPP method. The b-TiO_2 is proved to be effective on the generation of water vapor under solar light irradiation [37]. As a result, it is easily upscaled and used in clean, facile production of solar harvesting materials.

As for TiO_2 fabrication by EC-SPSC method, although it has been proved that TiO_2 can be fabricated by this method, the low-repeatability and bad-homogeneity prevent the further research. As a result, we do not recommend using the EC-SPSC method for the fabrication of TiO_2 nanoparticles.

References

1. Zhang, J., et al., *Development of modified N doped TiO_2 photocatalyst with metals, nonmetals and metal oxides.* Energy & Environmental Science, 2010. **3**(6): p. 715-726.

2. Asahi, R., et al., *Nitrogen-Doped Titanium Dioxide as Visible-Light-Sensitive Photocatalyst: Designs, Developments, and Prospects.* Chemical Reviews, 2014. **114**(19): p. 9824-9852.

3. Chen, X. and S.S. Mao, *Titanium Dioxide Nanomaterials: Synthesis, Properties, Modifications, and Applications.* Chemical Reviews, 2007. **107**(7): p. 2891-2959.

4. Liu, L. and X. Chen, *Titanium Dioxide Nanomaterials: Self-Structural Modifications.* Chemical Reviews, 2014. **114**(19): p. 9890-9918.

5. Chen, X., et al., *Increasing Solar Absorption for Photocatalysis with Black Hydrogenated Titanium Dioxide Nanocrystals.* Science, 2011. **331**(6018): p. 746-750.

6. Chen, X., L. Liu, and F. Huang, *Black titanium dioxide (TiO_2) nanomaterials.* Chemical Society Reviews, 2015. **44**(7): p. 1861-1885.

7. Saito, G., et al., *Solution plasma synthesis of bimetallic nanoparticles.* Nanotechnology, 2014. **25**(13): p. 135603.

8. Saito, G. and T. Akiyama, *Nanomaterial Synthesis Using Plasma Generation in Liquid.* Journal of Nanomaterials, 2015. **2015**: p. 123696.

9. Hu, X., et al., *Facile fabrication of PtAu alloy clusters using solution plasma sputtering and their electrocatalytic activity.* Journal of Alloys and Compounds, 2013. **552**: p. 351-355.

10. Hu, X., et al., *Rapid Synthesis and Structural Characterization of Well-Defined Gold Clusters by Solution Plasma Sputtering.* Crystal Growth & Design, 2012. **12**(1): p. 119-123.

11. Ishida, Y., et al., *Small Nanosized Oxygen-Deficient Tungsten Oxide Particles: Mechanistic Investigation with Controlled Plasma Generation in Water for Their Preparation.* ACS Omega, 2017. **2**(8): p. 5104-5110.

12. Toriyabe, Y., et al., *Controlled formation of metallic nanoballs during plasma electrolysis.* Applied Physics Letters, 2007. **91**(4): p. 041501.

13. Zhang, Z.-K., et al., *Plasma-electrolysis synthesis of TiO_2 nano/microspheres with optical absorption extended into the infra-red region.* Chemical Communications, 2011. **47**(29): p. 8439-8441.

14. Panomsuwan, G., et al., *Water-plasma-assisted synthesis of black titania spheres with efficient visible-light photocatalytic activity.* Physical Chemistry Chemical Physics, 2015. **17**(21): p. 13794-13799.
15. Jedsukontorn, T., et al., *Facile preparation of defective black TiO_2 through the solution plasma process: Effect of parametric changes for plasma discharge on its structural and optical properties.* Journal of Alloys and Compounds, 2017. **726**: p. 567-577.
16. Jedsukontorn, T., et al., *Narrowing band gap energy of defective black TiO_2 fabricated by solution plasma process and its photocatalytic activity on glycerol transformation.* Journal of Alloys and Compounds, 2018. **757**: p. 188-199.
17. Yu, F., et al., *Enhanced Solar Photothermal Catalysis over Solution Plasma Activated TiO_2.* Advanced Science, 2020. **7**(16): p. 2000204.
18. Jeem, M., et al., *A pathway of nanocrystallite fabrication by photo-assisted growth in pure water.* Scientific Reports, 2015. **5**(1): p. 11429.
19. Jeem, M., et al., *Tuning Optoelectrical Properties of ZnO Nanorods with Excitonic Defects via Submerged Illumination.* Nano Letters, 2017. **17**(3): p. 2088-2093.
20. Zhang, L., et al., *Photochemistry and the role of light during the submerged photosynthesis of zinc oxide nanorods.* Scientific Reports, 2018. **8**(1): p. 177.
21. Zhang, L., et al., *Fabrication of Iron Oxide Nanoparticles via Submerged Photosynthesis and the Morphologies under Different Light Sources.* ISIJ International, 2019. **59**(12): p. 2352-2358.
22. Nishino, F., et al., *Formation of CuO nano-flowered surfaces via submerged photo-synthesis of crystallites and their antimicrobial activity.* Scientific Reports, 2017. **7**(1): p. 1063.
23. Makuła, P., M. Pacia, and W. Macyk, *How To Correctly Determine the Band Gap Energy of Modified Semiconductor Photocatalysts Based on UV–Vis Spectra.* The Journal of Physical Chemistry Letters, 2018. **9**(23): p. 6814-6817.
24. Banno, M., et al., *Nanosecond time-resolved microscopic spectroscopy for diagnostics of an atmospheric-pressure discharge plasma formed in aqueous solution.* Japanese Journal of Applied Physics, 2015. **54**(6): p. 066101.
25. Chen, Q., et al., *Potential structure of discharge plasma inside liquid directly measured by an electrostatic probe.* Applied Physics Letters, 2013. **102**(24): p. 244105.
26. Zhang, H., et al., *Low-Temperature Atomic Hydrogen Treatment of SiO_2/Si Structures.* Japanese Journal of Applied Physics, 2003. **42**(Part 1, No. 10): p. 6252-6255.

27. Sudare, T., et al., *Accelerated nanoparticles synthesis in alcohol–water-mixture-based solution plasma.* Physical Chemistry Chemical Physics, 2015. **17**(45): p. 30255-30259.
28. Saito, G., Y. Nakasugi, and T. Akiyama, *Excitation temperature of a solution plasma during nanoparticle synthesis.* Journal of Applied Physics, 2014. **116**(8): p. 083301.
29. Yamaguchi, S., M. Koiwa, and M. Hirabayashi, *Interstitial Superlattice of Ti_6O and Its Transformation.* Journal of the Physical Society of Japan, 1966. **21**(10): p. 2096-2096.
30. Pabón, B.M., et al., *Formation of titanium monoxide (001) single-crystalline thin film induced by ion bombardment of titanium dioxide (110).* Nature Communications, 2015. **6**(1): p. 6147.
31. Shu, G., et al., *Microwave-Assisted Synthesis of Black Titanium Monoxide for Synergistic Tumor Phototherapy.* ACS Applied Materials & Interfaces, 2019. **11**(3): p. 3323-3333.
32. Shuker, R. and R.W. Gammon, *Raman-Scattering Selection-Rule Breaking and the Density of States in Amorphous Materials.* Physical Review Letters, 1970. **25**(4): p. 222-225.
33. Zimbone, M., et al., *Black TiO_x photocatalyst obtained by laser irradiation in water.* Catalysis Communications, 2016. **84**: p. 11-15.
34. Hazrati, H.D., J.D. Whittle, and K. Vasilev, *A Mechanistic Study of the Plasma Polymerization of Ethanol.* Plasma Processes and Polymers, 2014. **11**(2): p. 149-157.
35. Teranishi, T. and M. Miyake, *Size Control of Palladium Nanoparticles and Their Crystal Structures.* Chemistry of Materials, 1998. **10**(2): p. 594-600.
36. Gomes, J.F., et al., *New insights into the formation mechanism of Ag, Au and AgAu nanoparticles in aqueous alkaline media: alkoxides from alcohols, aldehydes and ketones as universal reducing agents.* Physical Chemistry Chemical Physics, 2015. **17**(33): p. 21683-21693.
37. Zhu, S., et al., *Solution Plasma-Synthesized Black TiO_2 Nanoparticles for Solar–Thermal Water Evaporation.* ACS Applied Nano Materials, 2021. **4**(4): p. 3940-3948.

Chapter 3

Mesoporous Single Crystal Titanium Oxide Microparticles for Enhanced Visible Light Photodegradation

3.1 General Introduction

Titanium dioxide (TiO_2) has played a very important role in the photodegradation of dyes due to its unique properties, such as better stability, non-toxicity, and better photocatalytic performance due to its bandgap (~ 3 eV) [1]. Commercially available TiO_2 products, for example, P25-TiO_2 (hereinafter called P25), a well-known material which is the composite of rutile and anatase, have been widely used in the field of photocatalytic degradation of organic pollutants [2-4]. In spite of high photoactivity of P25 under ultraviolet condition, its efficiency is limited under visible light irradiation [5].

On this account, researchers have been working on the improvement of the photodegradation efficiency of TiO_2 materials under visible light. For example, impurity doping is an effective way to extend usable light wavelength range of titanium dioxide [6-9]. Park et al. [6] used graft polymerization method to fabricate N-doped TiO_2, which has enhanced methyl orange degradation activity under visible light. Choi et al. [7] doped metal ion into TiO_2 to increase its visible light photoactivity. Introducing defects can also help to improve visible light activity. Dong et al. [8] successfully synthesized black TiO_2 through facile anodization technique, with a high photocatalytic activity under visible light. In addition to the methods above, pores and high specific surface area would contribute to the higher performance of TiO_2. Naik et al. [9] fabricated super porous TiO_2 photocatalyst (with over 100 m^2/g specific surface area) by sol-gel method and shows better adsorption and photodegradation ability of amaranth dyes.

Compared to the above methods, lattice defect introduction can not only take the advantage of doping effects, but also avoid introducing impurities [10-14]. Zhu et al. [10] used solution plasma synthesis method to fabricate black TiO_2 with Ti (III) component and prove its high activity for solar-thermal water evaporation. Xin et al. [11] successfully introduced Ti (III) into TiO_2 with significantly improved performance. Xu et al. [12] also fabricated TiO_2 microspheres with Ti (III) defects and proves the higher photodegradation efficiency, almost three times under visible light irradiation. In addition, single crystal has unique optical application, which makes TiO_2 work better under visible light. Zheng et al. [13] successfully fabricated mesoporous single crystal TiO_2

by using silica-templated hydrothermal method which works well for the photodegradation of methyl orange. Cheng et al. [14] also used $KTiOPO_4$ to fabricate single crystal TiO_2, which enhanced photoelectrochemical performance and shows a high conversion for benzene to phenol. In addition to the methods above, Ti metal can also be used for fabrication. Generally, H_2O_2 will play an important role in the direct oxidation of Ti metal, while several additives (e.g., HF, NaF or NaCl) will be used to control the product [15, 16]. The direct oxidation of Ti metal by H_2O_2 solution can also avoid impurity-introducing and create Ti (III).

Herein, we developed a facile one-step method to fabricate mesoporous single-crystalline ellipsoidal TiO_2 microparticles (e-TiO_2 MPs), which only requires common materials of Ti, an additive of NH_4F with hydrogen peroxide, and a simple process at elevated temperature. Additionally, the product is mesoporous structure with both Ti (III) and Ti (IV) components, which can make it have unique properties. The photocatalytic degradation of Rhodamine B and Methylene blue solution were conducted under visible light condition to compare the photocatalytic performance of the as-synthesized e-TiO_2 MPs with commercial P25. The possible mechanisms of the photocatalytic performance enhancement from the view of microstructure and their optical properties are also discussed.

3.2 Experimental section

3.2.1 Synthesis of e-TiO_2 MPs

The e-TiO_2 MPs were fabricated by a one-step method. The titanium plates (Nilaco Cooperation, Japan) were cut into the standard pieces (3.75 mm × 20 mm × 0.2 mm), and cleaned in acetone, ethanol, and distilled water under ultrasonication. Ti plates were then placed in a polymethyl methacrylate (PMMA) cuvette (3 ml) contained with 2 mL of hydrogen peroxide solution (30 wt%, H_2O_2, Kanto Chemical Co., inc.). 15 mg of NH_4F (97%, Wako Pure Chemical Cooperation, Wako special grade) was then added into the cuvette. The reaction was controlled at 80°C for 72 h. The precipitates were collected by centrifugation and cleaned with ethanol three times, then dried for 24 h at 50°C.

3.2.2 Structural characterizations

The as-synthesized e-TiO_2 MPs were observed using a transmission electron microscope (TEM, JEOL JEM-2000FX) operated at 200 kV and a field emission scanning electron microscope (FESEM, JEOL JSM-7001F) operated at 15 kV. High-resolution transmission electron microscopy

(HRTEM) images were taken using a scanning transmission electron microscopy (FEI Titan G3 60-300) operated at 300 kV. X-ray diffraction (XRD) measurement were conducted using an X-ray diffractometer (RIGAKU Miniflex 600) with the Cu Kα radiation as the source. UV-vis-NIR absorption spectra were measured using a UV-vis-NIR spectrometer (JASCO V-770 spectrophotometer). The band gap information was obtained by the Tauc's plot from the spectra. A photoelectron spectrometer with monochromatic Mg Kα radiation was used for X-ray photoelectron spectroscopy (XPS, JEOL JPS-9200). Brunauer–Emmett–Teller (BET) analysis was carried out using a sorption analyzer (Autosorb 6AG, Yuasa Ionics) to measure the specific surface area and the pore size distribution. P25 (particle sizes of 15-40 nm, Evonik Aeroxide) was tested as the control group.

3.2.3 Photodegradation experiments

Rhodamine B (RhB, 10^{-5} M, $C_{28}H_{31}ClN_2O_3$, Wako Pure Chemical Cooperation) and Methylene blue (MB, 10^{-5} M, $C_{16}H_{18}N_3SCl{\cdot}3H_2O$, Wako Pure Chemical Cooperation) were chosen as the typical dye for the photodegradation experiment of e-TiO_2. The commercially available P25 was set as the control group. For all experiments, 20 mg of the photocatalyst was added into 50 mL of the dye solution. A visible light source (Hamamatsu Lightningcure LC8, with a band filter of 400-600 nm, 300 VA) was used for illumination. Before the photodegradation, all the photocatalyst samples were stirred (~ 300 rpm) in dye solution for 30 min in dark to make good suspension and to exclude the effects of dye adsorption. All photodegradation experiments were set for 1 h, and a 2-ml aliquot was taken every 10 minutes for UV-vis-NIR spectra testing of the supernatant.

3.3 Results and discussion

3.3.1 Structural characterizations

Figure 3.1(a) shows the SEM images of the as-synthesized e-TiO_2 MPs, whose color is light yellow. The size distribution of e-TiO_2 based on the Figure 3.1(a) is shown in Figure 3.1(b). The particles with ellipsoidal shape were selected for the particle size distribution statistics. As shown in Figure 3.1(b), the polar diameter of the e-TiO_2 particles is in the range of 305 ± 56 nm. It is obvious that e-TiO_2 MPs have much larger size than P25 (~ 20 nm), which is shown in supplementary Figure 3.2(a). Furthermore, Figure 3.2(b) shows the titanium plate surface after the synthesis. After the reaction, the titanium plate surface was homogeneously covered by e-TiO_2

MPs. These MPs remain on the surface even after ultrasonic cleaning, showing a strong connection to the titanium plate. This result suggests that e-TiO_2 MPs were first generated on the surface of titanium plate, and then separated into the solution. The supersaturated Ti^{4+} ions could also be a Ti source for e-TiO_2 sediment in the solution. In addition, the EDS analysis results show the same Ti: O atomic ratios (1: 1.7) of both e-TiO_2 MPs in the solution and on the titanium plate surface.

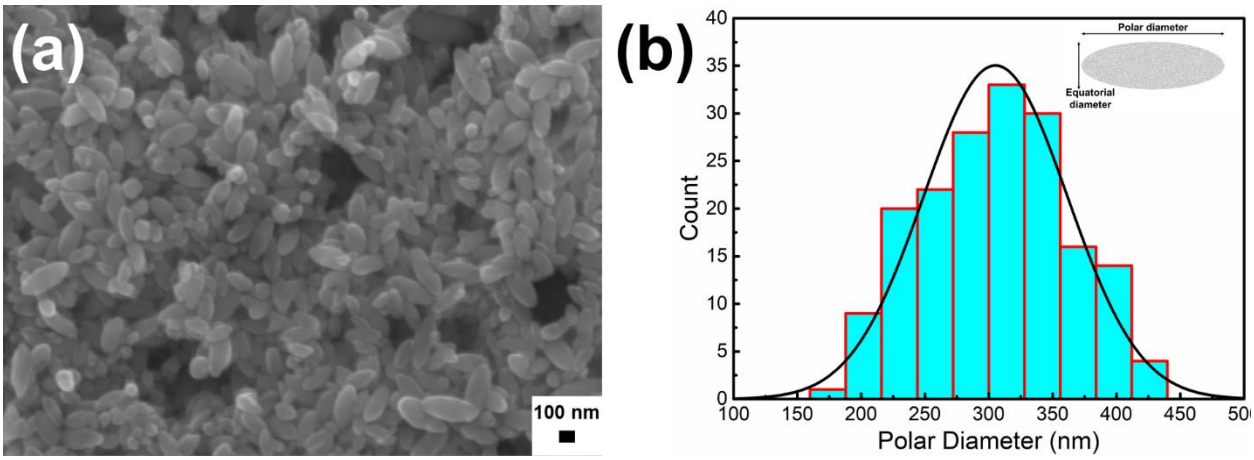

Figure 3.1. (a) SEM image of e-TiO_2, (b) size distribution figure from (a).

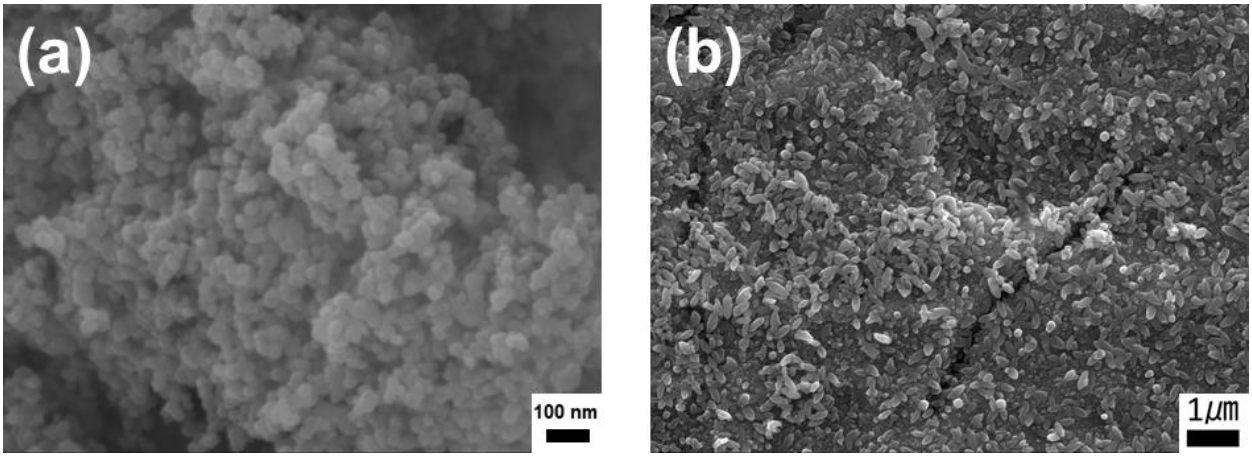

Figure 3.2. SEM image of (a) P25 and (b) Ti plate after fabrication.

The results of XRD patterns for the e-TiO_2 and P25 are compared in Figure 3.3. The diffraction peaks for e-TiO_2 are only attributed to the anatase phase. The typical peaks located at 25° and 37° correspond to the (101) and (103) planes of anatase phase. While the commercial P25 have an anatase-rutile binary phase structure. P25 shows both rutile peaks (27°, 41°, 54° for the planes (110), (111) and (211)) and anatase peaks (25° for (101) and 37° for (103), similar to e-TiO_2). Most of the time, if controlling the product as anatase, special methods are required for the selective production, such as using the sol-gel method by 3.3% molar concentration of glacial

acetic acid [17], or separating rutile/anatase/brookite complex by using 3 mol/L HNO_3 solution [18]. Compared to these methods, our synthesis of e-TiO_2 doesn't require other methods to control the product, simplifying the experimental steps, and making the product not interfered by impurities.

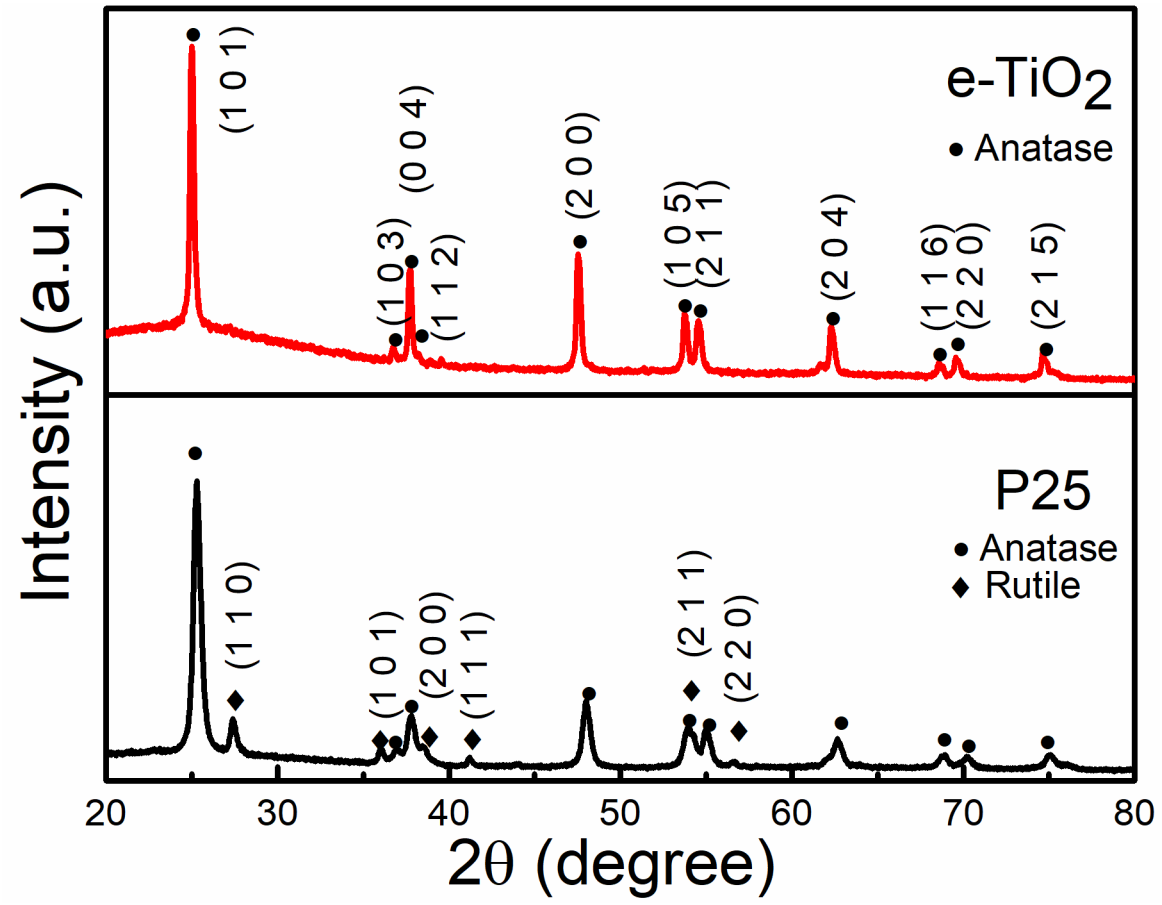

Figure 3.3. The XRD patterns of e-TiO_2 and P25. (Top: e-TiO_2, bottom: P25).

To analyze the surface of e-TiO_2 in detail, XPS analysis was carried out. Figure 3.4(a) shows the XPS analysis results of Ti for both e-TiO_2 and P25. According to the XPS database (NIST Standard Reference Database 20, Version 4.1 [19]), the XPS spectra of Ti range (455-467 eV) for e-TiO_2 can be fitted to 3 peaks. The peak located at 458 eV is recognized as typical TiO_2 Ti 2p3/2 peak. There is another TiO_2 peak at around 462 eV, which refers to the TiO_2 Ti 2p1/2 peak. In addition to the above two peaks, the peak located at 460 eV represents the existence of Ti (III). For P25, only typical TiO_2 Ti 2p1/2 (463 eV) and Ti 2p3/2 (458 eV) peaks are shown in the spectra. The binding energy of TiO_2 Ti 2p1/2 for e-TiO_2 and P25 are not same, suggesting that the surface elemental makeup of e-TiO_2 and P25 are different. The XPS spectra of oxygen also contains the information of low valence Ti. According to the database [19], the typical TiO_2 oxygen peak is

located at 529 eV. For e-TiO_2, there are two different peaks shown in the spectra. The peak at 531 eV indicates the Ti-O-H bond, and the peak which located at 533 eV is the peak of TiO_{2-x} [19-21]. Furthermore, two peaks at around 690 eV prove the existence of fluoride, which is shown in Figure 3.5. The peak located at 684 eV represents the F 1s peak of F^- [22], while the peak at 687 eV represents the F 1s peak of $TiO_{2-x}F_x$. [16]. Generally, to introduce Ti (III) in TiO_2, TiO_2 should be fabricated first, and then reduced by using other methods, which may require high temperature or other materials, for example, by using hydrogen reduction method under higher temperature (573 K) [23], or by introducing Ti-O-Fe structure formed by ferric nitrate ($Fe(NO_3)_3 \cdot 9H_2O$) [20] However, the present synthesis of e-TiO_2 and does not require high temperature or introduce other metal atoms, making this fabrication method more convenient.

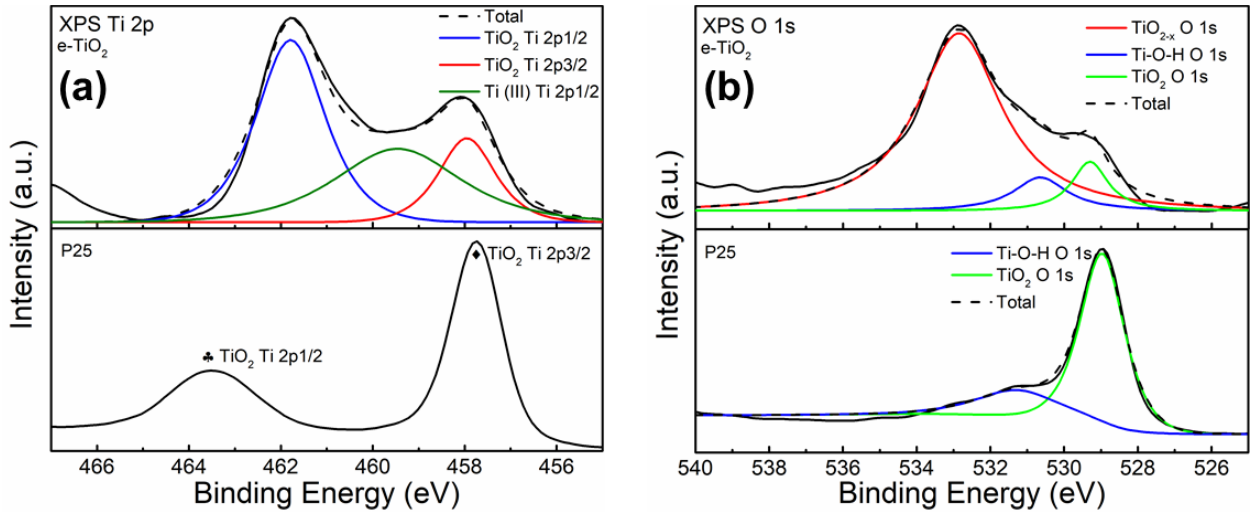

Figure 3.4. (a) XPS data of e-TiO_2 and P25 in Ti 2p binding energy range (Top: e-TiO_2, bottom: P25); (b) XPS data of e-TiO_2 and P25 in O 1s binding energy range. (Top: e-TiO_2, bottom: P25).

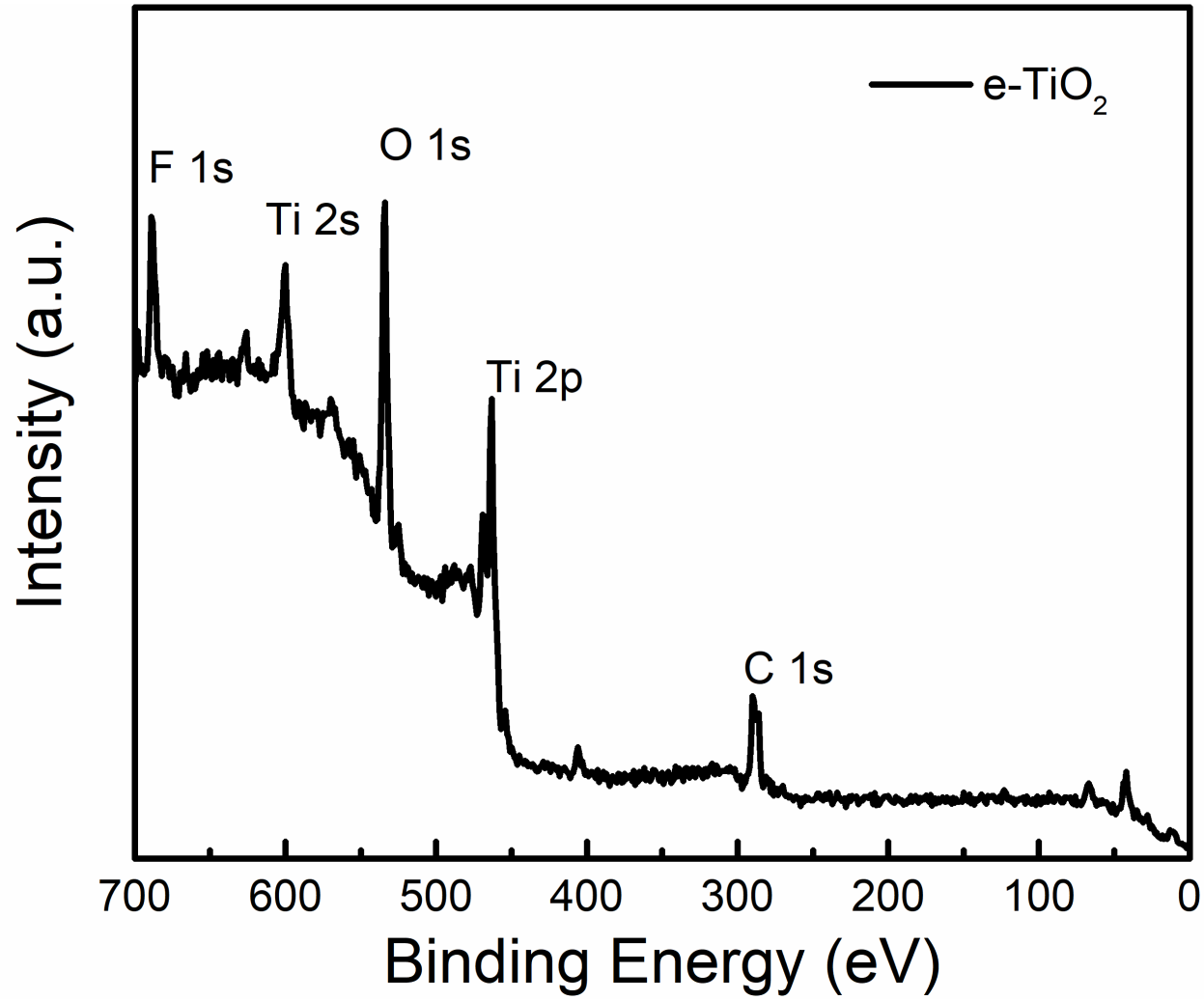

Figure 3.5. XPS wide scan spectra of e-TiO_2.

In order to figure out the specific surface area and pores, Brunauer–Emmett–Teller (BET) method is used for the pore size distribution analysis of e-TiO_2. Figure 3.6(a) shows the BET adsorption and desorption curve of e-TiO_2, which displays a type IV isotherm with hysteresis loop located at relative pressures of P/P_0 = 0.40-0.90. [24, 25]. This type IV isotherm with hysteresis loop is caused by capillary condensation initiated by mesopores [26]. For e-TiO_2, the BET surfaces area is calculated as 26 m^2/g. To prove that e-TiO_2 MPs are porous by BET specific surface area, we calculate the specific surface area of one perfect prolate spheroid (equatorial radius equals to each other) with the same size as e-TiO_2, and then compare with each other. According to the particle sized distribution in Figure 3.1(b), we assume the equatorial radius of e-TiO_2 is 50 nm, and the polar radius is 150 nm. Figure 3.7 shows the simulated perfect prolate spheroids, and the surface area of perfect prolate spheroids is calculated by the following equation:

$$S_p = 2\pi a^2 \left(1 + \frac{c}{ae}\arcsin e\right) \tag{3.1}$$

where a is the equatorial radius, c is the polar radius. e is the ellipticity of the prolate spheroid, defined by

$$e \equiv \sqrt{\frac{c^2 - a^2}{c^2}} = \sqrt{1 - \frac{a^2}{c^2}} \tag{3.2}$$

For a perfect prolate spheroid, we assume the equatorial radius a of e-TiO_2 is 50 nm, and the polar radius c is 150 nm (according to the particle size distribution), the average surface area is calculated as 7.723×10^4 nm^2.

Also, the volume of ellipsoid is calculated as:

$$V = \frac{4\pi a^2 c}{3} \tag{3.3}$$

For prolate spheroid, the volume of an e-TiO_2 particle is 1.571×10^6 nm^3. Since the density of anatase is 3.8 g/cm^3, the specific surface area of one perfect ellipsoid anatase should be 13.39 m^2/g.

Compared to the BET specific surface area, e-TiO_2 has much higher specific surface area than the perfect particle with same size, which suggests the porous structure of e-TiO_2.

In addition, as shown in Figure 3.6(b), Barrett-Joyner-Halenda (BJH) method is used to determine the pore size distribution. Most pores are distributed in the mesoporous interval (2-50 nm). The pore size inside e-TiO_2 is concentrated around 2 nm and remains high concentration within 5 nm range.

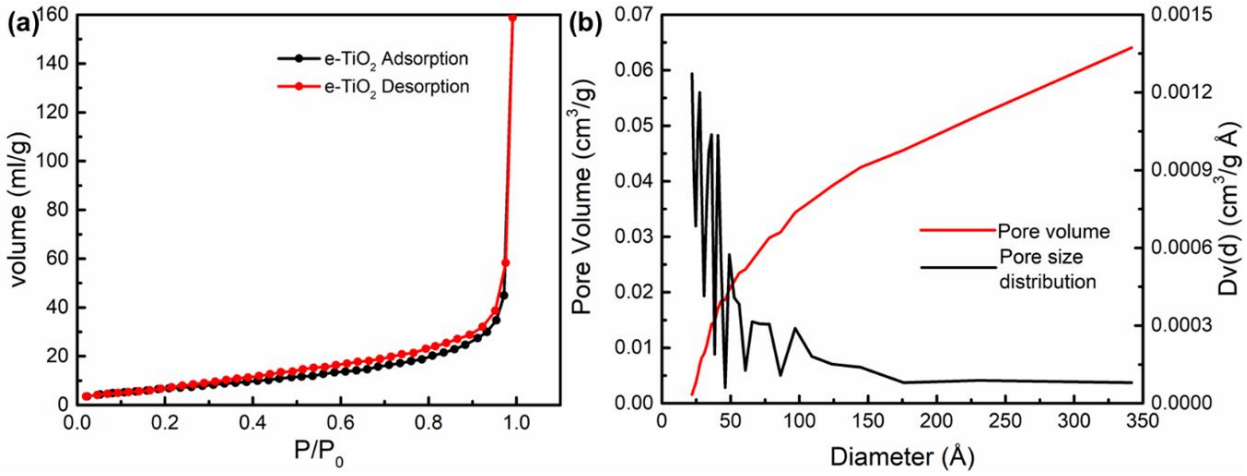

Figure 3.6. (a) BET adsorption and desorption curve of e-TiO_2; (b) BJH pore volume and pore size distribution curves of e-TiO_2.

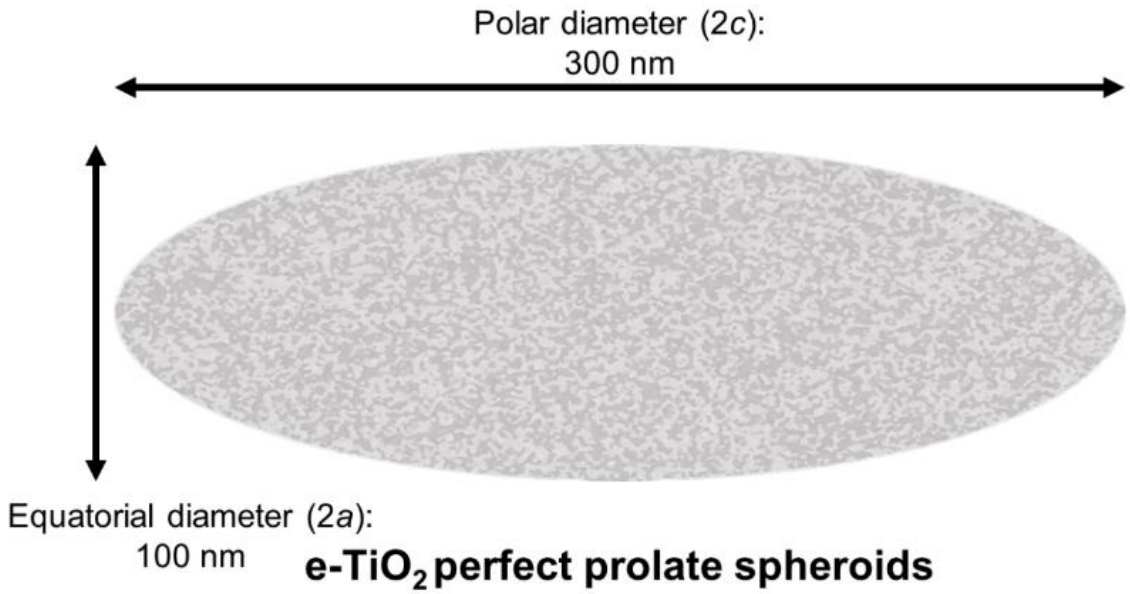

Figure 3.7. e-TiO_2 perfect prolate spheroids.

TEM images of e-TiO_2 in Figure 3.8(a) shows a clear ellipsoidal shape for e-TiO_2, whose aspect ratio is 14:5. As shown in Figure 3.8(b), the electron diffraction pattern of a single e-TiO_2 particle indicates that the whole e-TiO_2 particle is a single crystal with uniform orientation. Both (101) and (103) planes noted on this diffraction pattern are consistent with the XRD results of anatase. The results of diffraction pattern also suggest that e-TiO_2 growth towards (103) direction. Figure 3.8(c) and Figure 3.8(d) show the underfocus and overfocus TEM images, respectively, for the same area of an e-TiO_2 particle. In the highlighted area of underfocus TEM image, several lighter spots can be seen, while in the same area of overfocus TEM image, the lighter spots become darken. These contrast difference between the two different-defocused pictures suggests the existence of nano-pores. In our one-step method, NH_4F is considered to play a very important role [27] in the formation of bumpy surfaces and pores by the generation of coordination ion $[TiF_6]^{2-}$. Uneven surfaces of e-TiO_2 shows that F^- ions have successfully corroded TiO_2 surface and introduced pores.

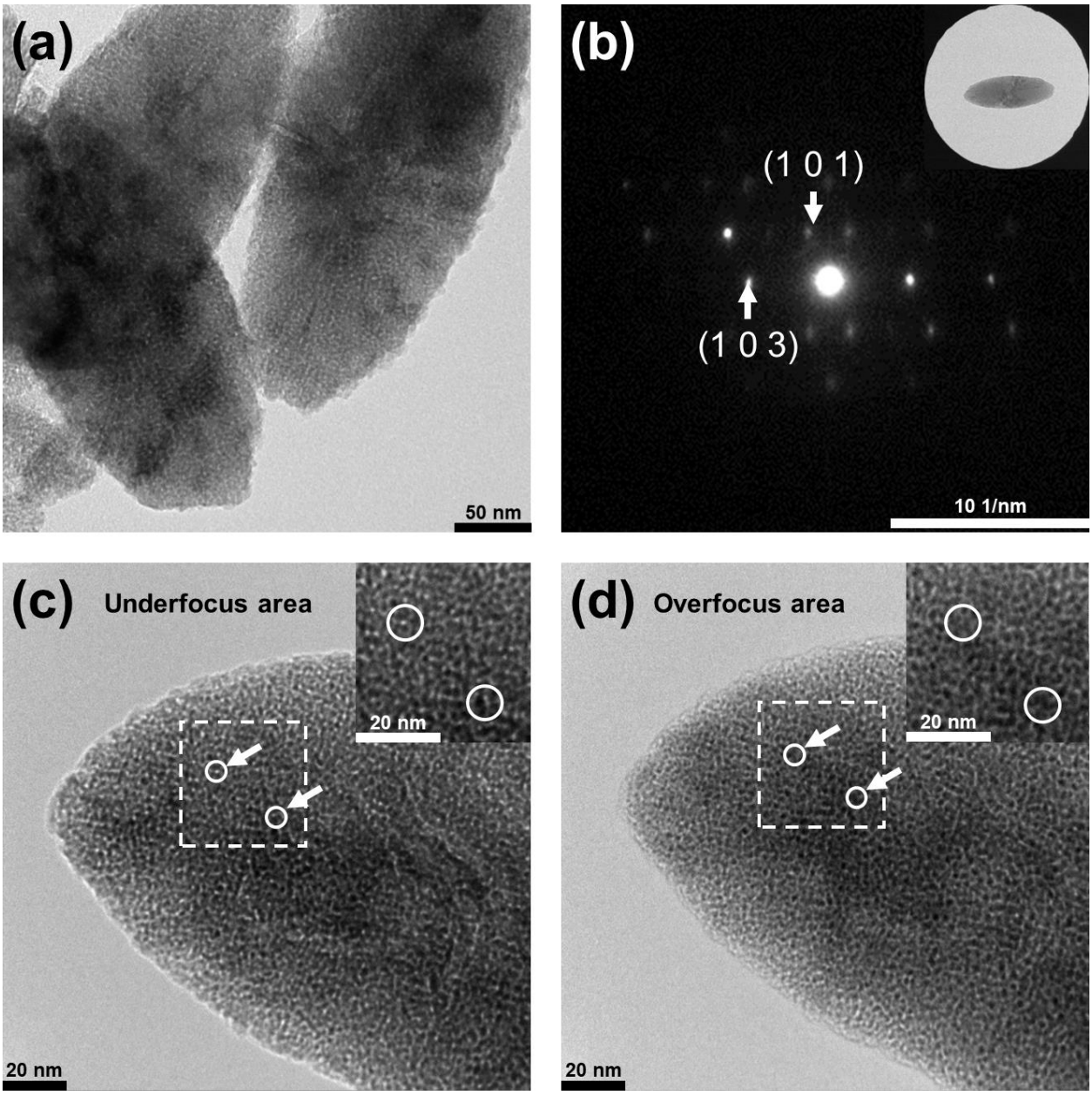

Figure 3.8. (a) TEM image of e-TiO_2; (b) diffraction pattern of e-TiO_2 single crystal, with (101) and (103) plane pointed out; (c) underfocus image of e-TiO_2 (d) overfocus image of e-TiO_2.

To examine the e-TiO_2 MPs more specifically, scanning transmission electron microscopy (STEM) is used for precision analysis. In the high-resolution TEM image of Figure 3.9(a), for an e-TiO_2, there are several blurred areas which are observed. Based on the previous TEM analysis, these blurred areas are presumably nano pores with defects. In order to confirm this, Fast Fourier Transform (FFT) and Inverse Fast Fourier Transform (IFFT) methods are used for the characterization [28]. Figure 3.9(c) shows the FFT image of selected area in Figure 3.9(b). The

FFT diffractogram is very similar to the diffraction pattern of e-TiO_2, also showing a regular arrangement, suggesting the fact that e-TiO_2 is a single crystal. Figure 3.9(d) of the IFFT image masked by the spot pair (plane (103)) in Figure 3.9(c) depicts several lattice discrepancies could be seen with some alone, and others in pair. These dislocations or related lattice defects suggest that there exist mesopores in the e-TiO_2 particle, as we discussed above, which are presumably generated by the movement of oxygen vacancies created by F^- ions in the e-TiO_2 particles [29].

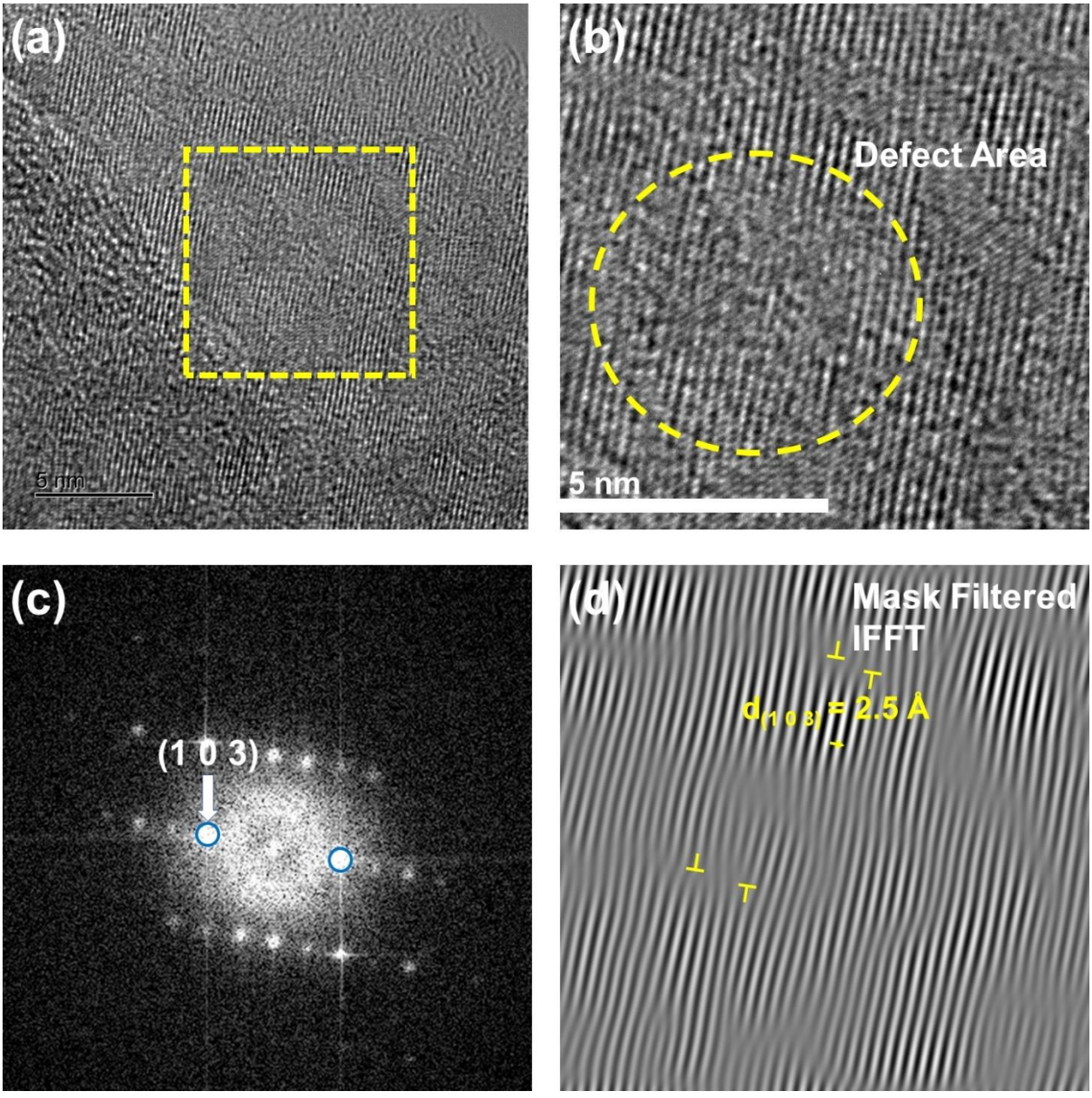

Figure 3.9. (a) High resolution TEM image of e-TiO_2; (b) Enlarged image of highlighted area in (a); (c) Fast Fourier Transform of (b); (d) Inverse Fast Fourier Transform of (c) selected (103) spot pair.

Figure 3.10 shows the electron energy loss spectroscopy (EELS) results. Two ranges of energy loss have been chosen, including low loss part (a) and core loss Ti part (b). Log-Ratio method is used to calculate the thickness of sample particles based on the data of zero and low loss part EELS [30]:

$$t/\lambda = \ln(I_t/I_0) \tag{3.4}$$

where t is the thickness of sample, λ is the inelastic mean free path of electron, I_t is the total integrated intensity of all EELS spectrum, I_0 means the total integrated intensity of zero loss peak (ZLP). For inorganic compound, Seah and Dench [31] proposed the following empirical formula to calculate its inelastic mean free path:

$$\lambda = 2170aE^{-2} + 0.72a^{3/2}E^{\frac{1}{2}} \tag{3.5}$$

where a is the average single layer thickness for the selected material, and E is the electron energy. For e-TiO_2 MPs, we can assume that a is 0.35 nm (interplanar spacing of layer (101)), and the thicknesses of two different positions are calculated by the data in Figure 3.10(a) and shown in Table 3.1. The calculated thickness of two positions is approximately 48 nm, while the measured thickness is 80-90 nm. Therefore, the estimation results of sample thickness by EELS data suggest the existence of pores in the e-TiO_2 MPs.

Table 3.1. Low loss EELS related data.

	I_0	I_t	$\ln(I_t/I_0)$	λ (nm)	t (nm)
Position 1	2.13×10^6	3.65×10^6	0.5391	89.64	48.32
Position 2	2.32×10^6	3.98×10^6	0.5386	89.64	48.28

Figure 3.10(b) shows the core loss EELS of e-TiO_2 MPs, for both Ti core loss range (450-470 eV) and O core loss range (520-540 eV). For position 1 (black line), there are two single peaks located in Ti core loss range, and one peak in O core loss range. According to Huang's research [32], two single peaks in Ti core loss range and one peak in O core loss range refer to the Ti (III) component. Position 2 (red line) shows two double peaks in Ti range and two peaks in O range, which refer to the TiO_2 component [32]. The EELS results are consistent with the XPS results, which proves the existence of Ti (III) in e-TiO_2.

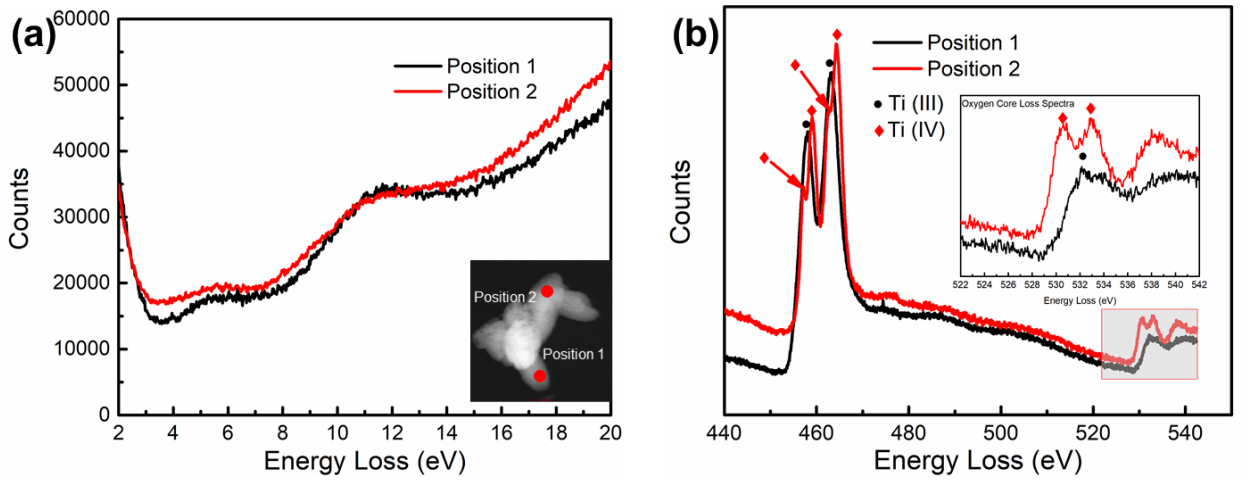

Figure 3.10. (a) EELS low loss spectra of e-TiO_2; (b) EELS Ti and O core loss spectra of e-TiO_2.

3.3.2 The reaction mechanism for the fabrication of e-TiO_2 MPs

In an aqueous solution, hydrogen peroxide could be hydrolyzed, and the following reaction occurs:

$$H_2O_2 \leftrightarrow H^+ + HO_2^- \tag{3.6}$$

causing the solution to be acidic [33]. The pH of 30% H_2O_2 would be around 3.

Under 80°C, Ti surface would be oxidated and TiO_2 formed. During this process, the pH of H_2O_2-NH_4F solution decreases, indicating the solution more acidic. Since the oxidation occurred on the surface of TiO_2, in the mixed-oxidation solution, the following electrode reaction occurred:

$$Ti + 2H_2O \rightarrow TiO_2 + 4H^+ + 4e^- \tag{3.7}$$

Which decreased the pH. Also at this stage, the supersaturated Ti^{4+} ions generated by H_2O_2 would be hydrolyzed to TiO_2. Then electrons combined with oxidant and the cathode reaction is

$$HO_2^- + 3H^+ + 2e^- \rightarrow 2H_2O \tag{3.8}$$

After fabrication of TiO_2, fluoride ion could corrode small amount of TiO_2 and form water-soluble complex [27],

$$TiO_2 + 6F^- + 4H^+ \rightarrow [TiF_6]^{2-} + 2H_2O \tag{3.9}$$

which made TiO_2 on the surface separated from plate and generated the mesoporous structure. Fluoride can also cause the reduction of the TiO_2, converts some Ti^{4+} to Ti^{3+} and create oxygen vacancies by charge compensation [16], which is consistent with the XPS and EELS analysis results. In addition, metallic Ti could also be a possible reason for the Ti (III) reduction.

3.3.3 Photocatalytic properties

Figure 3.11(a) shows the UV-vis-NIR spectra of e-TiO_2 and P25. The band gap energy (indirect) of e-TiO_2 can be determined in the Tauc's plot shown in Figure 3.11(b). Two different bandgaps of e-TiO_2 can be figured out. One band gap locates at 3.2 eV, which refers to the band gap of anatase. Another band gap is calculated as 2.4 eV [34], which may be due to the oxygen vacancy states of e-TiO_2 from the voids caused by F^- influence. The band gap of P25 can be also calculated from Figure 3.11(b), which locates at 3.0 eV. Generally, the band gap of anatase is 3.2 eV [35], and rutile 3.0 eV [36]. The e-TiO_2 has higher absorbance of visible light (400-500 nm wavelength) and lower band gap than these mentioned TiO_2 materials, suggesting that e-TiO_2 is more photo-effective under visible light [35, 37, 38].

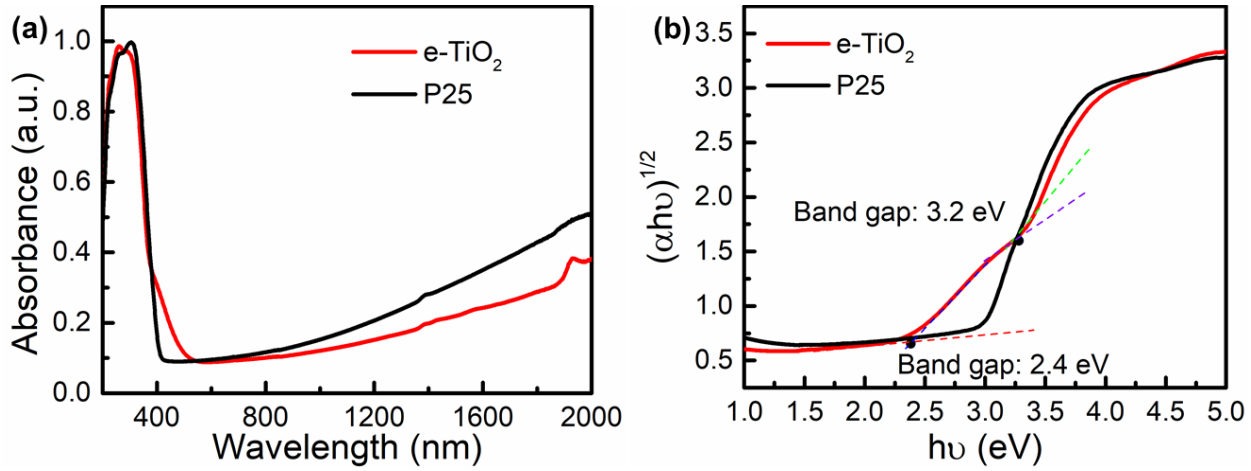

Figure 3.11. (a) UV-vis-NIR spectra curve of e-TiO_2 and P25; (b) Tauc's plot of e-TiO_2 transformed by UV-vis-NIR spectra.

The photocatalytic performance of the e-TiO_2 was investigated by RhB and MB solution degradation experiments under visible light. Table 3.2 shows the residual concentration of the dyes at each stage degraded by e-TiO_2 and P25. Figure 3.12(a) shows the degradation of the dyes within 60 min. Figure 3.12(b) shows the photodegradation kinetic constant *k*, calculated by the following equation [39]:

$$\frac{c}{c_0} = \exp(-kt) \tag{3.10}$$

For RhB degradation, mesoporous e-TiO_2 MPs could adsorb more dyes than P25 after 30 mins stirring. In the photodegradation process, the photodegradation kinetic constant *k* of RhB by e-TiO_2 is $k_{e,R}$ = 0.053 min^{-1}, 4 times as much as P25. Therefore, the e-TiO_2 shows much better photocatalytic performance than P25 under visible light. In this process, pores may play the most

important role. This is because the pores increase the specific surface area of the e-TiO_2 and increase the reaction area, making the degradation process faster. The anatase structure of the e-TiO_2 could also promote the photodegradability. As in the previous report, generally, anatase is more optically active than rutile [40]. Additionally, the single crystalline structure of e-TiO_2 could also promote the photoactivity. The uniformity and regularity of the crystalline structure has been proved to improve the photodegradation efficiency of TiO_2 [14]. Furthermore, trivalent Ti (III) and oxygen vacancies could cause the shift of the energy band gap and improve the photocatalytic performance. Hence, our mesoporous anatase e-TiO_2 shows higher photocatalytic activity than P25.

Table 3.2. The residual concentration of the dyes degraded by e-TiO_2 and P25.

	30 min dark stirring	**1 h degradation under visible light**
RhB (by e-TiO_2)	22%	1%
RhB (by P25)	93%	37%
MB (by e-TiO_2)	38%	17%
MB (by P25)	80%	18%

For MB degradation, the e-TiO_2 shows better adsorption in the initial 30 mins than P25. As shown in Table 2, MB is degraded to 38% by the e-TiO_2. Compared to RhB, the photodegradation rate of MB by e-TiO_2 decreased significantly. Photosensitization is one possible explanation for the selectively photodegradation of RhB instead of MB. RhB has been proved to be photosensitive during the TiO_2 photodegradation [41, 42]. During the step, RhB could also be excited by visible light, which accelerates the self-decomposition, making the degradation rate of RhB higher. Although there is no report to directly explain how photosensitization affects the degradation of MB by TiO_2, based on the RhB process, if MB needs to undergo the same process, it needs to absorb light first. According to Figure 3.13, the absorption peak of RhB locates in the range of 450-600 nm, while MB locates in the range of 550-700 nm. The wavelength of the visible light source is 400-600 nm, which can be well absorbed by RhB, but not by MB. This may be the reason why for e-TiO_2, photodegradation efficiency of MB is worse than RhB. Also, the photodegradation by e-TiO_2 did not perform well compared to P25. It has been reported that the ratio of anatase to rutile affects the photodegradation of MB due to the interaction between these two kinds of

crystallites. When the ratio of anatase and rutile is 4:1, the highest photodegradation efficiency could be obtained [43, 44]. Therefore, e-TiO_2 MPs (anatase main) is not as effective as P25 (20% rutile) for the photodegradation of MB. In addition, according to Figure 3.14, e-TiO_2 is considered as a one-time photocatalyst for both RhB and MB.

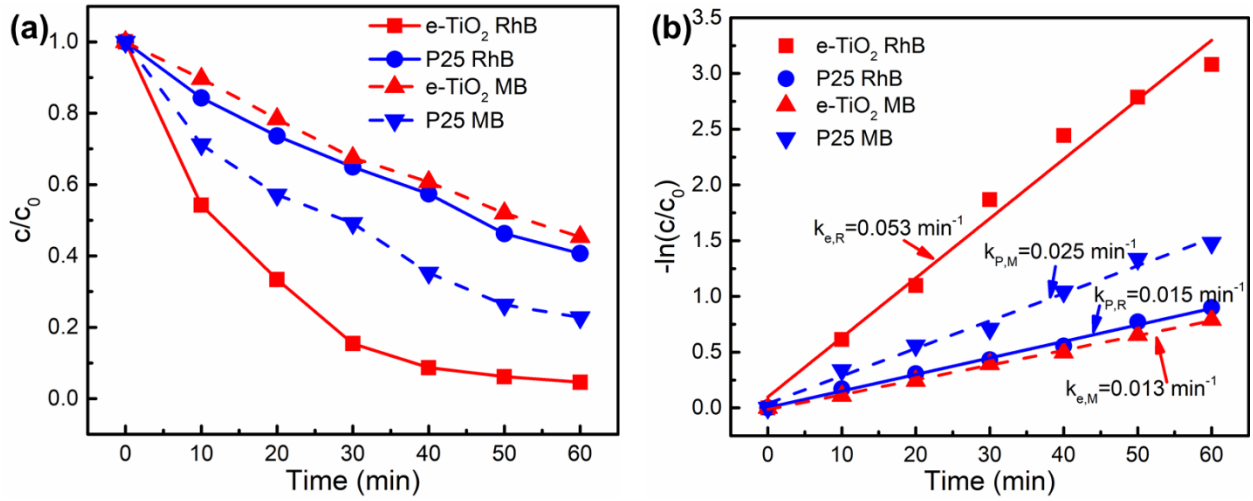

Figure 3.12. Photodegradation and (b) photodegradation kinetic constant calculation of RhB and MB by e-TiO_2 and P25.

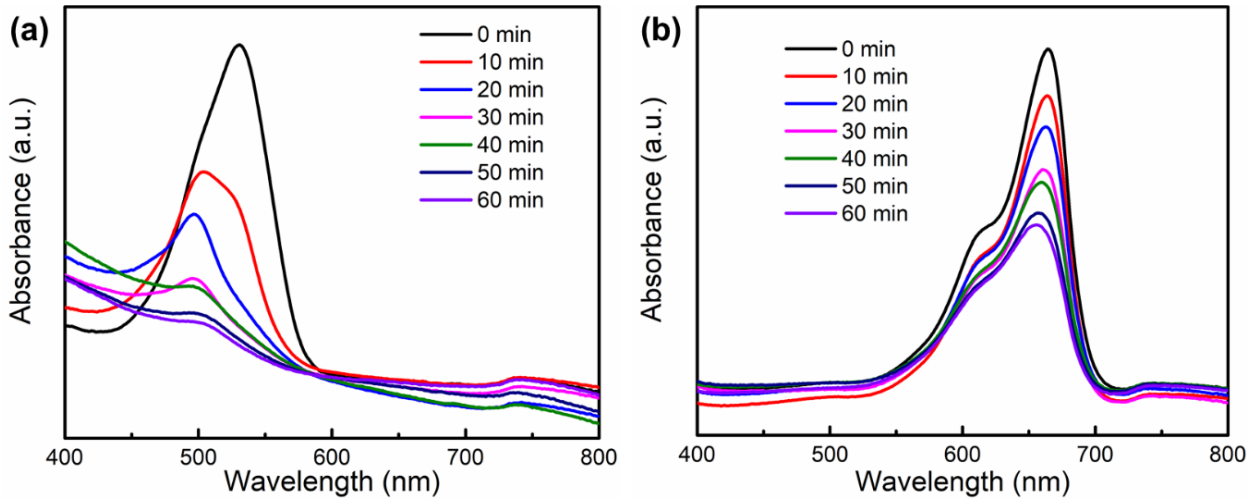

Figure 3.13. The UV-vis absorbance spectra for the photodegradation of (a) Rhodamine B and (b) Methylene blue.

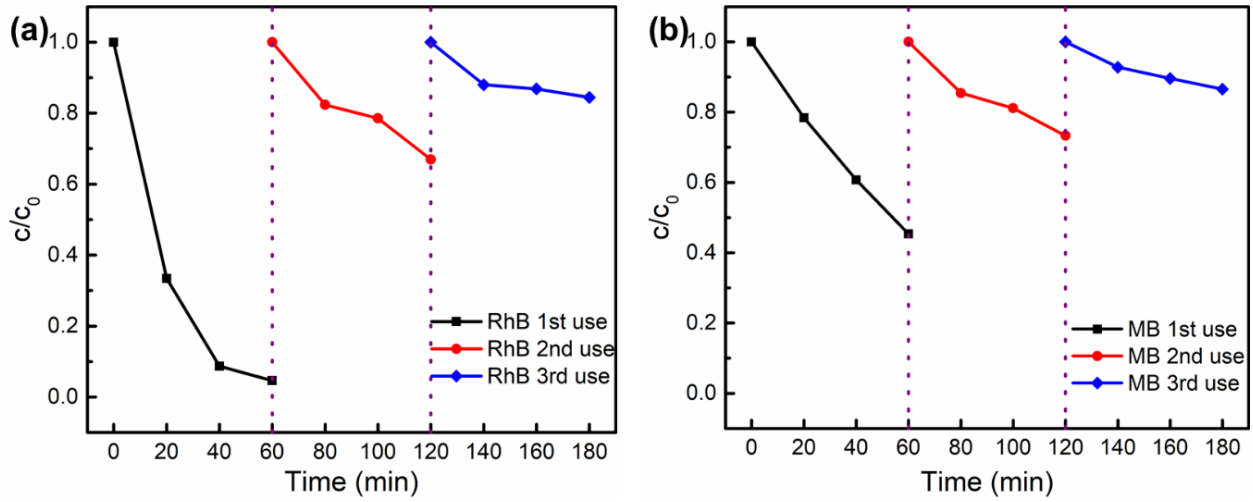

Figure 3.14. The e-TiO_2 photodegradation resuability test results of (a) RhB and (b) MB.

3.3.4 Photodegradation mechanism

During the process, the color of RhB solution would turn to yellow from red, which is supported by UV-vis-NIR data. The absorbance peak of 10^{-5} mol/L Rhodamine B is at around 540 nm (shown in Figure 3.13), which is in the range of yellow light. In the process of degradation, not only did the absorbance peak intensity decrease, but the position also began to shift towards the lower wavelength range (500 nm, which is in the range of green light), making the solution orange, then yellow. Cui et al. [45] reported a degradation mechanism of RhB that makes the intermediate during the process yellow. At first, deethylation reaction happened and RhB degraded to N, N-diethyl-N'-ethylrhodamine (DER). Thereafter, the deethylation continues. Depending on the position of the deethyl group, the intermediate product is also different. If the same side is deethylated, N, N-diethylrhodamine (DR) would be formed, otherwise would be N-ethyl-N'-ethylrhodamine (EER). These two substances have same chemical formula, while their structures are not same. Further deethylation would continue, forming N-ethylrhodamine (ER) and rhodamine (R) successively, and finally destructed its chromophore structure.

According to Honda-Fujishima effect [46], electrons in TiO_2 can be excited by UV light and promote the water decomposition. Hirakawa et al. [47] proposed a mechanism of light absorption by TiO_2 for Honda-Fujishima effect:

$$TiO_2 + h\nu \rightarrow e^- + h^+_{vb} \quad (3.11)$$

$$h^+_{vb} \rightarrow h^+_{tr} \quad (3.12)$$

in which h_{vb}^+ is the hole in the valence band state, and h_{tr}^+ is the trapped hole. The bandgap of e-TiO_2 is 2.4 eV, and it can be excited by visible light and absorb the energy of photons for the

photodegradation [48]. Figure 3.15 shows the mechanism of RhB photodegradation by e-TiO_2. After the absorption of light, the hole of TiO_2 would absorb the electrons in the water molecule and form the reactive oxygen species:

$$H_2O + h_{tr}^{+} \rightarrow H^{+} + \cdot OH \quad (3.13)$$

Based on Cui's photodegradation mechanism [45], RhB molecule would first deethylate:

$$C_{28}H_{31}ClN_2O_3(\text{RhB}) + \cdot OH \rightarrow \cdot C_{26}H_{26}ClN_2O_3 + C_2H_5OH \quad (3.14)$$

Then the intermediate product will combine with hydrogen radical fabricated by H^+ and electrons:

$$\cdot C_{26}H_{26}ClN_2O_3 + H^{+} + e^{-} \rightarrow C_{26}H_{27}ClN_2O_3\ (\text{DER}) \quad (3.15)$$

No gas is generated during this step, which is consistent with the experiment results.

The same mechanism could be applied on DER for the further deethylation process. Both DR and EER is fabricated by the deethylation of DER. After this step, the deethylation continues and ER formed by both DR and EER. These intermediate products make the color of dye solution shift to yellow during the photodegradation. After degraded to Rhodamine (R), the dye continues to degrade, finally become colorless. The photosensitization would also happen during the progress and increase the photodegradation efficiency [41, 42].

As for MB, since its peak did not shift, MB could be one-step degradation to colorless particle. At the beginning of the photodegradation, the energy of light is stilled absorbed by TiO_2 and form reactive oxygen species according to the Honda-Fujishima effect. Then the reactive oxygen species would react with MB molecule by causing the sulfur ring cleavage and degrade the blue dyes [49, 50].

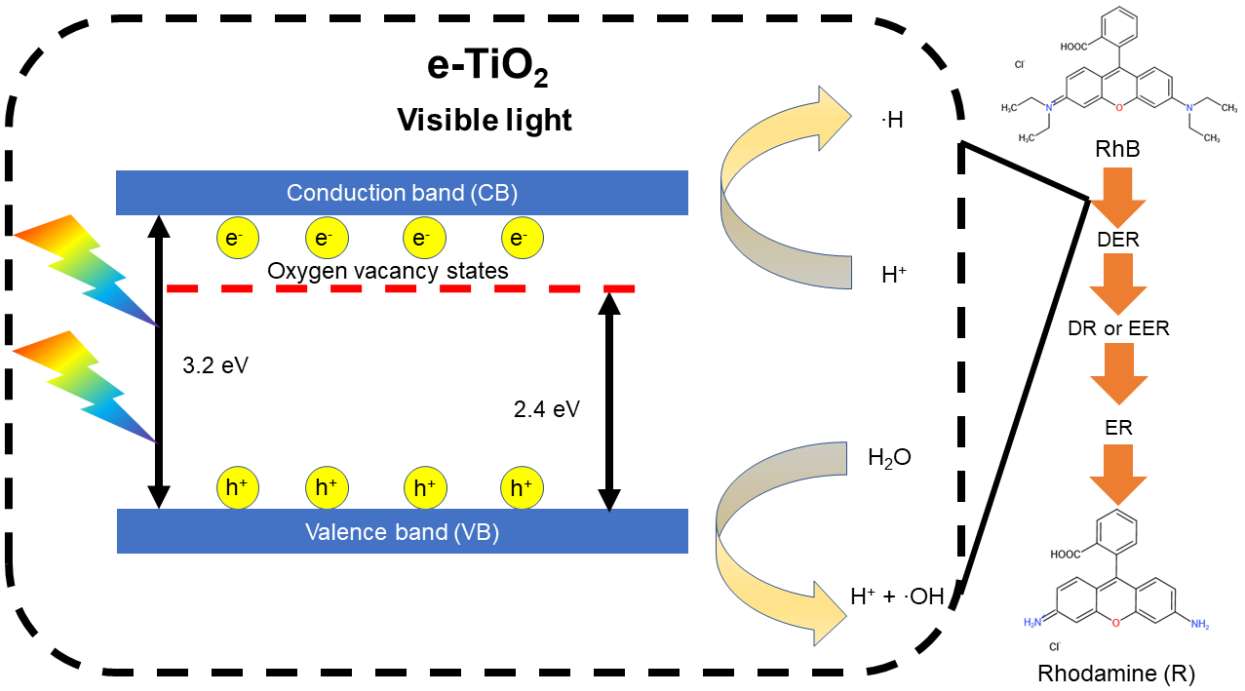

Figure 3.15. Photodegradation mechanism of e-TiO_2 for RhB.

3.4 Conclusions

In summary, we have successfully fabricated e-TiO_2 with high visible light photodegradation activity. Compared to conventional methods, this method only requires raw Ti, H_2O_2, NH_4F, at temperature of 80°C and atmospheric pressure. These requirements are easy to achieve compared to other methods using Ti plate as a raw material, making this method facile. The e-TiO_2 itself also has many advantages compared to commercial P25. Because of the effects of fluoride ions and H_2O_2, e-TiO_2 MPs are one kind of single crystal micromaterials, containing mesopores generated by oxygen vacancies and Ti (III) component. These modifications would lead to superior performances, such as high adsorption for dyes. Furthermore, e-TiO_2 has been proved to have much better photodegradation efficiency. When degrade RhB under visible light, the photodegradation kinetic constant of e-TiO_2 could be 4 times as much as P25. Therefore, the present work provides a facile route to fabricate single crystal TiO_2 with mesoporous structure for high efficiency visible light dye photodegradation.

References

1. Chen, X. and S.S. Mao, *Titanium Dioxide Nanomaterials: Synthesis, Properties, Modifications, and Applications.* Chemical Reviews, 2007. **107**(7): p. 2891-2959.

2. Ohtani, B., et al., *What is Degussa (Evonik) P25? Crystalline composition analysis, reconstruction from isolated pure particles and photocatalytic activity test.* Journal of Photochemistry and Photobiology A: Chemistry, 2010. **216**(2): p. 179-182.

3. Jiang, X., et al., *Anatase and rutile in evonik aeroxide P25: Heterojunctioned or individual nanoparticles?* Catalysis Today, 2018. **300**: p. 12-17.

4. Ge, Y., et al., *Visible-light-active TiO_2 photocatalyst for efficient photodegradation of organic dyes.* Optical Materials, 2021. **115**: p. 111058.

5. Humayun, M., et al., *Modification strategies of TiO_2 for potential applications in photocatalysis: A critical review.* Green Chemistry Letters and Reviews, 2018. **11**(2): p. 86-102.

6. Park, J.T., et al., *A facile graft polymerization approach to N-doped TiO_2 heterostructures with enhanced visible-light photocatalytic activity.* Materials Letters, 2017. **202**: p. 66-69.

7. Choi, W., A. Termin, and M.R. Hoffmann, *The Role of Metal Ion Dopants in Quantum-Sized TiO_2: Correlation between Photoreactivity and Charge Carrier Recombination Dynamics.* The Journal of Physical Chemistry, 1994. **98**(51): p. 13669-13679.

8. Dong, J., et al., *Defective Black TiO_2 Synthesized via Anodization for Visible-Light Photocatalysis.* ACS Applied Materials & Interfaces, 2014. **6**(3): p. 1385-1388.

9. Naik, A.P., et al., *Super porous TiO_2 photocatalyst: Tailoring the agglomerate porosity into robust structural mesoporosity with enhanced surface area for efficient remediation of azo dye polluted waste water.* Journal of Environmental Management, 2020. **258**: p. 110029.

10. Zhu, S., et al., *Solution Plasma-Synthesized Black TiO_2 Nanoparticles for Solar–Thermal Water Evaporation.* ACS Applied Nano Materials, 2021. **4**(4): p. 3940-3948.

11. Xin, X., et al., *Management on the location and concentration of Ti^{3+} in anatase TiO_2 for defects-induced visible-light photocatalysis.* Applied Catalysis B: Environmental, 2015. **176-177**: p. 354-362.

12. Xu, Y., et al., *Introducing Ti^{3+} defects based on lattice distortion for enhanced visible light photoreactivity in TiO_2 microspheres.* RSC Advances, 2017. **7**(52): p. 32461-32467.

13. Zheng, X., et al., *Mesoporous TiO_2 Single Crystals: Facile Shape-, Size-, and Phase-Controlled Growth and Efficient Photocatalytic Performance.* ACS Applied Materials & Interfaces, 2013. **5**(21): p. 11249-11257.

14. Cheng, F., et al., *Porous single-crystalline titanium dioxide at 2 cm scale delivering enhanced photoelectrochemical performance.* Nature Communications, 2019. **10**(1): p. 3618.

15. Xing, H., W. Wen, and J.-M. Wu, *Enhanced UV photoactivity of Ti^{3+} self-doped anatase TiO_2 single crystals hydrothermally synthesized using Ti-H_2O_2-HF reactants.* Journal of Photochemistry and Photobiology A: Chemistry, 2019. **382**: p. 111958.

16. Yu, J.C., et al., *Effects of F^- Doping on the Photocatalytic Activity and Microstructures of Nanocrystalline TiO_2 Powders.* Chemistry of Materials, 2002. **14**(9): p. 3808-3816.

17. Behnajady, M.A., et al., *Sol-Gel Low-temperature Synthesis of Stable Anatase-type TiO_2 Nanoparticles Under Different Conditions and its Photocatalytic Activity.* Photochemistry and Photobiology, 2011. **87**(5): p. 1002-1008.

18. Cassaignon, S., M. Koelsch, and J.-P. Jolivet, *Selective synthesis of brookite, anatase and rutile nanoparticles: thermolysis of $TiCl_4$ in aqueous nitric acid.* Journal of Materials Science, 2007. **42**(16): p. 6689-6695.

19. National Institute of Standards and Technology. *NIST X-ray Photoelectron Spectroscopy Database*. NIST Standard Reference Database Number 20 2000 2012 Oct 1st. 2021]; Available from: https://srdata.nist.gov/xps/.

20. Bharti, B., et al., *Formation of oxygen vacancies and Ti^{3+} state in TiO_2 thin film and enhanced optical properties by air plasma treatment.* Scientific Reports, 2016. **6**(1): p. 32355.

21. Ruzicka, J.-Y., et al., *XPS and NEXAFS study of fluorine modified TiO_2 nano-ovoids reveals dependence of Ti^{3+} surface population on the modifying agent.* RSC Advances, 2014. **4**(40): p. 20649-20658.

22. Liu, X., W. Chen, and W. Wang, *F^- Serve as Surface Trapping Sites to Promote the Charge Separation and Transfer of TiO_2.* ACS Omega, 2021. **6**(51): p. 35799-35809.

23. Shin, J.-Y., et al., *Oxygen-Deficient $TiO_{2-\delta}$ Nanoparticles via Hydrogen Reduction for High Rate Capability Lithium Batteries.* Chemistry of Materials, 2012. **24**(3): p. 543-551.

24. Xuan, S., et al., *Synthesis of Biocompatible, Mesoporous Fe_3O_4 Nano/Microspheres with Large Surface Area for Magnetic Resonance Imaging and Therapeutic Applications.* ACS Applied Materials & Interfaces, 2011. **3**(2): p. 237-244.

25. Chen, D., et al., *Synthesis of Monodisperse Mesoporous Titania Beads with Controllable Diameter, High Surface Areas, and Variable Pore Diameters (14−23 nm).* Journal of the American Chemical Society, 2010. **132**(12): p. 4438-4444.

26. Cychosz, K.A. and M. Thommes, *Progress in the Physisorption Characterization of Nanoporous Gas Storage Materials.* Engineering, 2018. **4**(4): p. 559-566.

27. Wang, X., et al., *Fluoride concentration controlled TiO_2 nanotubes: the interplay of microstructure and photocatalytic performance.* RSC Advances, 2016. **6**(22): p. 18333-18339.

28. Nussbaumer, H.J., *The Fast Fourier Transform*, in *Fast Fourier Transform and Convolution Algorithms*, H.J. Nussbaumer, Editor. 1981, Springer Berlin Heidelberg: Berlin, Heidelberg. p. 80-111.

29. Ovchinnikov, V., *Reactive-Vacancy Mechanism of Pore Growth in Oxide Films.* ECS Journal of Solid State Science and Technology, 2021. **10**(10): p. 103007.

30. Malis, T., S.C. Cheng, and R.F. Egerton, *EELS log-ratio technique for specimen-thickness measurement in the TEM.* Journal of Electron Microscopy Technique, 1988. **8**(2): p. 193-200.

31. Seah, M.P. and W.A. Dench, *Quantitative electron spectroscopy of surfaces: A standard data base for electron inelastic mean free paths in solids.* Surface and Interface Analysis, 1979. **1**(1): p. 2-11.

32. Huang, C.-N., et al., *Nonstoichiometric Titanium Oxides via Pulsed Laser Ablation in Water.* Nanoscale Research Letters, 2010. **5**(6): p. 972.

33. Busch, M.A. and K.W. Busch, *Bleaches and Sterilants*, in *Encyclopedia of Analytical Science (Third Edition)*, P. Worsfold, et al., Editors. 2019, Academic Press: Oxford. p. 300-315.

34. Makuła, P., M. Pacia, and W. Macyk, *How To Correctly Determine the Band Gap Energy of Modified Semiconductor Photocatalysts Based on UV–Vis Spectra.* The Journal of Physical Chemistry Letters, 2018. **9**(23): p. 6814-6817.

35. Choudhury, B. and A. Choudhury, *Oxygen defect dependent variation of band gap, Urbach energy and luminescence property of anatase, anatase–rutile mixed phase and of rutile phases of TiO_2 nanoparticles.* Physica E: Low-dimensional Systems and Nanostructures, 2014. **56**: p. 364-371.

36. Pascual, J., J. Camassel, and H. Mathieu, *Fine structure in the intrinsic absorption edge of TiO_2.* Physical Review B, 1978. **18**(10): p. 5606-5614.

37. Xu, J., et al., *Facile and Large-scale Synthesis of Defective Black TiO_{2-x}(B) Nanosheets for Efficient Visible-light-driven Photocatalytic Hydrogen Evolution.* Catalysts, 2019. **9**(12).
38. Feng, N., et al., *Unravelling the Efficient Photocatalytic Activity of Boron-induced Ti^{3+} Species in the Surface Layer of TiO_2.* Scientific Reports, 2016. **6**(1): p. 34765.
39. Gómez, M., et al., *Modelling and experimental checking of the influence of substrate concentration on the first order kinetic constant in photo-processes.* Journal of Environmental Management, 2016. **183**: p. 818-825.
40. Luttrell, T., et al., *Why is anatase a better photocatalyst than rutile? - Model studies on epitaxial TiO_2 films.* Scientific Reports, 2014. **4**(1): p. 4043.
41. Ma, Y. and J.-n. Yao, *Photodegradation of Rhodamine B catalyzed by TiO_2 thin films.* Journal of Photochemistry and Photobiology A: Chemistry, 1998. **116**(2): p. 167-170.
42. Wu, J.-M. and T.-W. Zhang, *Photodegradation of rhodamine B in water assisted by titania films prepared through a novel procedure.* Journal of Photochemistry and Photobiology A: Chemistry, 2004. **162**(1): p. 171-177.
43. Zaw, Y.Y., et al., *Effect of Anatase/Rutile Phase Ratio on the Photodegradation of Methylene Blue under UV Irradiation.* Materials Science Forum, 2020. **998**: p. 78-83.
44. Tichapondwa, S.M., J.P. Newman, and O. Kubheka, *Effect of TiO_2 phase on the photocatalytic degradation of methylene blue dye.* Physics and Chemistry of the Earth, Parts A/B/C, 2020. **118-119**: p. 102900.
45. Cui, Y., et al., *Effect of Dual-Cocatalyst Surface Modification on Photodegradation Activity, Pathway, and Mechanisms with Highly Efficient Ag/$BaTiO_3$/MnO_x.* Langmuir, 2020. **36**(2): p. 498-509.
46. Fujishima, A. and K. Honda, *Electrochemical Photolysis of Water at a Semiconductor Electrode.* Nature, 1972. **238**(5358): p. 37-38.
47. Hirakawa, T. and Y. Nosaka, *Properties of $O_2^{\bullet-}$ and OH• Formed in TiO_2 Aqueous Suspensions by Photocatalytic Reaction and the Influence of H_2O_2 and Some Ions.* Langmuir, 2002. **18**(8): p. 3247-3254.
48. Liu, H., et al., *Extended visible light response of binary TiO_2-Ti_2O_3 photocatalyst prepared by a photo-assisted sol–gel method.* Applied Catalysis A: General, 2006. **299**: p. 218-223.

49. Wang, Q., S. Tian, and P. Ning, *Degradation Mechanism of Methylene Blue in a Heterogeneous Fenton-like Reaction Catalyzed by Ferrocene.* Industrial & Engineering Chemistry Research, 2014. **53**(2): p. 643-649.

50. Zuo, R., et al., *Photocatalytic Degradation of Methylene Blue Using TiO_2 Impregnated Diatomite.* Advances in Materials Science and Engineering, 2014. **2014**: p. 170148.

Chapter 4

Facile Modification of TiO_2 Nanoparticles with H_2O_2 + NH_4F for Enhanced Visible Light Photodegradation of Rhodamine B and Methylene Blue

4.1 General Introduction

Using metal oxide nanomaterials is a common countermeasure for photodegrading dyes due to their supreme performances [1]. Titanium dioxide (TiO_2) has stood out among metal oxide materials because of higher stability, non-toxicity, and UV-region bandgap (~ 3 eV) [2, 3]. P25-TiO_2 (hereinafter called P25), one commercial TiO_2 product, has been widely used for the photodegradation of organic pollutants [4, 5]. P25 has been proved to be efficient by ultraviolet light degradation, while for visible light, the performance is limited [6].

For this reason, researchers have been working on the modification of TiO_2 materials to improve its visible light performance. Doping other elements is an effective way to improve the visible light performance of TiO_2 [7]. Iron, tungsten, and manganese are common elements used for the visible light photodegradation improvement of TiO_2 for different cases [8-10]. Co-doping is also fruitful for the enhancement of visible light photodegradation efficiency [11-13].

Apart from metals, non-metal materials, such as boron, nitrogen, carbon, iodine, and phosphorus, could also be used for TiO_2 modification [14-19]. Fluoride has been proved to be effective on the modification of titania materials [20]. Although rutile-TiO_2 and anatase-TiO_2 have been determined to be metastable near room temperature [21, 22], fluorides could react with them, making modification possible [23, 24]. It has been proved that fluoride materials can modify TiO_2 particles and improve its visible light activity [25, 26]. In addition to the elements above, hydrogen peroxide (H_2O_2) is also effective for the sensitization of TiO_2 and increase the visible light photodegradation efficiency [27]. In our previous study, it has been proved that H_2O_2 is effective on the fabrication of ellipsoidal TiO_2, which has enhanced visible light photodegradation activity [28].

Herein, we developed a facile modification method to increase the visible light photodegradation efficiency of TiO_2, which only uses hydrogen peroxide (H_2O_2) and NH_4F. We modified the commercial P25 and TiO_2 samples fabricated from titanium isopropoxide (TTIP) by using H_2O_2 + NH_4F. The samples before and after modification are tested for the characterization and property analysis. This modification method is able to increase the specific surface area of

TiO_2, change the color and lower the band gap. Rhodamine B (RhB) and methylene blue (MB) are used to test under visible light (400 nm-600 nm) performance to compare the photodegradation efficiency for the before and after modification samples. All three modified samples show higher visible light efficiency for RhB. The modification is also proved to be effective on TiO_2 for the visible light photodegradation of MB. The possible mechanisms of TiO_2 fabrication, H_2O_2 + NH_4F modification, and dye photodegradation are also discussed in the manuscript.

4.2. Materials and Methods

4.2.1 Synthesis of Different TiO_2 Nanoparticles

1 M sodium hydroxide solution (NaOH, Kanto Chemical Co., Inc, pH ~ 14) was used as the alkaline solution for the hydrolysis of TTIP ($[(CH_3)_2CHO]_4Ti$, Wako Pure Chemical Cooperation, 95%), while 1 M hydrochloric acid (HCl, Wako Pure Chemical Cooperation, pH ~ 0) was chosen as the acidic solution. 1 mL of the TTIP was added into 10 mL of the solution with different pH and stirred (~ 300 rpm) in a dark chamber for 24 h. The precipitates were collected by centrifugation and purified with ethanol three times, then dried in an oven for 24 h at 50°C. P25 (Evonik Aeroxide) was also chosen as the TiO_2 material for the further modification.

4.2.2 Modification by H_2O_2 + NH_4F Solution

300 mg of ammonia fluoride (NH_4F, 97%, Wako Pure Chemical Cooperation, Wako special grade) was added into 90 mL of hydrogen peroxide (30 wt%, H_2O_2, Kanto Chemical Co., inc.) to control the mass fraction at 3.3 wt%. Then, 0.1 g of TiO_2 was added into 10 mL of solution and kept at 80°C for 72 h. The products were collected by centrifugation and purified for characterization.

4.2.3 Structural Characterization

All TiO_2 nanoparticles were observed by a field emission scanning electron microscope (FESEM, JEOL JSM-7001F) operated at 15 kV and a transmission electron microscope (TEM, JEOL JEM-2000FX) operated at 200 kV. High-resolution transmission electron microscopy (HRTEM) images were taken by a scanning transmission electron microscopy (FEI Titan G3 60-300) operated at 300 kV. X-ray diffraction (XRD) measurement were conducted using an X-ray diffractometer (RIGAKU Miniflex 600) with the Cu Kα (λ = 1.5406 Å) radiation as the source. A photoelectron spectrometer with monochromatic Mg Kα radiation was used for X-ray photoelectron spectroscopy (XPS, JEOL JPS-9200). UV-vis absorption spectra were measured

using a UV-vis spectrometer (JASCO V-770 spectrophotometer). The band gap information was obtained from the Tauc's plot calculated by the spectrometer.

4.2.4 Photodegradation Experiments

Rhodamine B (RhB, 10^{-5} M, $C_{28}H_{31}ClN_2O_3$, Wako Pure Chemical Cooperation) and Methylene blue (MB, 10^{-5} M, $C_{16}H_{18}N_3SCl \cdot 3H_2O$, Wako Pure Chemical Cooperation) worked for the photodegradation tests as the dyes. All the TiO_2 samples were tested by RhB and MB solution in a dark chamber, respectively. 50 mL of the dye solution were prepared for the test with 20 mg of TiO_2 nanoparticles. A visible light source (Hamamatsu Lightningcure LC8, 400-600 nm) was used for illumination. All photocatalysts were stirred (~ 300 rpm) in dye solution for 30 min to spread in water better and to eliminate the dye adsorption before the photodegradation process. These experiments were all set for 1 h, and during this period, a 2-mL aliquot was taken every 10 minutes for UV-vis spectra measurement of absorbance.

.3. Results and Discussion

4.3.1 Sample Characterization of TiO_2 samples

Table 4.1 shows the properties of all TiO_2 samples used in this research with the sample names and the corresponding fabrication method. Figure 4.1 shows the SEM images of them. The as-prepared samples are shown in the above, while after-modification samples are shown in the below. Among the three samples without H_2O_2 + NH_4F modification, P25 and TH shows the almost same size, with an average diameter of 20 nm. TN is different in size from the P25 and TH, which size is over 100 nm, and presents in lump form. This result suggests that TNF has a lower specific surface area than P25 and TH. For the three samples after the H_2O_2 + NH_4F modification, they all have similar sizes (~ 20 nm). Compared to their pre-modification samples, PF and THF do not show changes in size, indicating that modification does not contribute to the size change. For TNF, after modification, the size of particle become smaller, which means that this modification has corroded TN and breaks it into smaller particles to lead to an increase in the specific surface area.

Table 4.1. Properties of all TiO_2 samples prepared in the research.

Sample Name	Fabrication Method	Modification	Structure	Specific Surface Area (m^2/g)
P25	Commercial chemical	None	Anatase (00-064-0863) Rutile (00-001-1292)	54.4

	(Evonik Aeroxide)			
PF	Commercial chemical (Evonik Aeroxide)	H_2O_2 + NH_4F	Anatase + Rutile	65.0
TH	TTIP + HCl	None	Rutile + Anatase	147.5
THF	TTIP + HCl	H_2O_2 + NH_4F	Anatase + Rutile	114.7
TN	TTIP + NaOH	None	Amorphous	24.1
TNF	TTIP + NaOH	H_2O_2 + NH_4F	Amorphous	266.8

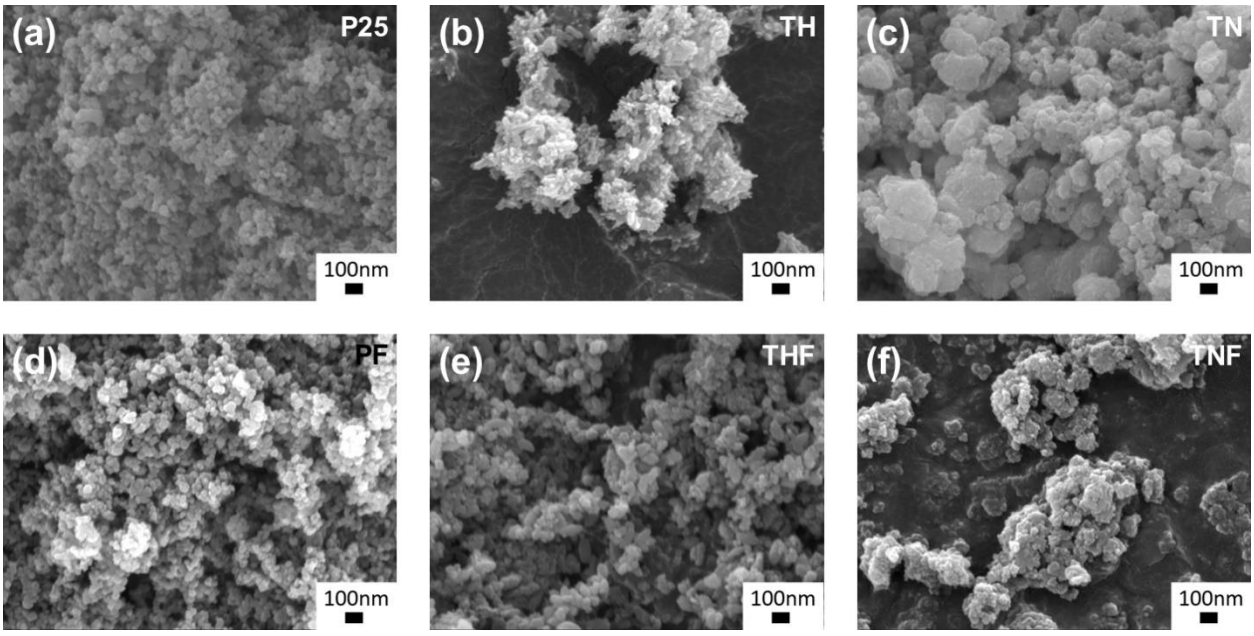

Figure 4.1. SEM images of TiO_2 samples: (a) P25, (b) TH, (c) TN, (d) PF, (e) THF and (f) TNF.

The XRD patterns are shown in Figure 2 for TH, TN, P25 and their as-modified samples. As shown in Figure 2(a), both anatase and rutile peaks are detected in P25 and PF samples, showing an anatase-rutile mixed phase. Compared to P25, the peak of PF dose not shift, suggests that the crystal structure doesn't change during the modification. For TH and THF, as shown in Figure 2(b), TH is mainly rutile, while THF is mainly anatase after the modification. Figure 2(c) shows the XRD results of TN and TNF. Different from the previous samples, the XRD pattern of TN and TNF suggests that TN and TNF have amorphous structure [29].

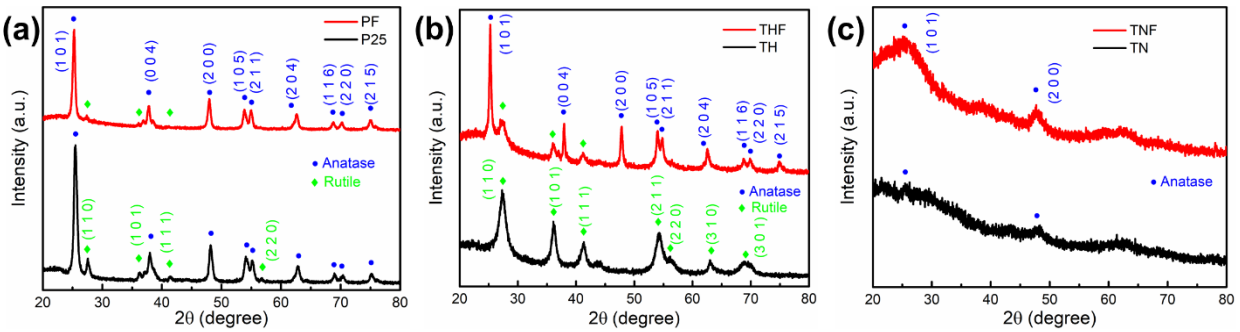

Figure 4.2. XRD patterns of (a) P25 and PF (b) TH and THF and (c) TN and TNF.

XPS was carried out to analyze the surface of TiO_2 different samples. The results of Ti 2p range and O 1s range are collected and shown in Figure 4.3. Figure 4.3(a) shows the XPS of P25 and PF. The XPS spectra of P25 is based on the previous report [28], which is used as a control group. The peak located at 458 eV is determined as the TiO_2 Ti 2p3/2 peak, while 464 eV is recognized as the TiO_2 Ti 2p1/2 peak. There is no peak shift in Ti 2p spectra, however, the O 1s spectra changes after the treatment. P25 only have one peak located at 529 eV, which is the typical TiO_2 O peak. For PF, in addition to the peak of 529 eV, there is another peak, which is at 531 eV. This new peak suggests the existence of oxygen vacancies after the modification, which may be because of H_2O_2 + NH_4F [26]. Figure 3(b) shows the XPS results of TH and THF. In Ti 2p spectra, both TH and THF show standard TiO_2 2p peaks (458 eV for Ti 2p3/2 and 464 eV for Ti 2p1/2). However, for TH and THF, the two Ti peaks shift slightly, suggesting that the surface of TH and THF are not totally same. For the O spectra, TH shows three different peaks, while THF shows two different peaks. The XPS spectra indicates that both TH and THF has oxygen vacancies on the surface. The region with more oxygen vacancies, the higher the surface binding energy [30]. The effect of H_2O_2 + NH_4F could cause the reduction and re-oxidation of Ti (IV) and formed new TiO_2, which may block some oxygen vacancies on the surface of these samples [26, 28]. Also, the O 1s peaks are not at the same position, suggesting the difference of the surface properties. For the XPS results of TNF, Ti peaks change after the modification. TiO_2 Ti 2p3/2 peak (locates at 458 eV) and 2p1/2 peak (464 eV) are indicated in Figure 4.3(c), which are recognized as red line and blue line. In addition, purple line and green line show that the peaks of Ti_2O_3 Ti 2p3/2 and Ti_2O_3 Ti 2p1/2 appear on the surface of TNF [31]. According to Figure 4.4, after modification, two fluoride 1s peaks are detected by XPS. The peaks locate at 684 eV and 687 eV represent the F 1s peak of F^- and F 1s peak of $TiO_{2-x}F_x$, respectively [26, 32]. The results indicate that F^- has successfully reacted with all TiO_2 samples.

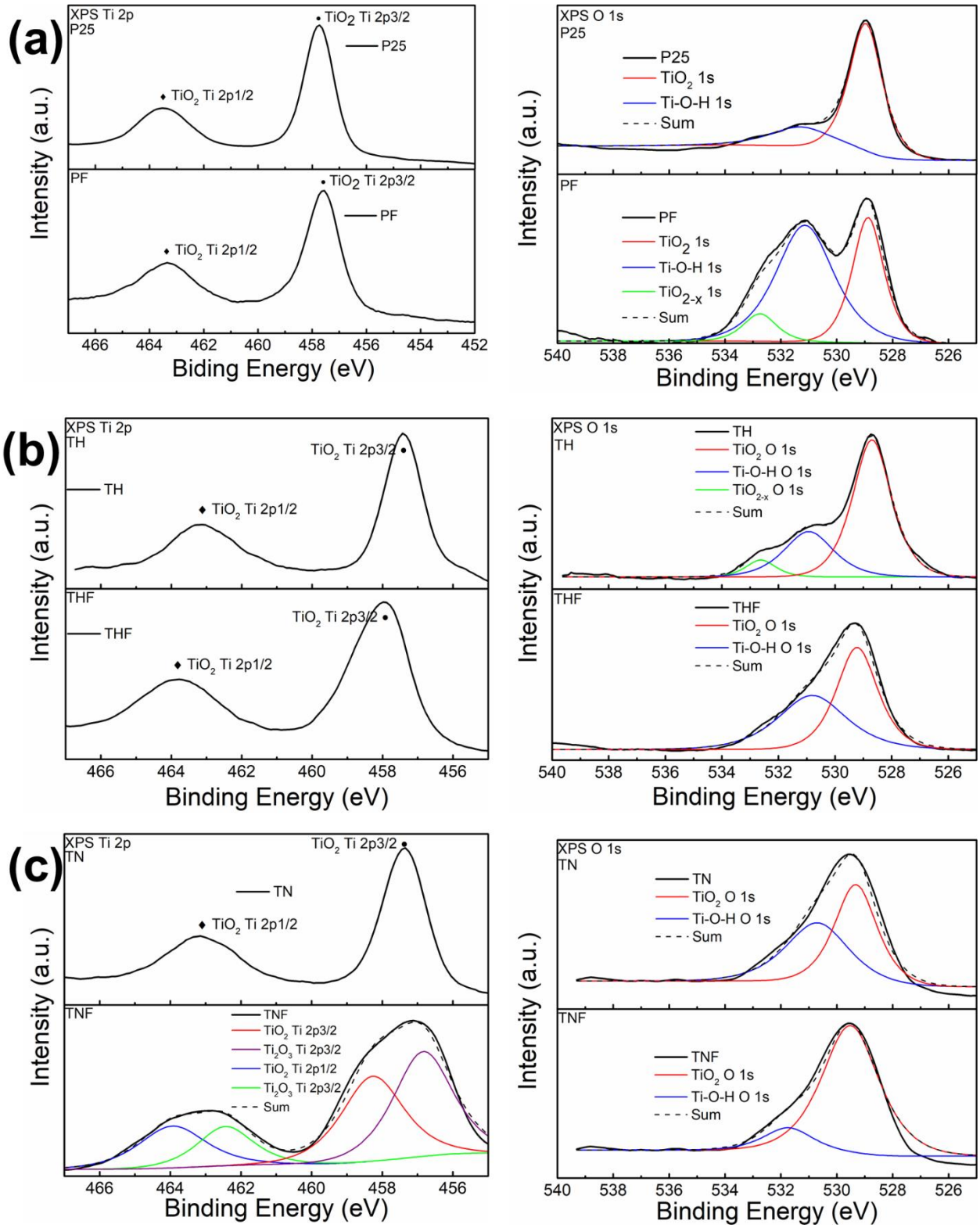

Figure 4.3. XPS spectra of (a) P25 and PF; (b) TH and THF; (c) TN and TNF.

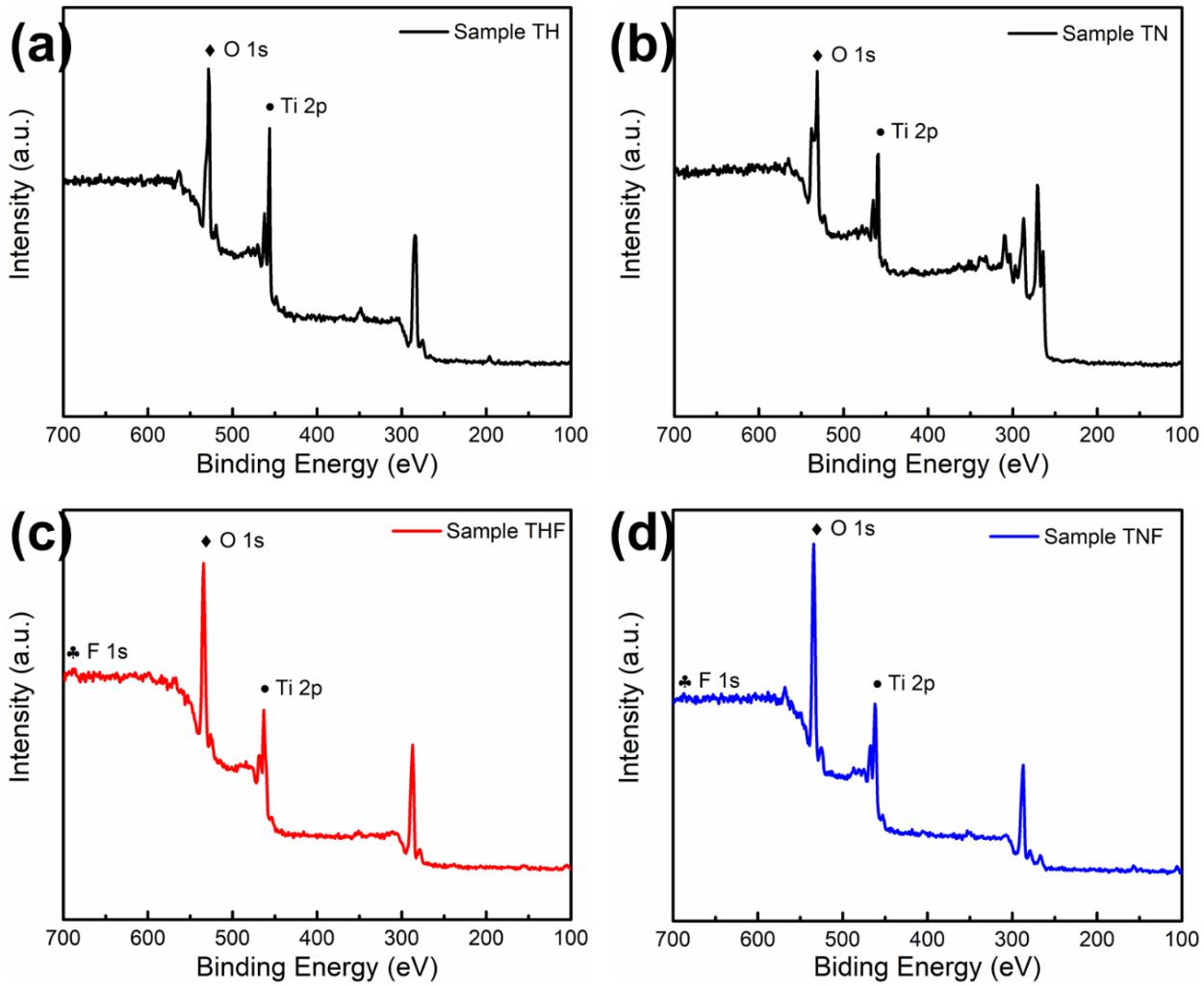

Figure 4.4. XPS wide scan of (a) TH, (b) TN, (c) THF and (d) TNF.

The specific surface area and pore size distribution of TiO_2 samples have been analyzed by the Brunauer–Emmett–Teller (BET) method. As shown in Table 1, TNF shows the highest specific surface area, which is 266.8 m^2/g, almost five times that of P25. After the H_2O_2 + NH_4F modification, the specific surface of TN series increases the most. As SEM image (Figure 1) shows, TN is blocky with large size, which may be the reason for its low specific surface area. After modification, blocky TN becomes small-sized TNF. P25 series don't show significant surface area increase, which is presumably due to the small size of P25. The specific surface area of TH decreases after the modification, which is different from other samples. This is presumably because of the TiO_2 rearrangement caused by F^- ions [26]. For sample TH, fluoride would also cause the reduction of TiO_2, while H_2O_2 can re-oxidize Ti (III) to Ti (IV). The re-formed TiO_2 is possible to block the holes, making THF reconstituted into large spheres, and causing the specific surface area

to decrease [33]. From the XRD pattern of THF in Figure 2, the full width at half maxima (FWHM) of THF is smaller than that of TH, which also indicates the larger particle size of THF.

For detailed structural characterization, TEM observations are carried out for the all six TiO_2 samples. As shown in Figure 4.5, compared to P25, PF doesn't show noticeable size change, however, its surface becomes rough. These results suggest that H_2O_2 + NH_4F treatment doesn't change the size but corrodes the surface of P25. For TH and THF, the shape changes from strip (less than 100 nm) to ellipsoid (~ 100 nm) by the modification, which may answer the question why the specific surface area of THF is less than TH. According to the TEM images, TH has a high probability of being composed of many small particles. The modification process could cause the rearrangement of these small particles, making the specific surface area lower [26, 33]. The shape of TN also changed after the modification. The size of TN is larger (over 100 nm), while TNF is much smaller (~ 20 nm). These results indicate that the H_2O_2 + NH_4F modification successfully corrodes TN and breaks it apart. The selected area electron diffraction (SAED) patterns of each TiO_2 sample are also shown in Figure 4.5. P25, PF TH and THF are all anatase-rutile binary structure. Although TH and THF have both rutile and anatase structure, just as P25 and PF. The SAED patterns of TH and THF are not as clear as P25 and PF, suggesting that TH and THF are chemically disordered. This result suggests that TH and THF may have higher chemical activity than P25 and PF [34]. Also, SAED patterns of TN and TNF can prove their amorphic structure. In TEM characterization, the antithesis between overfocus and underfocus TEM images of same area (as shown in Figure 4.6) can figure out the pores in the area. Compared to these overfocus and underfocus images, we can see that P25 and PF don't have pores. Therefore, the specific surfaces areas of P25 and PF are much lower than other samples. TNF cannot see the pores clearly, neither. This result may be due to its small size, making it easier to separate rather than introduction of pores.

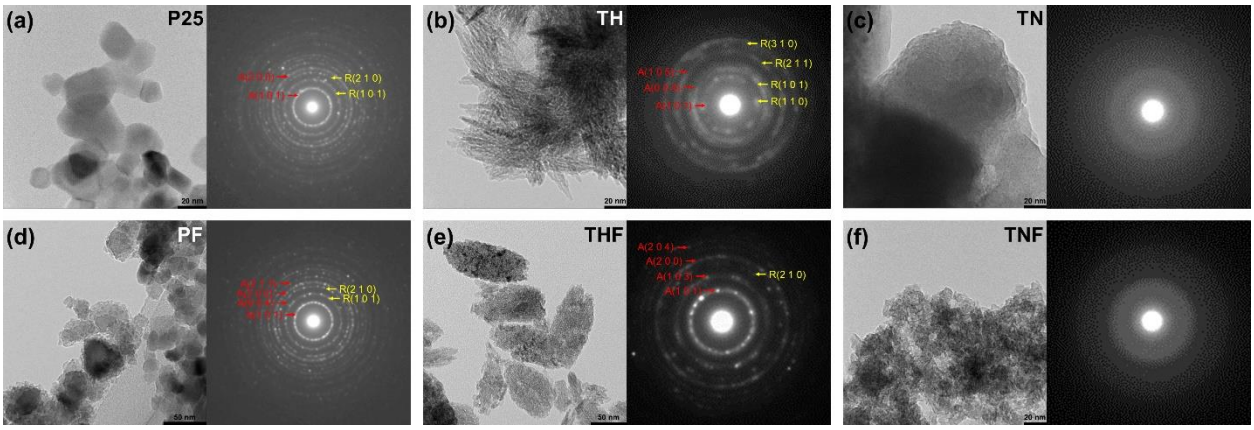

Figure 4.5. TEM images of TiO_2 samples with SAED patterns.

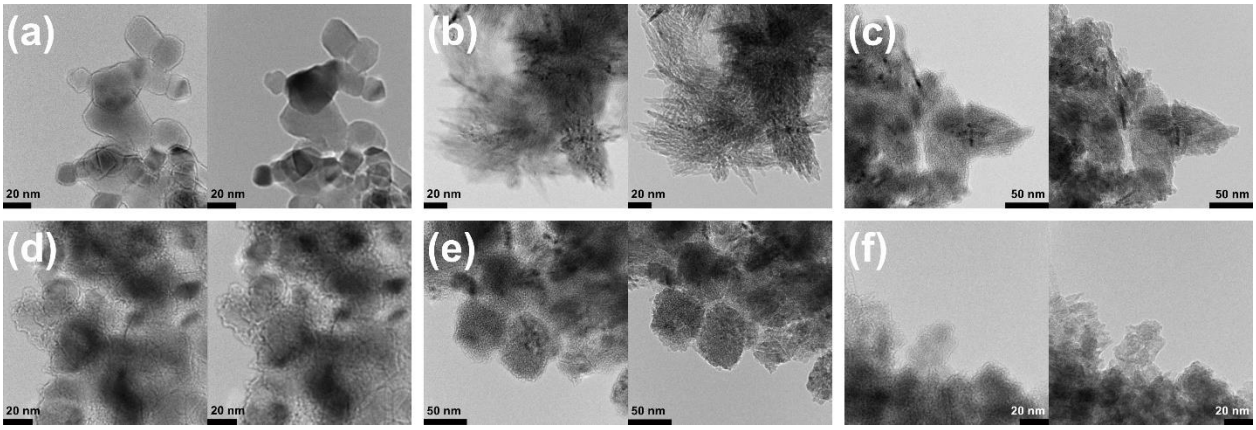

Figure 4.6. Overfocus (left) and underfocus (right) TEM images of TiO_2 samples: (a) P25, (b) TH, (c) TN, (d) PF, (e) THF and (f) TNF.

Scanning Transmission Electron Microscopy (STEM) is also used for the characterization of the six TiO_2 samples. Figure 4.7 shows the HRTEM images of TH, TN, THF and TNF. In TH and THF, regular arrangements can be seen, suggesting that TH and THF are crystalline structure. In addition, the atomic arrangements have different orientation, indicating that TH and THF are polycrystalline. Fast Fourier Transform (FFT) and Inverse Fast Fourier Transform (IFFT) can be used for micro characterization in detail [35]. The bottom right partial enlarged view shows the mask filtered IFFT image for TH ((1 1 0) plane of rutile) and THF ((1 0 1) plane of anatase). These IFFT images depict several defects in these materials, which could clarify the reason why TH and THF work well in photodegradation, which will be discussed later. Furthermore, the interplanar spacing of both samples calculated by IFFT match the actual data (plane (1 1 0) of rutile: 3.2 Å, plane (1 0 1) of anatase: 3.5 Å). These results also revealed that TH is composed of rutile and THF is of anatase, respectively. Figure 5(b) and (d) show the detail of TN and TNF, while partial

enlarged perspectives are shown in the corresponding bottom right. TN and TNF are mainly amorphous, which is consistent with the XRD results. According to the partial enlarged view, TN still have some crystal structures, which are shown as bright spots in the FFT image, but the FFT image of TNF does not show any bright spots, indicating that TNF in the HRTEM region is amorphous.

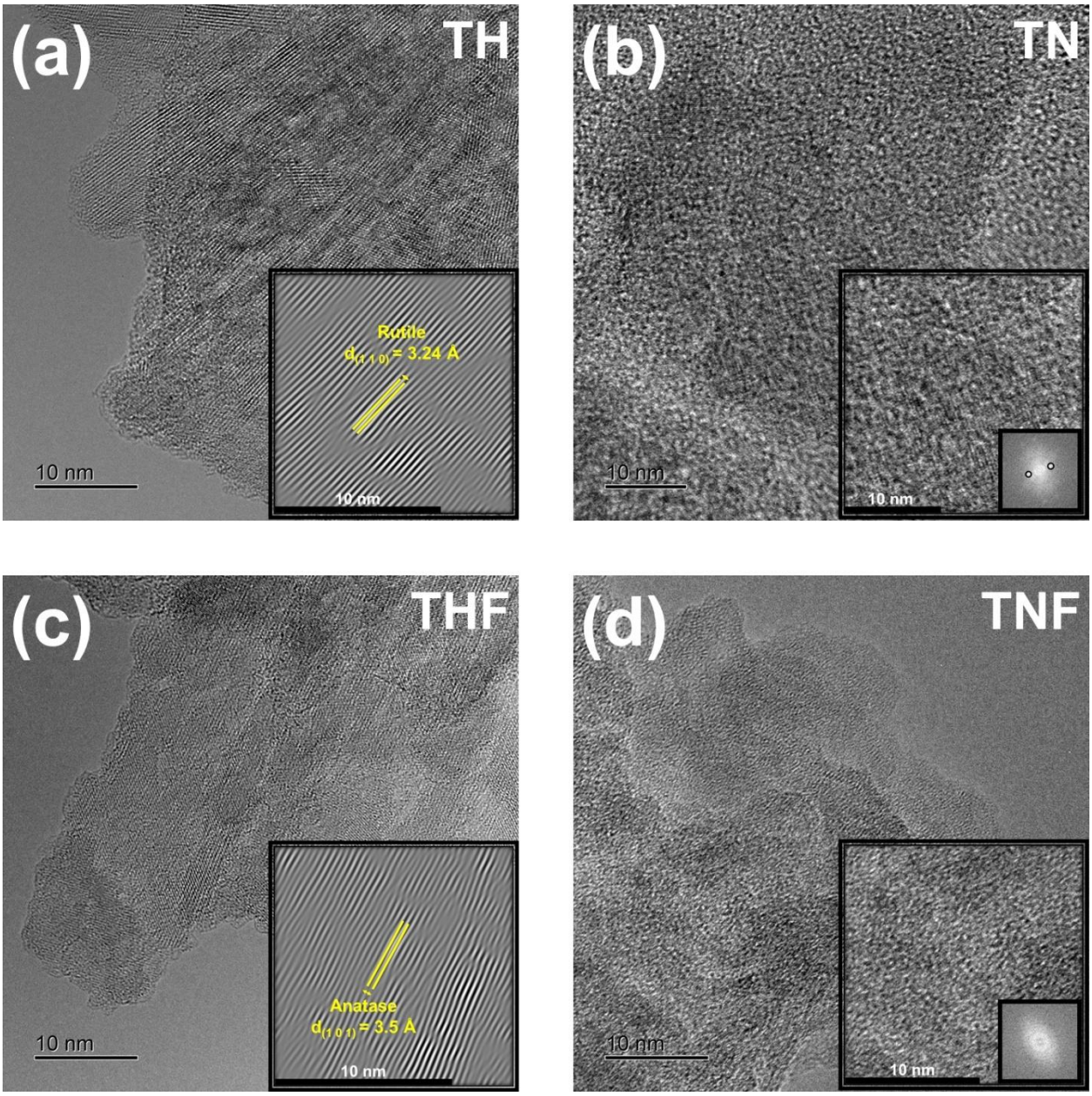

Figure 4.7. HRTEM images of (a) TH (b) TN (c) THF (d) TNF.

4.3.2 The formation mechanism of TiO_2 samples.

TTIP is an effective material for the fabrication of TiO_2 nanoparticles.

$$\mathrm{TTIP} \xrightarrow{\mathrm{Hydrolysis}} \mathrm{TiO_2} \quad (1)$$

In the solution with different pH, TTIP could fabricate TiO_2 with different structure. Acidic solution promotes the amorphous-to-crystal process, while alkaline solution inhibits this process [36].

$$\mathrm{TTIP} \xrightarrow{\mathrm{HCl,1M}} \mathrm{Rutile} + \mathrm{Anatase} \quad (2)$$

$$\mathrm{TTIP} \xrightarrow{\mathrm{NaOH,1M}} \mathrm{Amorphous\ TiO_2} \quad (3)$$

Also, the presence of HCl would enhance the transformation of anatase-to-rutile [36], which may be the reason for the high content of rutile in TH.

In the modification process, H_2O_2 and NH_4F could react with TiO_2 particles, corroding the sample and creating pores. For crystal TiO_2 (P25 and TH), low temperature under 100°C would promote the transformation from rutile to anatase [37].

$$\mathrm{Rutile} \xrightarrow{80°\mathrm{C}} \mathrm{Anatase} \quad (4)$$

Fluoride ion is usually considered as a corrosive for TiO_2 [38].

$$\mathrm{TiO_2} + 6\mathrm{F^-} + 4\mathrm{H^+} \rightarrow [\mathrm{TiF_6}]^{2-} + 2\mathrm{H_2O} \quad (5)$$

In addition, fluoride ion is able to reduce TiO_2, making Ti (IV) convert to Ti (III) and creating oxygen vacancies [26].

$$\mathrm{Ti\ (IV)} \xrightarrow{\mathrm{F^-}} \mathrm{Ti\ (III)} + \mathrm{oxygen\ vacancies} \quad (6)$$

Due to the presence of H_2O_2, Ti (III) will be oxidized again [39].

$$\mathrm{Ti\ (III)} \xrightarrow{\mathrm{H_2O_2}} \mathrm{TiO_2} \quad (7)$$

Reaction (7) makes Ti (III) not present on the TiO_2.

4.3.3 Photocatalytic Performance

Table 2 shows the optical properties of TiO_2 samples. After H_2O_2 + NH_4F solution treatment, all TiO_2 samples show a significant color change, as shown in Figure 4.8(a), white TiO_2 nanoparticles turn yellow. The color change in TNF is apparent, followed by THF. PF has the lightest color. These color changes can be directly reflected in the UV-vis spectra, as shown in Figure 4.8(b), with the scanning range set from 190 nm to 1000 nm. The dotted lines represent the pretreatment sample, while solid lines represent the after-treatment sample. For TH and TN, after the modification, their absorption spectra shift towards the visible light direction, suggesting that these two samples are successfully modified for visible light photodegradation by the H_2O_2 +

NH_4F solution treatment. For P25, there is no obvious shift in the absorption spectrum. The indirect band gap of these TiO_2 samples can be determined by Tauc's plot transformed from UV-vis spectra, which is shown in Figure 4.8(c) [40, 41]. Compared to the pretreatment samples (shown as dotted lines), bandgaps of all three after-treatment samples shift towards the low energy area. TN has the largest decrease, followed by TH, and P25 is the smallest. Table 2 also shows the bandgap energy of these TiO_2 samples. TNF has the lowest bandgap energy, at around 2.2 eV. The next is THF, which bandgap is around 2.5 eV. The band gap of PF is 3.0 eV, only 0.1 eV lower than P25. In addition to the bandgaps mentioned above, PF and THF also show other bandgaps locating at 3.1 eV and 3.0 eV, respectively, which are the bandgaps of pretreatment samples P25 and TH. These results suggest that P25 and TH are not completely modified by H_2O_2 + NH_4F. In conclusion, after modification, these TiO_2 samples yield more effective under visible light.

Table 4.2. Optical properties of TiO_2 samples and the photodegradation kinetic constants.

Sample Name	Color	Bandgap (eV)	RhB kinetic constant (min^{-1})	MB kinetic constant (min^{-1})
P25	white	3.1	0.010	0.027
PF	light yellow	3.0	0.022	0.006
TH	white	3.0	0.027	0.006
THF	light yellow	2.5	0.043	0.048
TN	white	3.5	8.39×10^{-4}	
TNF	yellow	2.2	0.069	

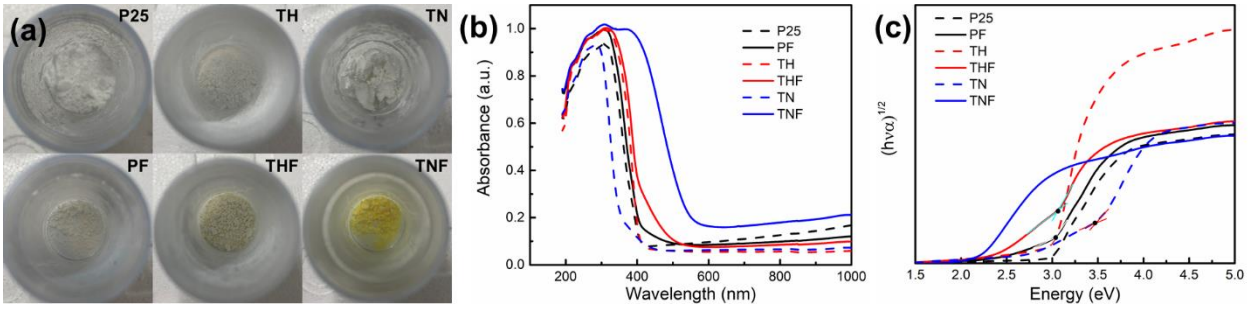

Figure 4.8. (a) Photograph of the TiO_2 samples; (b) UV-vis spectra of six TiO_2 samples; (c) Tauc's plot transformed by (b).

RhB and MB are chosen as the dye for the photodegradation ability test of the six samples to evaluate the improvement of photodegradation efficiency after the fluoride solution processing.

Figure 4.9(a) shows the results of the photodegradation tests of RhB, and Figure 4.9(b) shows the photodegradation kinetic calculated by the following equation [42].

$$c = c_0 \exp(-kt) \quad (8)$$

The results of the kinetic constants of TiO_2 samples for RhB photodegradation are shown in Table 2. In three pretreatment samples, TH has the highest photodegradation efficiency, whose kinetic constant is 0.027 min^{-1}, followed by P25 (0.010 min^{-1}), while TN is difficult for RhB photodegradation under visible light because of its high bandgap energy (3.5 eV), which is out of visible light range. The reason why TH works more efficient than P25 is presumably higher specific surface area. After modification, it can be clearly seen that the photodegradation efficiency of RhB by three groups of TiO_2 has been improved to varying degrees. The efficiency of group TN improves the most. After the treatment, TNF sample, whose kinetic constant reaches 0.069 min^{-1}, almost 7 times higher than that of P25, becomes the highest among all the TiO_2 samples. This is because of its high specific surface area (266.8 m^2/g) and low bandgap (2.2 eV). The photodegradation kinetic constant of THF increases to 0.043 min^{-1}, which reaches 4 times that of P25. This may be due to the phase transition (rutile to anatase) occurred during the modification [43]. The shift of bandgap caused by fluoride also suggests that THF has higher visible light activity [44, 45]. According to Figure 7(b), the photodegradation efficiency of THF decreased after 30 min, which may because of the decrease of specific surface area. The photodegradation kinetic constant of PF increases to 0.022 min^{-1}. This is also due to the increase of specific surface area and the decrease of bandgap energy [44, 45]. Since the increase of specific surface area and the decrease of energy bandgap are not significant, the efficiency improvement of photodegradation is not as significant as that of THF and TNF.

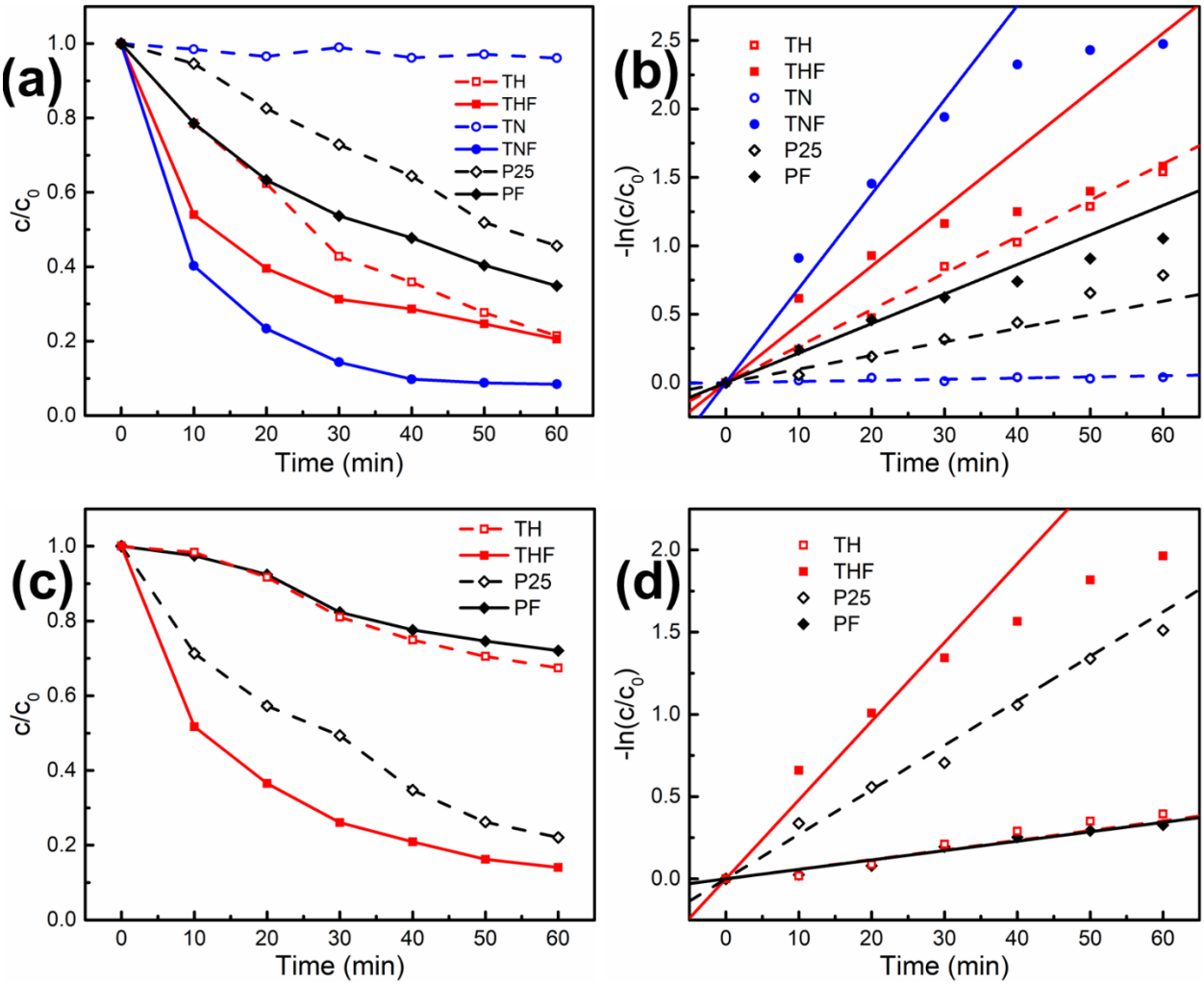

Figure 4.9. (a) Photodegradation curves of RhB by TiO_2 samples; (b) Photodegradation kinetic constant calculation of RhB by TiO_2 samples; (c) Photodegradation curves of MB by P25, PF, TH and THF; (d) Photodegradation kinetic constant calculation of MB by P25, PF, TH and THF.

Figure 4.9(c) shows the photodegradation tests of MB, while Figure 4.9(d) shows their photodegradation kinetic constants. Only four samples are mentioned in these two figures. The absorbance data of P25 used as the control group is based on the previous report [28]. TN and TNF will be discussed later. The visible light photodegradation kinetic constants of MB by different TiO_2 samples are shown in Table 2. Among these TiO_2 samples, THF shows the highest efficiency for the MB photodegradation, which is 0.048 min^{-1}. P25 also shows the high visible light photodegradation kinetic constant at 0.027 min^{-1}. Compared these two samples, the photodegradation kinetic constant of PF and TH (both 0.006 min^{-1}) are much lower, reducing the efficiency of visible light driven photodegradation. These results are highly possible to be caused

by structural changes due to the H_2O_2 + NH_4F modification. For MB photodegradation by TiO_2, the efficiency reaches the highest when the ratio of anatase and rutile is 4:1 [46, 47]. According to the XRD pattern in Figure 2, after the H_2O_2 + NH_4F modification, the proportion of anatase in TiO_2 sample increases, while the proportion of rutile decreases. TH is mainly rutile, so its photodegradation efficiency of MB is low. After modification, the proportion of anatase phase in THF increases, making the kinetic constant of MB photodegradation increases. However, the ratio of anatase and rutile for P25 has already been 4:1. Therefore, as the proportion of anatase increases, the photodegradation efficiency of PF decreases instead.

For TN and TNF, the efficiency of photodegradation under visible light cannot be determined because of their high adsorption rate. After 30 mins stirring even in dark condition, compared to P25, which adsorbed 11.3% of the MB, TN adsorbed 94.4% of the MB dyes, while TNF adsorbed 98.8% of the MB dyes, almost 9 times that of P25. Both solutions became colorless, which is quite effective, but unable to conduct the photodegradation kinetic constant. Since TN didn't show such high adsorption ability for RhB, it is possible for TN to have good selectivity for MB. This phenomenon is probably due to the differences between MB and RhB dyes. Although both MB and RhB are cationic dyes, MB has only positive group (-$N(Et)_2$), while RhB has both positive group and negative group (-COOH). The surface of TiO_2 nanoparticles is highly negatively charged, making it repel RhB, but has high adsorption of MB [48].

The results of recycle test are shown in Figure 4.10. RhB is taken as the dyes for the recycle dyes. Four of the TiO_2 samples (PF, TH, THF, and TNF) are tested for the cyclability. P25 is not considered as the control group, while TN is not good as a kind of photodegradation material. We set the dye degradation amount as 1 for the first time, and then plot the ratio of the degradation amount of the second and third time. According to the results, although fluctuating, all four samples show good cycle performance. Among them, sample PF and TH show the better cyclability, making their recycled photodegradation ratios float around 1. The cyclability of THF is worse, but during the third time, it remains over 70% photodegradation efficiency. In conclusion, all four TiO_2 samples have good recyclability.

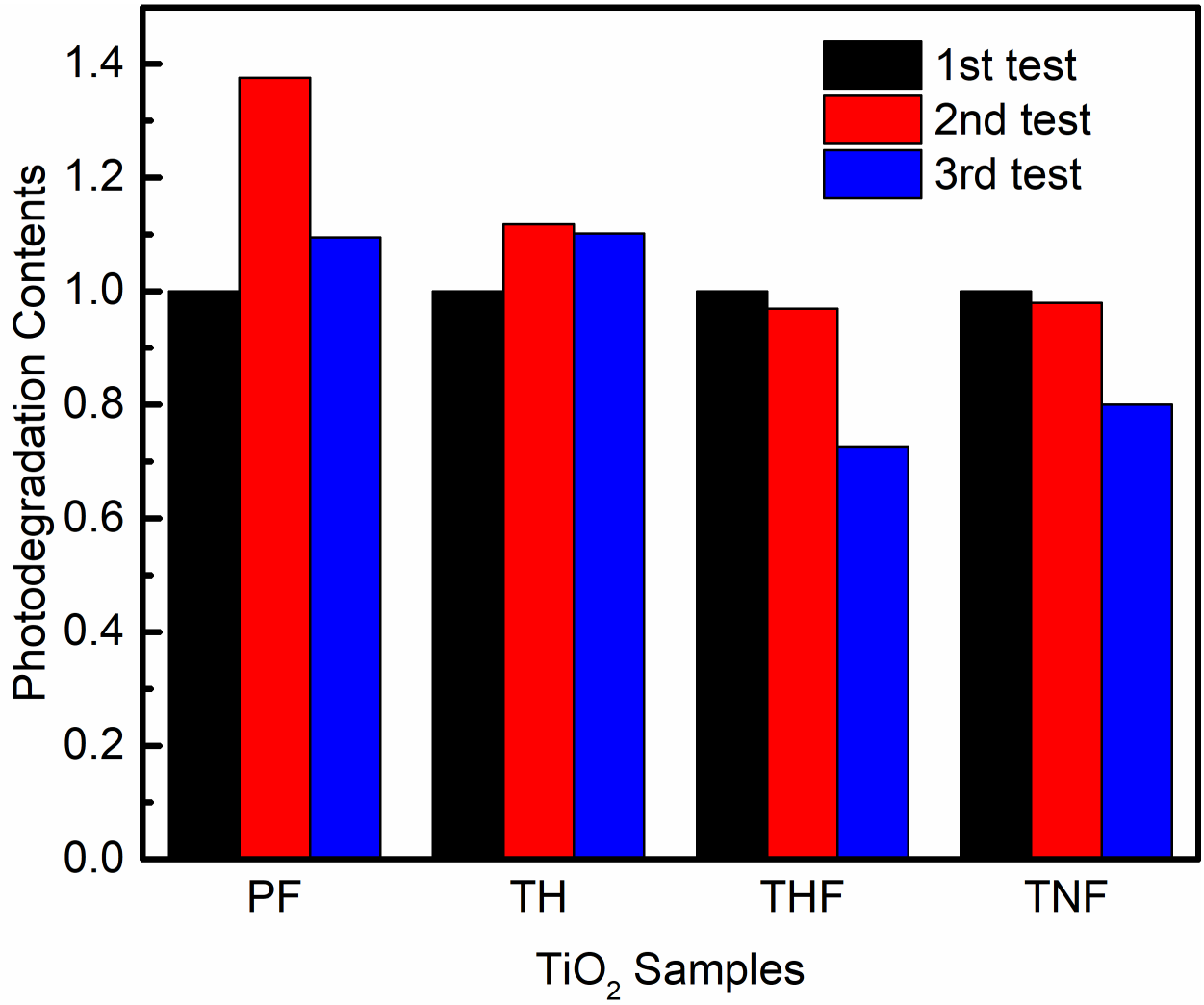

Figure 4.10. The cyclability test of sample PF, TH, THF, and TNF.

4.3.4 Photodegradation Mechanism

Figure 4.11 shows the absorbance spectra of RhB solution degraded by the six TiO_2 samples. Except for the groups degraded by P25 and TN, all the RhB solution degraded by the rest four samples turns to yellow, which is presented as the absorbance peak shifting to 500 nm. Based on the previous report, it is possible for RhB solution to turn yellow during the photodegradation process [49-51]. The electrons of TiO_2 can be excited by light and then create holes [52, 53].

$$TiO_2 + h\nu \rightarrow e^- + h_{vb}^+ \quad (9)$$

$$h_{vb}^+ \rightarrow h_{tr}^+ \quad (10)$$

In equation (9) and (10), h_{vb}^+ is the hole in the valence band state, and h_{tr}^+ is the trapped hole. In this experiment, TiO_2 samples absorb visible light to varying degrees, making the water molecule splitting, and releasing protons and hydroxyl radicals.

$$H_2O + h_{tr}^{+} \rightarrow H^{+} + \cdot OH \quad (11)$$

Hydroxyl radicals are active, which promotes the deethylation process of RhB molecule [54]. After that, the as-synthesized radicals would combine the protons (created by H_2O splitting) and electrons (excited from TiO_2 by light) and produce N, N-diethyl-N′-ethylrhodamine (DER)

$$C_{28}H_{31}ClN_2O_3(RhB) + \cdot OH \rightarrow \cdot C_{26}H_{26}ClN_2O_3 + C_2H_5OH \quad (12)$$

$$\cdot C_{26}H_{26}ClN_2O_3 + H^{+} + e^{-} \rightarrow C_{26}H_{27}ClN_2O_3\ (DER) \quad (13)$$

The same process applies for DER, which fabricates N, N-diethylrhodamine (DR) and N-ethyl-N'-ethylrhodamine (EER). Then the deethylation would continue and fabricate N-ethylrhodamine (ER) and rhodamine (R). These intermediate products make the solution become yellow before complete decomposition [49-51].

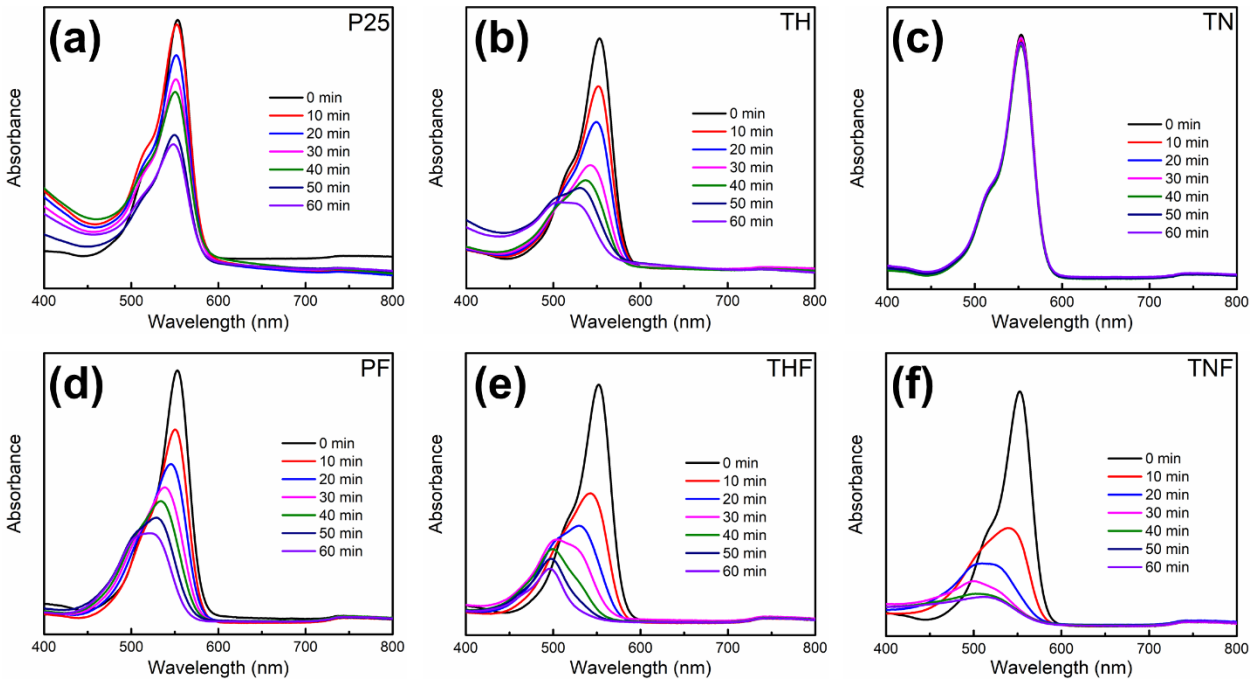

Figure 4.11. The UV-vis absorbance spectra of RhB photo-degraded by (a) P25 (b) TH (c) TN (d) PF (e) THF and (f) TNF.

According to Figure 4.11, the absorbance peak of P25 does not shift, suggesting that the photodegradation mechanism of P25 is different from other TiO_2 samples. The decomposition of conjugated structure caused by photosensitization of RhB, instead of deethylation, plays a very important role in RhB photodegradation by P25 [55, 56]. The range of visible light source we use is 400-600 nm, which contains the RhB light absorption peak. Although will be discussed elsewhere, TN does not show a very good photodegradation efficiency.

For MB photodegradation, according to Figure 4.12, the absorption peak of all four samples do not shift, suggesting the mechanisms are same. The hydroxyl radicals are believed to be able to photo-degrade MB [57]. Two mechanisms have been proposed to clarify the MB photodegradation by TiO_2 [58]. In these two mechanisms, N-demethylation would happen first because of the low bond energy of N-CH_3 bond (296.2 kJ/mol). C-S and C-N bonds can be oxidized and broken in the following oxidation, and finally decomposed to CO_2, H_2O, Cl^-, SO_4^{2-}, and NO_3^- [59]. In summary, Figure 4.13 schematically shows the photodegradation mechanisms under visible light for six TiO_2 samples.

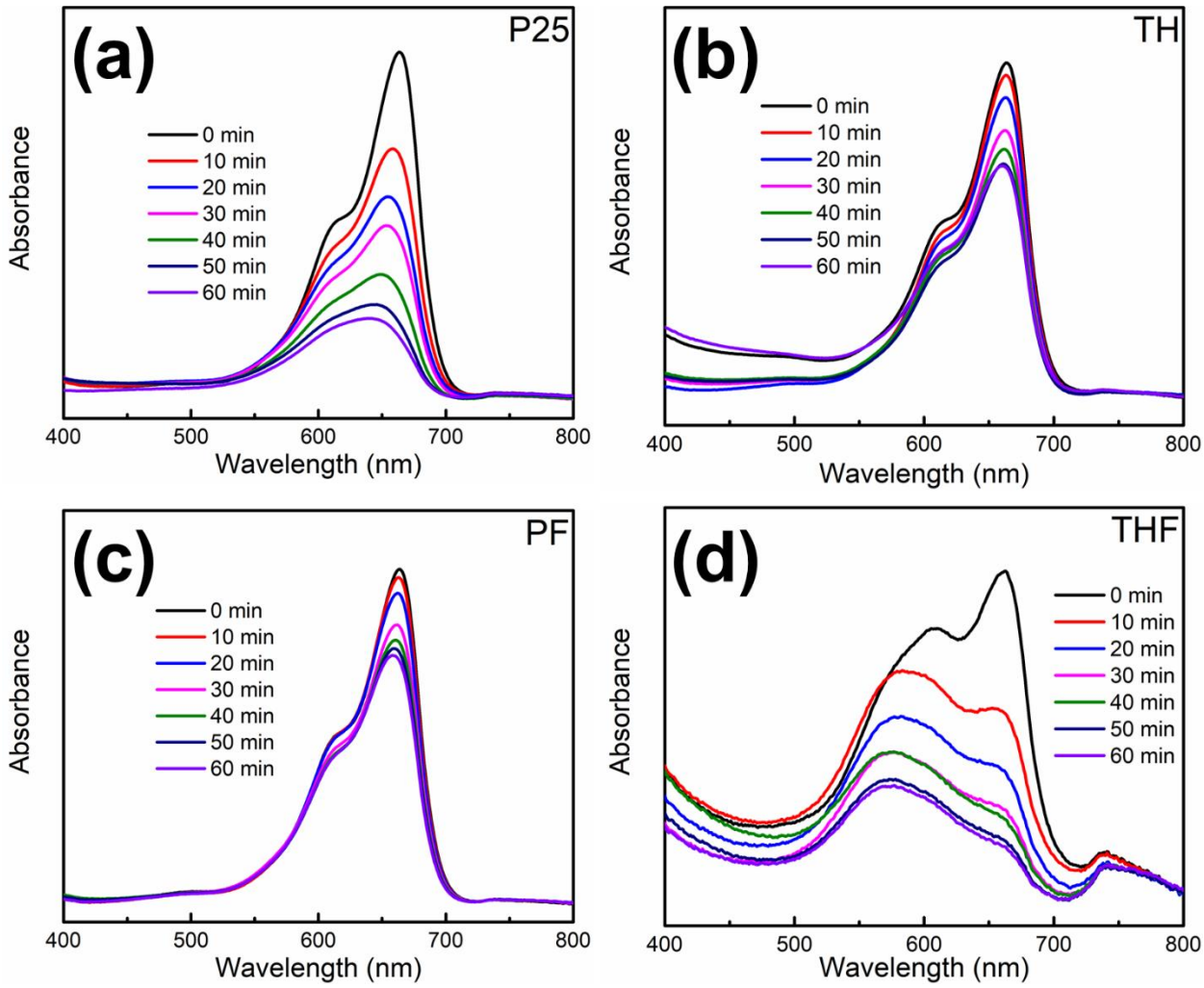

Figure 4.12. The UV-vis absorbance spectra of MB photo-degraded by (a) P25 (b) TH (c) PF and (d) THF.

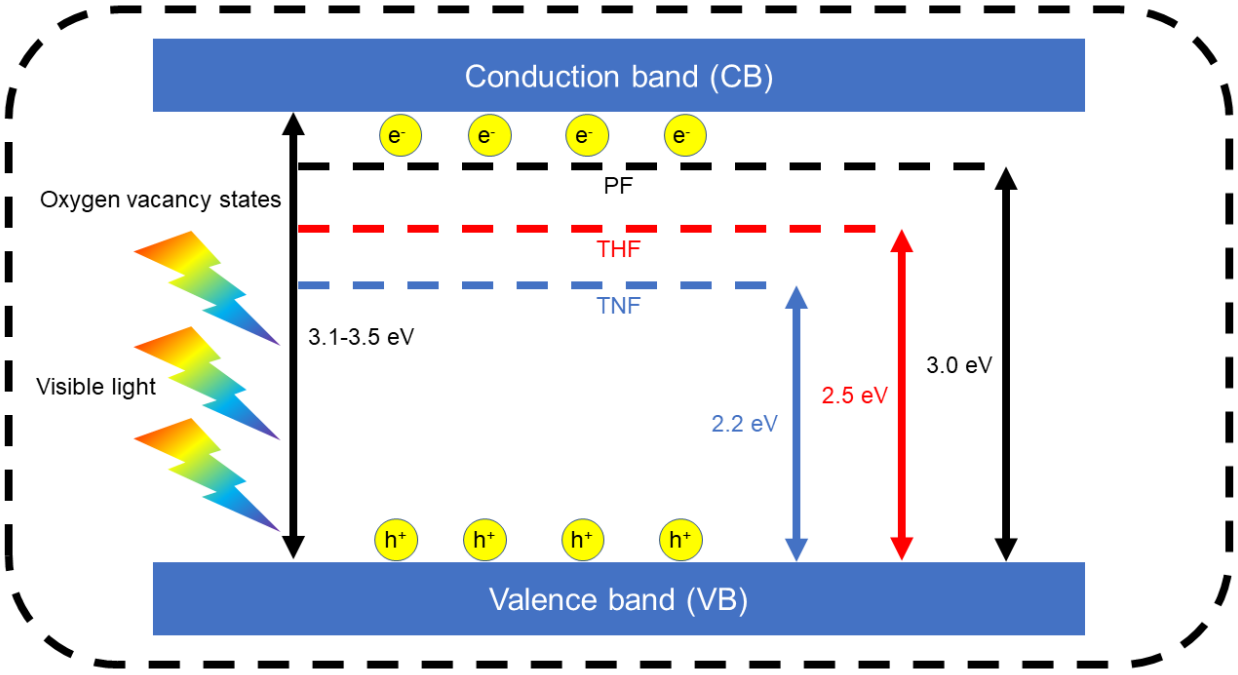

Figure 4.13. Schematics of photodegradation mechanism of TiO_2 samples under visible light.

4.4. Conclusion

In summary, we have successfully modified TiO_2 nanoparticles with H_2O_2 + NH_4F to enhance its visible light photo-driven activity. Compared to conventional methods, the present method is facile to obtain the modified TiO_2 samples of different structures from TTIP. The pH can affect the structure of TiO_2 hydrolyzed by TTIP, fabricating crystal TiO_2 under acidic conditions, and amorphous TiO_2 under alkaline conditions. The modification method is also easy to access by only requiring H_2O_2, NH_4F and 80°C temperature. P25, PF, TH and THF are crystal, while TN and TNF are amorphous. The modification would increase the transformation from rutile to anatase (for crystal TiO_2 samples) and amorphization (for amorphous TiO_2 samples). Furthermore, this facile modification method is proved to be effective on the increasement of visible light photodegradation efficiency by reducing their bandgap, especially for RhB. The photodegradation kinetic constant of TNF can reach almost 7 times that of P25, which is the highest among all the TiO_2 samples. THF has the highest visible light photodegradation kinetic constant for MB, which is about 1.8 times that of P25. Finally, TN and TNF show very high MB dye adsorption, almost 9 times that of P25. Therefore, the present work provides a facile new route for the modification of TiO_2 and gives a unique performance improvement.

References

1. Gusain, R., et al., *Adsorptive removal and photocatalytic degradation of organic pollutants using metal oxides and their composites: A comprehensive review.* Advances in Colloid and Interface Science, 2019. **272**: p. 102009.

2. Gupta, S.M. and M. Tripathi, *A review of TiO_2 nanoparticles.* Chinese Science Bulletin, 2011. **56**(16): p. 1639.

3. Chen, X. and S.S. Mao, *Titanium Dioxide Nanomaterials: Synthesis, Properties, Modifications, and Applications.* Chemical Reviews, 2007. **107**(7): p. 2891-2959.

4. Ohtani, B., et al., *What is Degussa (Evonik) P25? Crystalline composition analysis, reconstruction from isolated pure particles and photocatalytic activity test.* Journal of Photochemistry and Photobiology A: Chemistry, 2010. **216**(2): p. 179-182.

5. Bessergenev, V.G., et al., *An improvement of photocatalytic activity of TiO_2 Degussa P25 powder.* Applied Catalysis A: General, 2015. **500**: p. 40-50.

6. Humayun, M., et al., *Modification strategies of TiO_2 for potential applications in photocatalysis: A critical review.* Green Chemistry Letters and Reviews, 2018. **11**(2): p. 86-102.

7. Dharma, H.N., et al., *A Review of Titanium Dioxide (TiO_2)-Based Photocatalyst for Oilfield-Produced Water Treatment.* Membranes, 2022. **12**(3).

8. Ma, J., et al., *Preparation of nanocrystalline Fe-doped TiO_2 powders as a visible-light-responsive photocatalyst.* Research on Chemical Intermediates, 2009. **35**(3): p. 329-336.

9. Laokiat, L., et al., *Photocatalytic degradation of benzene, toluene, ethylbenzene, and xylene (BTEX) using transition metal-doped titanium dioxide immobilized on fiberglass cloth.* Korean Journal of Chemical Engineering, 2012. **29**(3): p. 377-383.

10. Binas, V., et al., *Photocatalytic oxidation of gaseous benzene, toluene and xylene under UV and visible irradiation over Mn-doped TiO_2 nanoparticles.* Journal of Materiomics, 2019. **5**(1): p. 56-65.

11. Wang, J., et al., *Preparation, structural and photocatalytic activity of Sn/Fe co-doped TiO_2 nanoparticles by sol-gel method.* Ceramics International, 2022. **48**(6): p. 8297-8305.

12. Li, X., et al., *Visible light-driven photocatalysis of W, N co-doped TiO_2.* Particuology, 2013. **11**(6): p. 732-736.

13. Chen, Q., et al., *Visible-light-activated Ce–Si co-doped TiO_2 photocatalyst.* Applied Surface Science, 2009. **255**(18): p. 7918-7924.

14. Islam, S.Z., et al., *Synthesis and Catalytic Applications of Non-Metal Doped Mesoporous Titania.* Inorganics, 2017. **5**(1).

15. Lin, X., et al., *Carbon-doped mesoporous TiO_2 film and its photocatalytic activity.* Microporous and Mesoporous Materials, 2011. **142**(1): p. 276-281.

16. Chang, P.-y., C.-h. Huang, and R.-a. Doong, *Ordered mesoporous carbon– TiO_2 materials for improved electrochemical performance of lithium ion battery.* Carbon, 2012. **50**(11): p. 4259-4268.

17. Liu, G., et al., *Visible Light Photocatalyst: Iodine-Doped Mesoporous Titania with a Bicrystalline Framework.* The Journal of Physical Chemistry B, 2006. **110**(42): p. 20823-20828.

18. Yu, J.C., et al., *Synthesis and Characterization of Phosphated Mesoporous Titanium Dioxide with High Photocatalytic Activity.* Chemistry of Materials, 2003. **15**(11): p. 2280-2286.

19. Zaleska, A., et al., *Preparation and photocatalytic activity of boron-modified TiO_2 under UV and visible light.* Applied Catalysis B: Environmental, 2008. **78**(1): p. 92-100.

20. Mabilleau, G., et al., *Influence of fluoride, hydrogen peroxide and lactic acid on the corrosion resistance of commercially pure titanium.* Acta Biomaterialia, 2006. **2**(1): p. 121-129.

21. Hanaor, D.A.H., et al., *Ab initio study of phase stability in doped TiO_2.* Computational Mechanics, 2012. **50**(2): p. 185-194.

22. Hanaor, D.A.H. and C.C. Sorrell, *Review of the anatase to rutile phase transformation.* Journal of Materials Science, 2011. **46**(4): p. 855-874.

23. Yoo, J.-H. and S.-W. Cho, *Solubility of TiO_2 in NaF-CaF_2-BaF_2 Melts.* Metals and Materials International, 2018. **24**(6): p. 1386-1393.

24. Yan, W., et al., *Synergistic effect of sodium ions and fluoride ions on synthesis of pure-phase TiO_2(B) nanorings.* Journal of Nanoparticle Research, 2017. **19**(6): p. 192.

25. Yu, Y., et al., *Preparation, Characterization and Photocatalytic Activities of F^- doped TiO_2 Nanotubes.* Catalysis Letters, 2008. **121**(1): p. 165-171.

26. Yu, J.C., et al., *Effects of F^- Doping on the Photocatalytic Activity and Microstructures of Nanocrystalline TiO_2 Powders.* Chemistry of Materials, 2002. **14**(9): p. 3808-3816.

27. Zou, J. and J. Gao, *H_2O_2-sensitized TiO_2/SiO_2 composites with high photocatalytic activity under visible irradiation.* Journal of Hazardous Materials, 2011. **185**(2): p. 710-716.

28. Yu, Z., et al., *Mesoporous single crystal titanium oxide microparticles for enhanced visible light photodegradation.* Optical Materials, 2022. **127**: p. 112297.

29. Zhang, Y., et al., *Thermochemistry of glasses along the $2NdAlO_3$–$3SiO_2$ join.* Journal of Physics: Condensed Matter, 2003. **15**(31): p. S2343-S2355.
30. Kuznetsov, M.V., J.F. Zhuravlev, and V.A. Gubanov, *XPS analysis of adsorption of oxygen molecules on the surface of Ti and TiN_x films in vacuum.* Journal of Electron Spectroscopy and Related Phenomena, 1992. **58**(3): p. 169-176.
31. Chan, C.M., S. Trigwell, and T. Duerig, *Oxidation of an NiTi alloy.* Surface and Interface Analysis, 1990. **15**(6): p. 349-354.
32. Liu, X., W. Chen, and W. Wang, *F^- Serve as Surface Trapping Sites to Promote the Charge Separation and Transfer of TiO_2.* ACS Omega, 2021. **6**(51): p. 35799-35809.
33. Byun, M.Y., et al., *Effect of surface properties of TiO_2 on the performance of Pt/ TiO_2 catalysts for furfural hydrogenation.* RSC Advances, 2022. **12**(2): p. 860-868.
34. Yang, Y., et al., *Deciphering chemical order/disorder and material properties at the single-atom level.* Nature, 2017. **542**(7639): p. 75-79.
35. Nussbaumer, H.J., *The Fast Fourier Transform*, in *Fast Fourier Transform and Convolution Algorithms*, H.J. Nussbaumer, Editor. 1981, Springer Berlin Heidelberg: Berlin, Heidelberg. p. 80-111.
36. Song, K.C. and S.E. Pratsinis, *Control of Phase and Pore Structure of Titania Powders Using HCl and NH_4OH Catalysts.* Journal of the American Ceramic Society, 2001. **84**(1): p. 92-98.
37. McNicoll, C., T. Kemmitt, and V. Golovko, *Hydrothermal rutile to anatase reverse phase transformation.* International Journal of Nanotechnology, 2014. **11**(5-678): p. 493-501.
38. Wang, X., et al., *Fluoride concentration controlled TiO_2 nanotubes: the interplay of microstructure and photocatalytic performance.* RSC Advances, 2016. **6**(22): p. 18333-18339.
39. Furiya-Sato, S., et al., *Electrochemical evaluation of the hydrogen peroxide- and fluoride-induced corrosive property and its recovery on the titanium surface.* Journal of Prosthodontic Research, 2020. **64**(3): p. 307-312.
40. Makuła, P., M. Pacia, and W. Macyk, *How To Correctly Determine the Band Gap Energy of Modified Semiconductor Photocatalysts Based on UV–Vis Spectra.* The Journal of Physical Chemistry Letters, 2018. **9**(23): p. 6814-6817.
41. Suram, S.K., P.F. Newhouse, and J.M. Gregoire, *High Throughput Light Absorber Discovery, Part 1: An Algorithm for Automated Tauc Analysis.* ACS Combinatorial Science, 2016. **18**(11): p. 673-681.

42. Gómez, M., et al., *Modelling and experimental checking of the influence of substrate concentration on the first order kinetic constant in photo-processes.* Journal of Environmental Management, 2016. **183**: p. 818-825.

43. Luttrell, T., et al., *Why is anatase a better photocatalyst than rutile? - Model studies on epitaxial TiO_2 films.* Scientific Reports, 2014. **4**(1): p. 4043.

44. Feng, N., et al., *Unravelling the Efficient Photocatalytic Activity of Boron-induced Ti^{3+} Species in the Surface Layer of TiO_2.* Scientific Reports, 2016. **6**(1): p. 34765.

45. Xu, J., et al., *Facile and Large-scale Synthesis of Defective Black TiO_{2-x}(B) Nanosheets for Efficient Visible-light-driven Photocatalytic Hydrogen Evolution.* Catalysts, 2019. **9**(12).

46. Tichapondwa, S.M., J.P. Newman, and O. Kubheka, *Effect of TiO_2 phase on the photocatalytic degradation of methylene blue dye.* Physics and Chemistry of the Earth, Parts A/B/C, 2020. **118-119**: p. 102900.

47. Zaw, Y.Y., et al., *Effect of Anatase/Rutile Phase Ratio on the Photodegradation of Methylene Blue under UV Irradiation.* Materials Science Forum, 2020. **998**: p. 78-83.

48. Natarajan, T.S., H.C. Bajaj, and R.J. Tayade, *Preferential adsorption behavior of methylene blue dye onto surface hydroxyl group enriched TiO_2 nanotube and its photocatalytic regeneration.* Journal of Colloid and Interface Science, 2014. **433**: p. 104-114.

49. Cui, Y., et al., *Effect of Dual-Cocatalyst Surface Modification on Photodegradation Activity, Pathway, and Mechanisms with Highly Efficient Ag/$BaTiO_3$/MnO_x.* Langmuir, 2020. **36**(2): p. 498-509.

50. Watanabe, T., T. Takizawa, and K. Honda, *Photocatalysis through excitation of adsorbates. 1. Highly efficient N-deethylation of rhodamine B adsorbed to cadmium sulfide.* The Journal of Physical Chemistry, 1977. **81**(19): p. 1845-1851.

51. Hu, X., et al., *Oxidative Decomposition of Rhodamine B Dye in the Presence of VO^{2+} and/or Pt(IV) under Visible Light Irradiation: N-Deethylation, Chromophore Cleavage, and Mineralization.* The Journal of Physical Chemistry B, 2006. **110**(51): p. 26012-26018.

52. Fujishima, A. and K. Honda, *Electrochemical Photolysis of Water at a Semiconductor Electrode.* Nature, 1972. **238**(5358): p. 37-38.

53. Hirakawa, T. and Y. Nosaka, *Properties of $O_2^{\bullet-}$ and OH• Formed in TiO_2 Aqueous Suspensions by Photocatalytic Reaction and the Influence of H_2O_2 and Some Ions.* Langmuir, 2002. **18**(8): p. 3247-3254.

54. Liang, L., et al., *Efficiency and mechanisms of rhodamine B degradation in Fenton-like systems based on zero-valent iron.* RSC Advances, 2020. **10**(48): p. 28509-28515.
55. Ma, Y. and J.-n. Yao, *Photodegradation of Rhodamine B catalyzed by TiO_2 thin films.* Journal of Photochemistry and Photobiology A: Chemistry, 1998. **116**(2): p. 167-170.
56. Wu, J.-M. and T.-W. Zhang, *Photodegradation of rhodamine B in water assisted by titania films prepared through a novel procedure.* Journal of Photochemistry and Photobiology A: Chemistry, 2004. **162**(1): p. 171-177.
57. Zou, J., J. Gao, and F. Xie, *An amorphous TiO_2 sol sensitized with H_2O_2 with the enhancement of photocatalytic activity.* Journal of Alloys and Compounds, 2010. **497**(1): p. 420-427.
58. Lv, H., et al., *A brief introduction to the fabrication and synthesis of graphene based composites for the realization of electromagnetic absorbing materials.* Journal of Materials Chemistry C, 2017. **5**(3): p. 491-512.
59. Wang, Q., S. Tian, and P. Ning, *Degradation Mechanism of Methylene Blue in a Heterogeneous Fenton-like Reaction Catalyzed by Ferrocene.* Industrial & Engineering Chemistry Research, 2014. **53**(2): p. 643-649.

Chapter 5

Summary

5.1 General Conclusions

The research target of this dissertation is the design and modification of Ti oxide materials, for the high photoactivity under visible light condition. In order to achieve this goal, three different kind of TiO_2 particles (b-TiO_2, EC-SPSC TiO_2, e-TiO_2) are fabricated by different methods, while two of them are homogenous and worthy of further research for the visible light photocatalyst. In addition to the newly formed TiO_2, one facile method is used for the modification of common TiO_2 in the market. This method is proved to be effective for the visible light photodegradation of common dyes. Furthermore, an attempt to the synthesize of TiO_2-related heterojunction is made. Green TiO_2/WO_3 and red $TiO_2/WO_3/MnO_x$ are successfully fabricated and proved to have higher absorption of visible light compared to origin TiO_2.

In chapter 2, two different methods are used for the fabrication of TiO_2 for the enhancement of the visible light activity. In this work, a one-step SPP method is proposed to fabricate b-TiO_2, which is a superior photo material with high solar absorption property. In addition, EC-SPSC method is used for the attempting of TiO_2 fabrication. A two-step mechanism for the formation of b-TiO_2 is proposed. At first, the formation of black TiO_{2-x} layer is caused by the Ti electrode surface pre-oxidation. After that, the electrode surface melted by Joule heating in plasma, then sputtered molten TiO_x clusters quenches by electrolyte and aggregates to form b-TiO_2 particles. In these steps, the pre-oxidized TiO_{2-x} layer is found to be necessary for the b-TiO_2 formation by SPP method. The b-TiO_2 is proved to be effective on the generation of water vapor under solar light irradiation. As a result, it is easily upscaled and used in clean, facile production of solar harvesting materials. As for TiO_2 fabrication by EC-SPSC method, although it has been proved that TiO_2 can be fabricated by this method, the low-repeatability and bad-homogeneity prevent the further research. As a result, we do not recommend using the EC-SPSC method for the fabrication of TiO_2 nanoparticles.

In chapter 3, e-TiO_2 is successfully fabricated by a facile method. Compared to conventional methods, this method only requires raw Ti, H_2O_2, NH_4F, at temperature of 80°C and atmospheric pressure. These requirements are easy to achieve compared to other methods using Ti plate as a raw material, making this method facile. The e-TiO_2 itself also has many advantages compared to commercial P25. Because of the effects of fluoride ions and H_2O_2, e-TiO_2 MPs are one kind of

single crystal micromaterials, containing mesopores generated by oxygen vacancies and Ti (III) component. These modifications would lead to superior performances, such as high adsorption for dyes. Furthermore, e-TiO_2 has been proved to have much better photodegradation efficiency. When degrade RhB under visible light, the photodegradation kinetic constant of e-TiO_2 could be 4 times as much as P25. Therefore, the present work provides a facile route to fabricate single crystal TiO_2 with mesoporous structure for high efficiency visible light dye photodegradation.

In chapter 4, the facile method for the fabrication of e-TiO_2 is used for the modification of common TiO_2 nanomaterials to enhance the visible light photo-driven activity. Compared to conventional methods, the present method is facile to obtain the modified TiO_2 samples of different structures from TTIP. The pH can affect the structure of TiO_2 hydrolyzed by TTIP, fabricating crystal TiO_2 under acidic conditions, and amorphous TiO_2 under alkaline conditions. The modification method is also easy to access by only requiring H_2O_2, NH_4F and 80°C temperature. P25, PF, TH and THF are crystal, while TN and TNF are amorphous. The modification would increase the transformation from rutile to anatase (for crystal TiO_2 samples) and amorphization (for amorphous TiO_2 samples). Furthermore, this facile modification method is proved to be effective on the increasement of visible light photodegradation efficiency by reducing their bandgap, especially for RhB. The photodegradation kinetic constant of TNF can reach almost 7 times that of P25, which is the highest among all the TiO_2 samples. THF has the highest visible light photodegradation kinetic constant for MB, which is about 1.8 times that of P25. Finally, TN and TNF show very high MB dye adsorption, almost 9 times that of P25. Therefore, the present work provides a facile new route for the modification of TiO_2 and gives a unique performance improvement.

5.2 Future Prospects

5.2.1 General Introduction

Although b-TiO_2, e-TiO_2 and modified TiO_2 have been proved to be effective to visible light, there are still some other methods to enhance the properties of TiO_2 materials. Doping is an effective way to broaden the absorption wavelength of light of a certain metal oxide [1]. Tungsten trioxide is one of the potential doping material for TiO_2, which is sensitive to the visible light. Fujii et al. have proposed a facile method to fabricate WO_3 by H_2O_2 and tungsten metal [2]. Based on this research, we have successfully fabricated W-doped TiO_2 and W/Mn doped TiO_2.

5.2.2 Experimental methods

Tungsten solution was prepared for the fabrication of doped TiO_2 materials. 0.5 g of tungsten metal (Nilaco Cooperation, Japan) were cleaned in acetone, ethanol, and distilled water under ultrasonication for 15 mins each. 10 wt% of H_2O_2 solution was diluted by H_2O_2 solution (30 wt%, Kanto Chemical Co., inc.) as the solvent. Then 0.5 g of W metal was dropped into 20 mL 10 wt% H_2O_2 solution and illuminated by a UV lamp (λ = 365 nm) for 24 hours. Clear solution was collected for the further fabrication.

TTIP solution ($[(CH_3)_2CHO]_4Ti$, Wako Pure Chemical Cooperation, 95%) was used as the Ti source of the doped material. 0.1 mL of TTIP solution was added into the 20 mL clear solution, then put under the same UV lamp for other 72 hours with stirring (~ 300 rpm). The suspension was then centrifuged to get the product. The product was cleaned three times and dried in 50°C. In addition, to get the Mn-doped material, 0.2 g of the Manganese flake (Mn, KANTO CHEMICAL CO., INC) was added in W solution after the TTIP, keeping other procedures same. All the chemicals were used as received without purification.

5.2.3 The Characterization of W-doped TiO_2 and W/Mn co-doped TiO_2

Figure 5.1 shows the SEM image of W-doped TiO_2. Figure 5.2 shows the XPS spectra of W-doped TiO_2. Peaks appear in all three regions (Ti 2p, W 4f, O1s), suggesting that all W has successfully doped on the Ti surface.

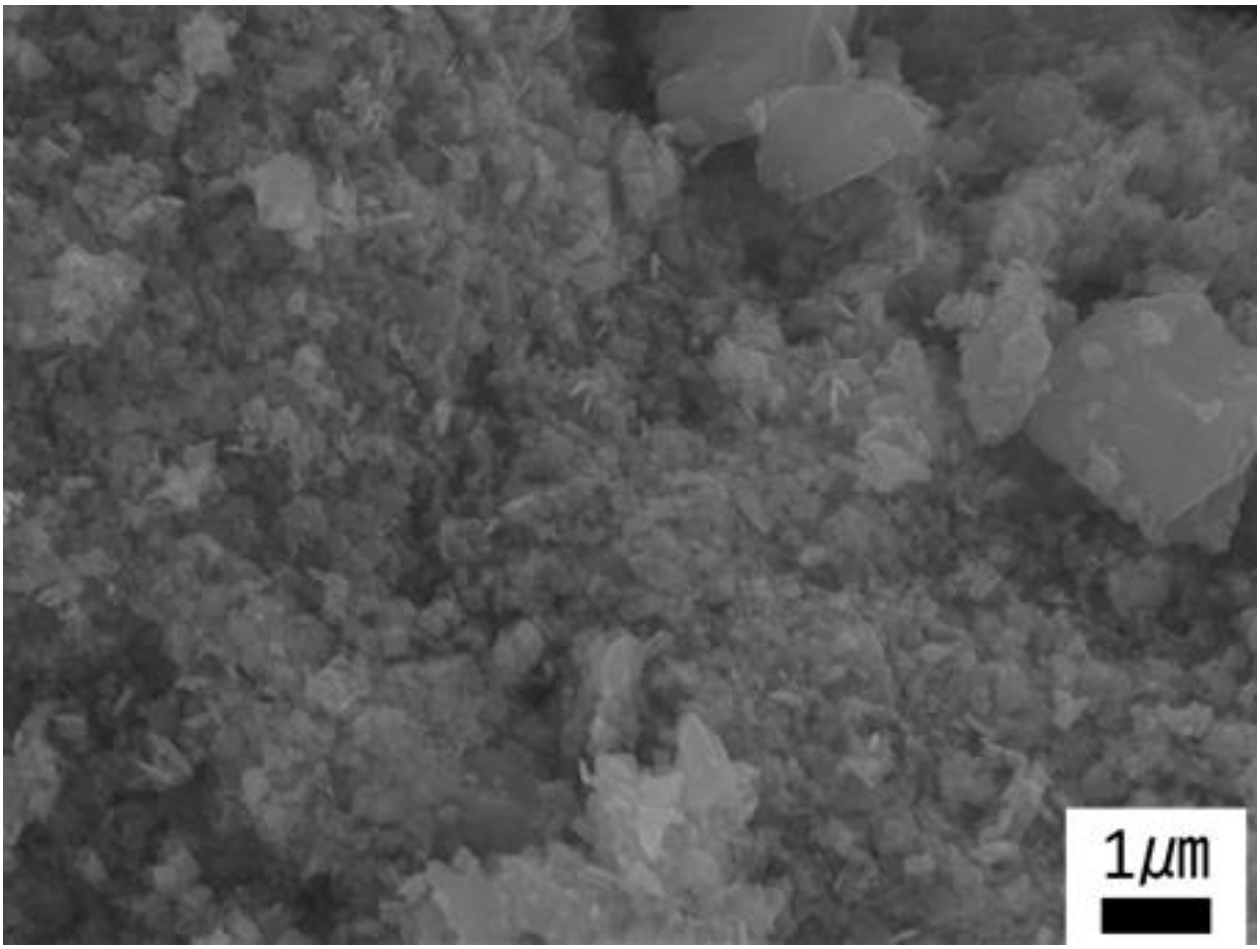

Figure 5.1. SEM image of W-doped TiO_2.

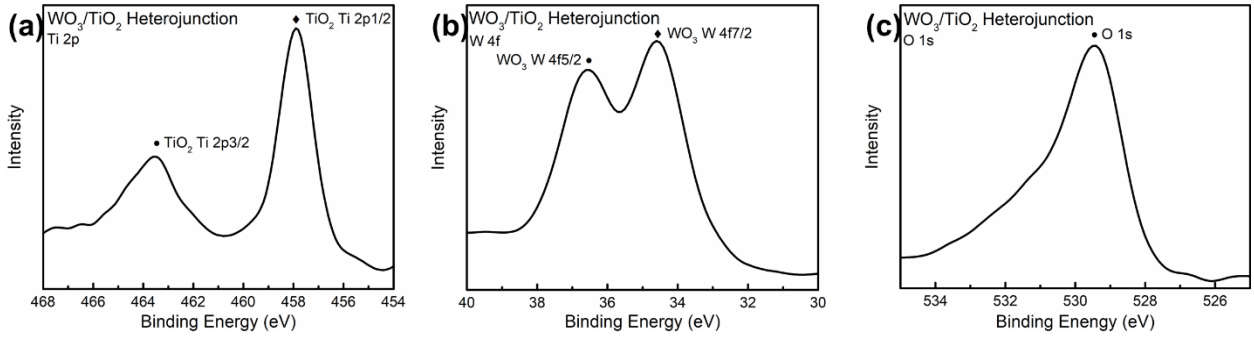

Figure 5.2 XPS spectra of (a) Ti 2p range (b) W 4f range (c) O 1s range of W-doped TiO_2.

The HRTEM images of W-doped TiO_2 are shown in Figure 5.3. The plate WO_3 structure can be seen clearly in the figure, surrounded by TiO_2. Figure 5.3(b) and (c) shows the detailed structure of WO_3 and TiO_2, respectively. According to the SAED result, WO_3 may be a single crystal structure, while TiO_2 is amorphous.

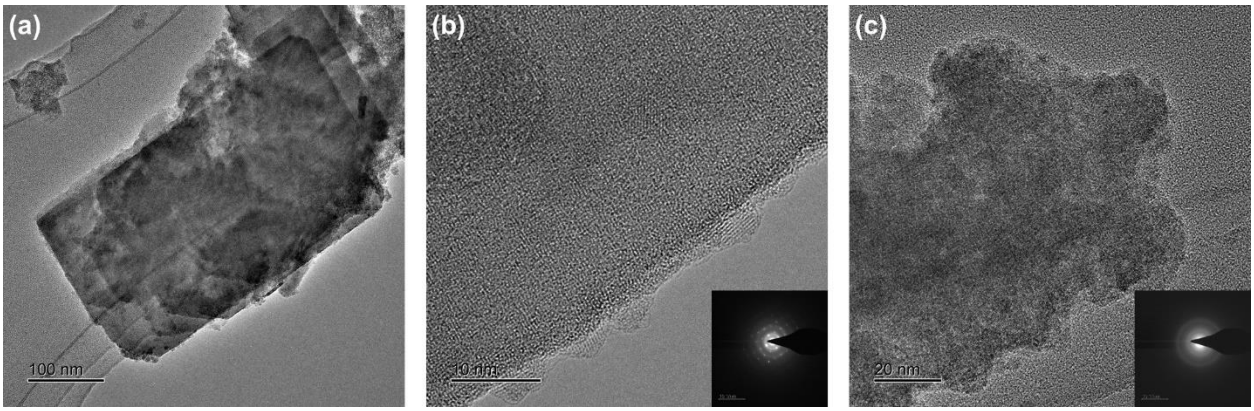

Figure 5.3. HRTEM images of (a) W doped TiO_2 (b) WO_3 with SAED (c) TiO_2 with SAED.

Figure 5.4 shows the SEM images of W/Mn doped TiO_2 with the EDS results. Compared to Figure 5.1, long strip substances appear, which is probably Mn oxides. The EDS dotting map shows that all three metal elements appear at the same point, suggesting that Mn participates in the reaction and form oxides.

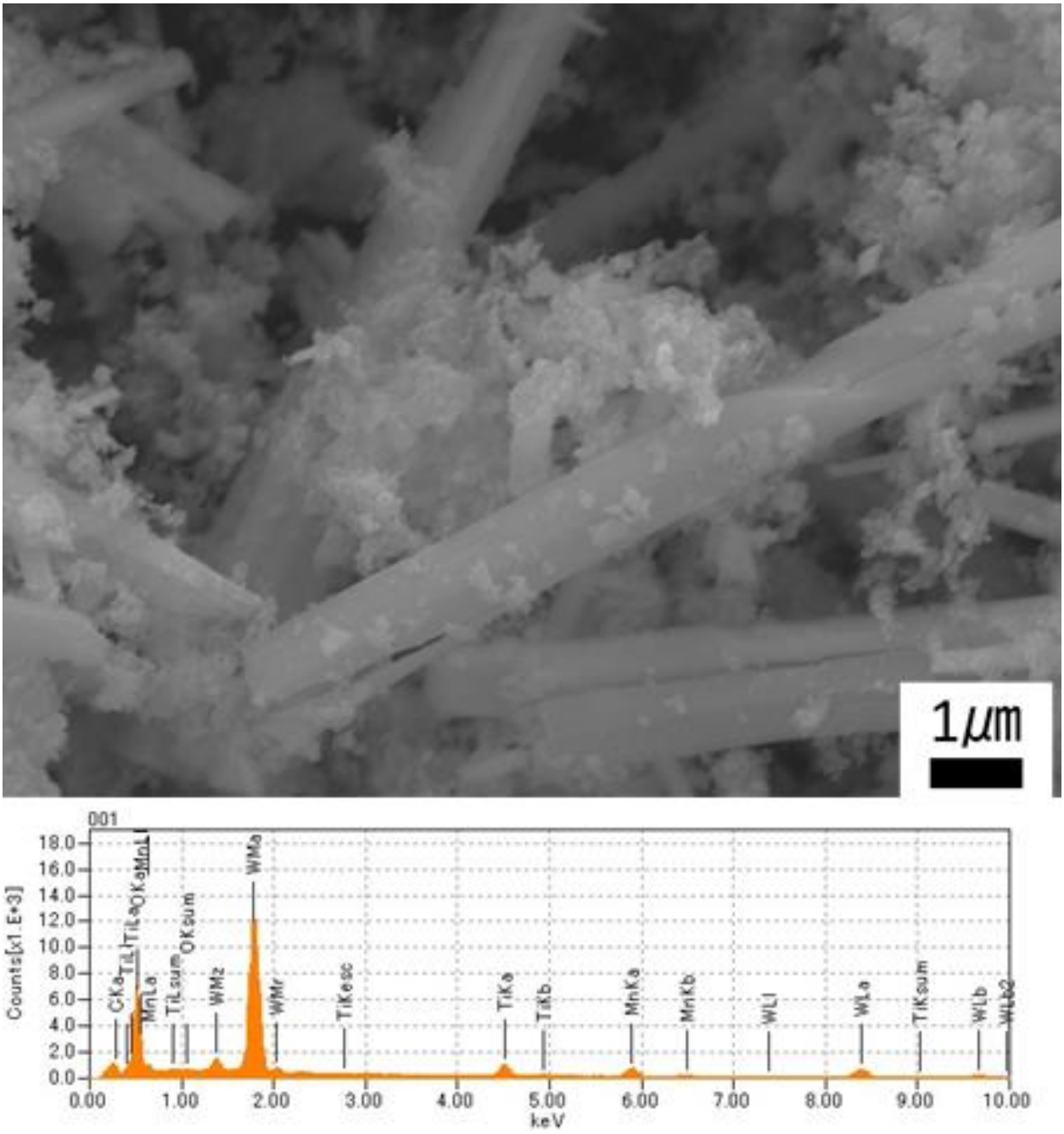

Figure 5.4. SEM image of W/Mn-doped TiO_2 with EDS analysis data.

Figure 5.5 shows the sample images of W-doped TiO_2 and W/Mn doped TiO_2. The original TiO_2 is white, while original WO_3 is yellow. The color of the doped TiO_2 changes. W-doped TiO_2 is green, while W/Mn doped TiO_2 is brown. The changes of color harbingers the changes of bandgap. Figure 5.6 shows the UV-vis spectra of W-doped TiO_2 and W/Mn doped TiO_2, together with the data of TiO_2 and WO_3 as control groups. Whether it is W-doped TiO_2 or W/Mn doped TiO_2, the absorption of visible light is stronger than that of the two control groups.

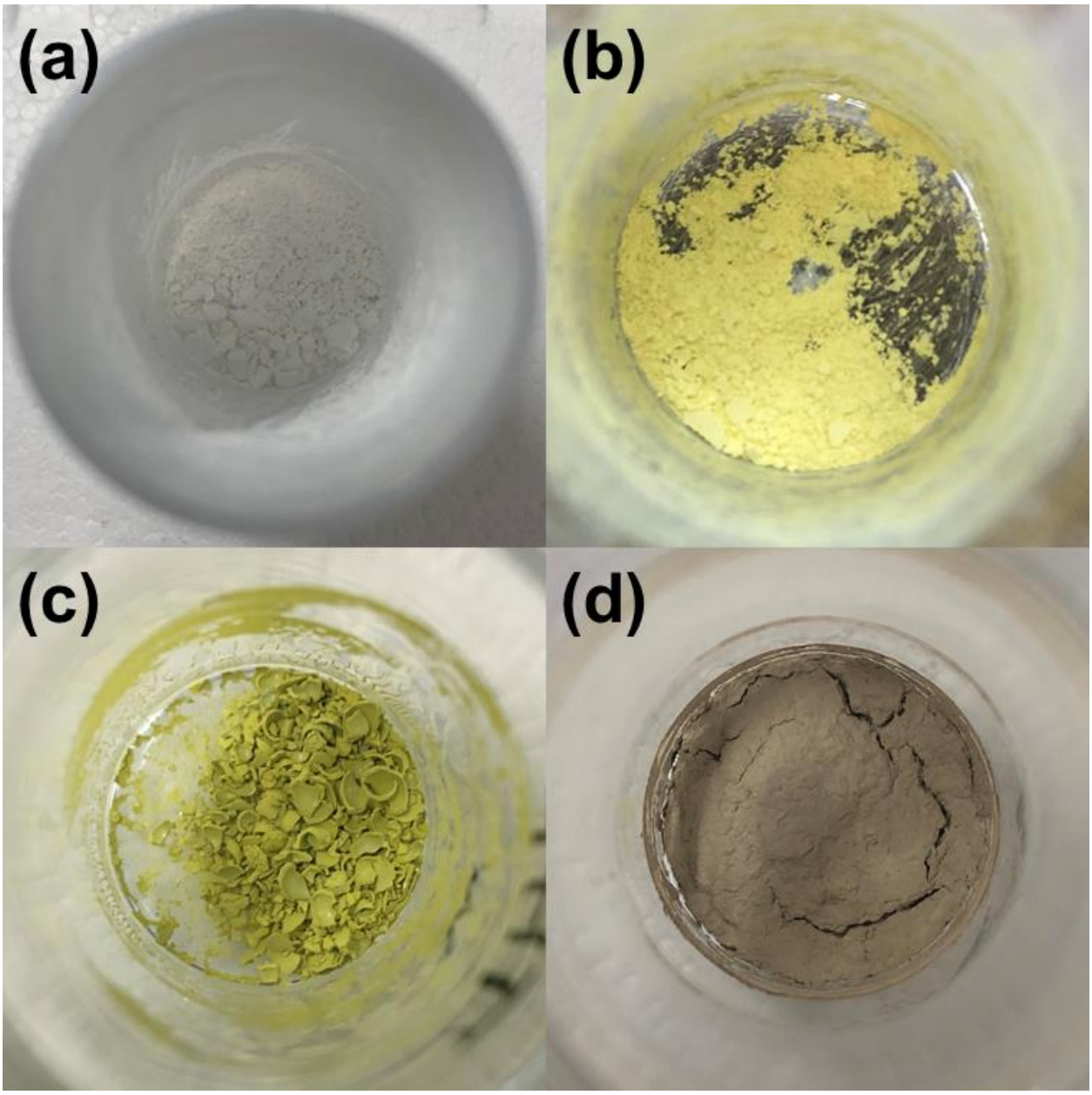

Figure 5.5. Sample image of (a) TiO_2 (b) WO_3 (c) W-doped TiO_2 (d) W/Mn doped TiO_2.

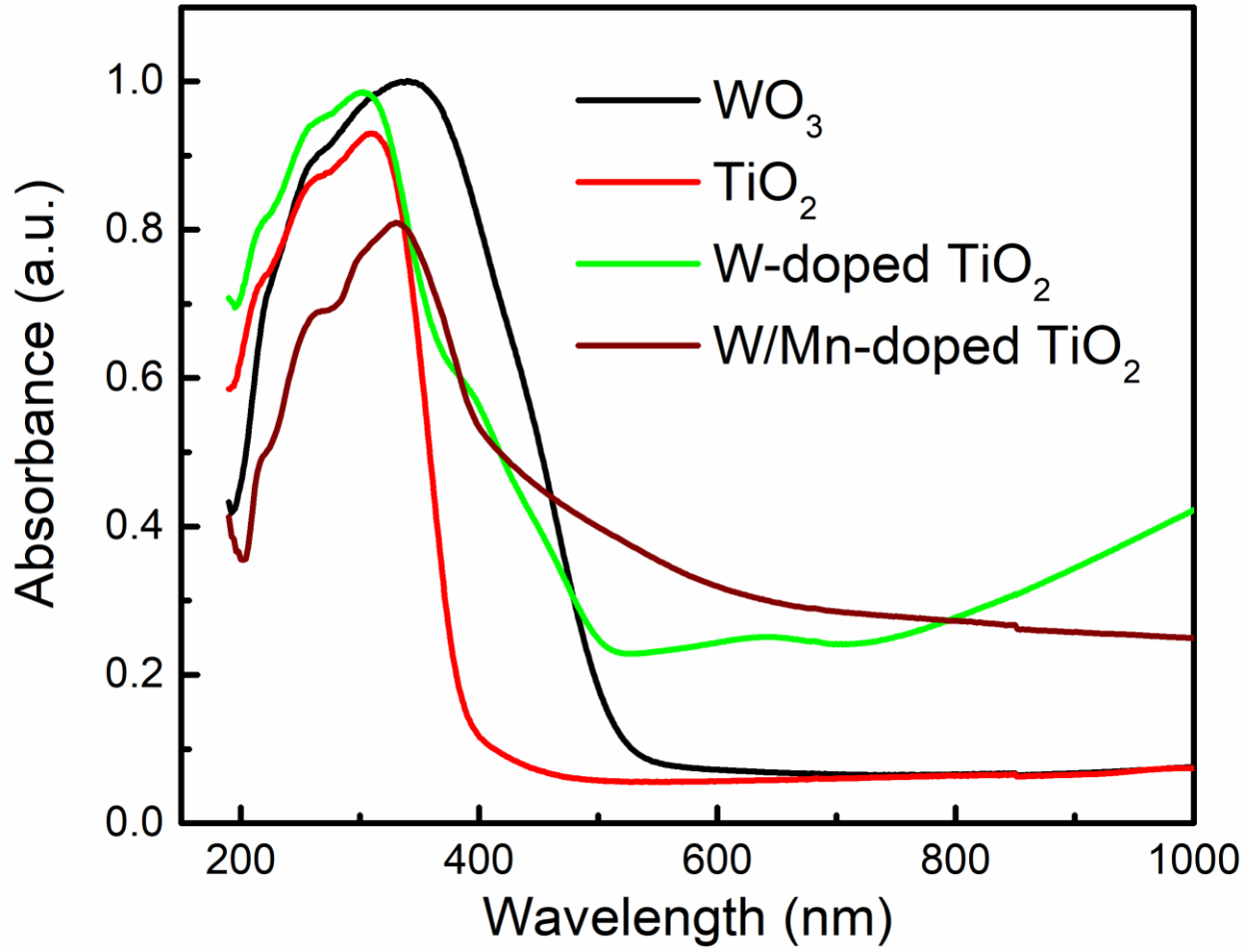

Figure 5.6 UV-vis spectra of WO_3, TiO_2, W-doped TiO_2 and W/Mn doped TiO_2.

5.2.4 Possible Research Directions

Based on the existing research, we have successfully fabricated so called doped 'TiO_2' material with different color. Since all the metal elements are detected by the previous research, more microscopic characterizations are required to determine what forms of coexistence between these different metal oxides. Compared to the white TiO_2, the color indicates that the material begins to absorb visible light at a specific wavelength. Therefore, it is necessary to find out the photocatalytic properties of the material under visible light. In addition, the clarification of photoelectrochemical performance and related applications are also in the consideration.

References

1. Asahi, R., et al., *Visible-Light Photocatalysis in Nitrogen-Doped Titanium Oxides.* Science, 2001. **293**(5528): p. 269-271.
2. Fujii, S., et al., *Selective fabrication of tungsten nano-oxides via submerged photosynthesis with hydrogen peroxide for chromic device application.* Materials Letters, 2021. **302**: p. 130344.

Academic Achievements

Journal Articles (Related to Ph.D thesis):

1. Zhehan Yu, Shilei Zhu, Lihua Zhang, Seiichi Watanabe, Mesoporous single crystal titanium oxide microparticles for enhanced visible light photodegradation, Optical Materials, Volume 127, 2022, 112297.

2. Shilei Zhu, Zhehan Yu, Lihua Zhang, and Seiichi Watanabe, Solution Plasma-Synthesized Black TiO_2 Nanoparticles for Solar–Thermal Water Evaporation, ACS Applied Nano Materials 2021 4 (4), 3940-3948.

3. Zhehan Yu, Lihua Zhang, Seiichi Watanabe, Facile modification of TiO_2 nanoparticles with H_2O_2 + NH_4F for enhanced visible light photodegradation of rhodamine B and methylene blue. Materials Today Communications, 2022. 33: p. 104213.

Presentation at conferences:

1. Zhehan Yu, Shilei Zhu, Lihua Zhang, Seiichi Watanabe, MNC 2021, The Fabrication of Mesoporous Single Crystal Ellipsoid TiO_2 Nanoparticle with Enhanced Visible Light Photodegradation Efficiency. (Online)

2. Zhehan Yu, Lihua Zhang, Seiichi Watanabe, 日本金属学会・日本鉄鋼協会両北海道支部合同サマーセッション, Facile Modification of TiO_2 Nanoparticles with H_2O_2 + NH_4F for Enhanced Visible Light Photodegradation of Rhodamine B and Methylene Blue.

Acknowledgements

At the very beginning, my deepest gratitude goes to my Ph.D. supervisor, Professor Seiichi Watanabe, for giving me the chance as a doctoral student, and support me for the past three years. Professor Watanabe has made outstanding contributions to the research in the field of materials science, laboratory construction, and guidance of student research. Without his guidance and assistance, it is unable for me to complete the work of the doctoral dissertation in three years.

I would also like to say thank you to Professor Lihua Zhang for the kindly guidance during my research life. Professor Zhang has paid a lot attention to both my career and my life, giving me a lot of help while I was confused, and taught me a lot of scientific research methods and skills while I was a rookie.

Additionally, I would like to thank the rest of my dissertation committee, including Professor Tamaki Shibayama and Naoyuki Hashimoto, for their diligent instruction during my research and graduation process. I am also thankful to Professor Noriyuki Okinaka for his suggestions in my work.

The whole research group has contributed a lot to my doctoral life. I would like to thank Secretary Ms. Kaori Mitomo and Ms. Aiko Kishimoto for their help for the related office matters. I would also like to thank Dr. Melbert Jeem, Dr. Shilei Zhu, Dr. Longfei Guo, Dr. Yuki Takahashi, and Dr. Shuntaro Murakami for their assistance of my research, and Mr. Kento Hiraiwa for helping me to adapt to Japanese society. All other members of the Lab of Photo and Thermal Energy Conversion Materials, Tomoya Goto, Junichi Mizuno, Takuya Moriyama, Atsuki Toda, Souta Fujii, Ryoya Hoshino, Akinori Takeda, Mitsuru Ishiguro, Tomohiro Masuda, Keita Oomori, Junpei Tsukamura, Hsueh-I Lin, Ayaka Hayano, Yukihiro Fukushima, Ryota Noto, Masaya Osawa, Satoshi Takai, Kazutaro Yamazaki, Keisuke Abe, Kohei Fukuroi, Hiroto Miyashita, Mahiro Nishimura, Tatsuya Sakai, Shizuka Okumura, Yuichirou Baba, Taisuke Hayama, Hiroki Kumai, Yuma Sakai, Suzuhito Sawaki, have assisted my to varying degrees, and I would like to express my thanks here.

I also need to thank the other people who have helped me during the past three years. I am thankful to Dr. Subing Yang for the assistance of my research, especially in the operation of TEM, Dr. Shenghua Zhang and Dr. Kaixin Dong give me a lot of useful comments and suggestions. The stuffs in Center for Advanced Research of Energy and Materials and Graduate School of Engineering have also given me a lot of help. Additionally, I am grateful with the financial aids

from Minitstry of Education, Culture, Sports, and Technology (MEXT), and Hokkaido University DX Doctoral Fellowship. I am also thankful to Graduate School of Engineering for the employment as Research Assistant and Short-term Support Researcher. Then, I would like to express my thanks to all E3 stuffs for their guidance, help, and assistance in my school life.

I will say thank you to the previous tutors: Professor Ying Liu, Professor Betul Bilgin, Professor Said Al-Hallaj, and other professors and stuffs from University of Illinois at Chicago have given me a lot of guidance during my master's life. Professor Yunzhi Gao, Professor Qinmin Pan, Dr. Shuaifeng Lou, and other professors and stuffs from Harbin Institute of Technology have guided me to get started with research. I will also send my gratitude to my teachers in Hefei No.6 High School, Bengbu No.6 Middle School, and Bengbu No.2 Experimental Primary School, for their leading me to the academic enlightenment.

During my life in Japan, I have received help from many friends. Here, I would like to express my special thanks to Jinmin, Jia, Qi Kan, and Yi Qie. My classmates and friends in China and other countries have also given me a lot of moral support. I would like to say thank you to my classmates: Yuanzhe Wang, Shaobo Ma, Bonan Zhou, Yiqun Zhang, and other classmates of Bengbu No.6 Middle School; all classmates of Hefei No.6 High School class 31 2014; all classmates of Harbin Institute of Technology class 1414202, Reem Khoury, Michell Powers, John Yang, and other classmates in University of Illinois at Chicago. I would also like to say thank you to my other friends: Bingan Chen, Botai Xiong, Lingchen Kong, Yutong Gong, Yirang Tan, all members of my participated societies, and Huiwen Zhou, Shuran You, Liming Zheng, Zixuan Wang. Thank you all for your support.

Finally, I will extend my highest gratitude to my parents, Professorate Senior Engineer Bingliang Yu and Mrs. Yuhong Liu, for their selfless support from both financial and mental, and my maternal grandmother, Mrs. Gao Ling, for keeping believing in me. Also, I will thank to my paternal grandparents, Mr. Maofan Yu and Mrs. Ruilan Huang, and my maternal grandfather, Mr. Guanlian Liu. I hope my Ph.D. degree will comfort your spirits.